Bringing Complexity Science to Real World: Quantification of Stress in Humans and Systems

Theerasak Chanwimalueang

Supervisor: Prof. Danilo P. Mandic

A thesis submitted for the degree of
Doctor of Philosophy (Ph.D.)

Communications and Signal Processing Group
Department of Electrical and Electronic Engineering
Imperial College London
January 2018

I claim that many patterns of Nature are so irregular and fragmented, that, compared with Euclid — a term used in this work to denote all of standard geometry — Nature exhibits not simply a higher degree but an altogether different level of complexity ... The existence of these patterns challenges us to study these forms that Euclid leaves aside as being "formless," to investigate the morphology of the "amorphous."

Benoit Mandelbrot

The amazing thing is that chaotic systems don't always stay chaotic, Ben said, leaning on the gate. Sometimes they spontaneously reorganize themselves into an orderly structure. They suddenly become less chaotic?" I said, wishing that would happen at HiTek. No, that's the thing. They become more and more chaotic until they reach some sort of chaotic critical mass. When that happens, they spontaneously reorganize themselves at a higher equilibrium level. It's called self-organized criticality.

Connie Willis

Abstract

Analysing real-world data within the context of structural complexity is crucial for accurately revealing the dynamical behavior of systems, ranging from individual (human) to network (economic). Indeed, the so-called "Complexity Loss Theory" establishes that complexity measures are able to provide physically meaningful interpretation of, for example, the occurrence of stress in such systems. This theory states that organisms or systems under constraints, such as ageing illness or more generally loss of degrees of freedom, exhibit lower complexity of their observable responses. To this end, this thesis aims to model/quantify stress levels of two dynamical systems: i) autonomic nervous (in humans), and ii) economic (in financial markets). For human based scenarios, we collected Electrocardiogram (ECG) in two human activities: i) public speaking, and ii) music performance. For the assessment of the structural complexity of systems, stock indices from the four major stock markets in the US were used for studying stress in economic.

This thesis introduces a novel framework for analysing physiological stress from heart rate variability (HRV) extracted from the wearable ECG. The framework includes a robust method, established based on the matched filtering method and the Hilbert transform, for detecting R-peaks in noisy ECG. We examine the physiological stress through several standard entropy measures, prior to introducing our novel "Cosine Similarity Entropy" and "Multiscale Cosine Similarity Entropy". These new entropy measures are derived based on angular distance, Shannon entropy and the coarse-grained scale, and shown to successfully and rigorously quantify structural complexity in systems within the context of self-correlation. The analysis over numerous case studies shows that the proposed framework is capable of detecting loss of degrees of freedom, that is, 'stress-patterns' under different stress conditions. Furthermore, we examine economic stress through an enhanced multivariate entropy measure, "Moving-Averaged Multivariate Sample Entropy", which is established based on a standard multivariate entropy and a novel detrended moving average scale.

The MA-MSE makes it possible to capture the periods of financial stress which corresponds to the occurrence of the economic crises correctly.

Overall, the novel algorithms in this thesis have resolved several limitations of the existing entropy measures, especially related to short time series, sensitivity to signal amplitudes, and undefined entropy values for data with artefacts. In addition, real world data do not obey any closed-form probability distribution and are often nonstationary, which requires non-parametric entropy estimators suitable for such scenarios - a subject of this thesis.

Acknowledgements

I would like to thank my supervisor Prof. Danilo Mandic who gave me the opportunity to undertake this PhD and for his support during the tough times. During the last four years, through his encouragement and guidance, he has given me countless opportunities to develop as a person and a scholar. Next, I am particularly grateful to Dr. David Looney and Dr. Valentin Goverdovsky for the assistance and supervision given on writing publications and conducting experiment. I am indebted to Apit Hemakom and Wilhem von Rosenberg for our fruitful academic discussion and their generous help. I would like to show my gratitude to Xiang Min who helps solving my technical problems over four years of my PhD. I would like to thank Alicia C. Garcia for her excellent collaboration on our publications. I would like to thank Dr. Mosabber Ahmed for introducing me the concept of the Multivariate Multiscale Entropy approach. I am thankful to have been given the privilege to work with Prof. Anthony G. Constantinides. I am grateful to the CSP group administrator, Ms. Charlotte Grady, who has supported me during my PhD. I would like to thank Takashi, Tricia, Sithan, Pouria, Alex, Ilia, Giuseppe and Thayne for their kindly help. I am thankful for the help given by Bruno, who provides important details on the history of the economic crises. I would like to thank Prof. Aaron Williamon for collaboration and advice on our music performance research. I would like to express gratitude to Dr. Wongwit Senawong, who gave me the opportunity to pursue a PhD degree in the UK. I would like to acknowledge the Royal Thai Government for the PhD funding. I also would like to acknowledge my colleagues at the Biomedical Engineering Department, Engineering Faculty, Srinakharinwirot University. Last but not least, my heartfelt gratitude goes to my family for their love, care, understanding and support.

Theerasak Chanwimalueang

January 2018

Contents

List of Figures

List of Tables

Statement of Originality

I declare that the work presented in this thesis is the outcome of my research under the supervision of Prof. Danilo P. Mandic. Ideas and results from the work of others are appropriately acknowledged with the standard referencing practices employed in this discipline. The material in this thesis has not been submitted for any degree at any other academic or professional institution.

Copyright Declaration

List of Principal Symbols

N	number of samples
$H[\cdot]$	Hilbert transform
$x(t)$	real function
$x^{(h)}(t)$	Hilbert transform of $x(t)$
τ_s	time shift of the Hilbert transform
$X^{(h)}(j\omega)$	Fourier transform of $x^{(h)}(t)$
$\|s(t)\|$	norm of $x^{(h)}(t)$
m	embedding dimension
τ	time lag for entropy measures
r	tolerance level for entropy measures
r_{se}	tolerance level for the sample entropy
r_{fe}	tolerance level for the fuzzy entropy
r_{cse}	tolerance level for the cosine similarity entropy
ϵ	scale factor for entropy measures
$1/f$	fractal noise
$\{x_i\}_{i=1}^{N}$	a time series with a number of samples N
$\boldsymbol{x}_i^{(m)}$	embedding vector i with a given embedding dimension im
$ChebDis_{i,j}^{(m)}$	Chebyshev distance between $\boldsymbol{x}_i^{(m)}$ and $\boldsymbol{x}_j^{(m)}$
$P_i^{(m)}(r)$	a number of similar patterns of $\boldsymbol{x}_i^{(m)}$ with a given tolerance level r

$B_i^{(m)}(r)$	local probability of occurrences of similar patterns with a given r
$B^{(m)}(r)$	global probability of occurrences of similar patterns with a given tolerance r
$y_i^{(\epsilon)}$	coarse-grained scale of $\{x_i\}_{i=1}^N$ with a scale factor ϵ
η	a Guassian order
$S_i^{(m)}(r_{fe}, \eta)$	fuzzy similarity of $\boldsymbol{x}_i^{(m)}$ with a given r_{fe} and η
$CosSim_{i,j}^{(m)}$	cosine similarity between $\boldsymbol{x}_i^{(m)}$ and $\boldsymbol{x}_j^{(m)}$
$CosDis_{i,j}^{(m)}$	cosine distance between $\boldsymbol{x}_i^{(m)}$ and $\boldsymbol{x}_j^{(m)}$
$\alpha_{i,j}^{(m)}$	an angle between $\boldsymbol{x}_i^{(m)}$ and $\boldsymbol{x}_j^{(m)}$
$AngDis_{i,j}^{(m)}$,	angular distance between $\boldsymbol{x}_i^{(m)}$ and $\boldsymbol{x}_j^{(m)}$
$\{\boldsymbol{s}_i\}_{i=1}^N$	a zero median time series of $\{\boldsymbol{x}_i\}_{i=1}^N$
α_i	a correlation coefficient of an order i^{th} of an autoregressive process
p	an order of an autoregressive model
e_{min}	minima
e_{max}	maxima
$m(t)$	local mean
$d(t)$	local oscillation

List of Abbreviations

AF	Atrial Fibrillation
ALIS	Assessment of Latent Index of Stress
ANS	Autonomic Nervous System
ApEn	Approximate Entropy
AR	Autoregressive (model)
AVNN	Averages of Normal to Normal Intervals
CGP	Coarse Graining Process
CHF	Congestive Heart Failure
CLT	Complexity Loss Theory
CSE	Cosine Similarity Entropy
DJIA	Dow Jones Industrial Average
ECG	Electrocardiogram
QRS	a name for the combination of three of the graphical deflections of ECG
EEG	Electroencephalogram
EMD	Empirical Mode Decomposition
EMH	Efficient Market Hypothesis
FE	Fuzzy Entropy
FSI	Financial Stress Index
FT	Fourier Transform

GAS	General Adaptation Syndrome
GUI	Graphic User Interface
HF	High Frequency (HF band of heart rate variability)
HR	Heart Rate
HRV	Heart Rate Variability
LF	Low Frequency (LF band of heart rate variability)
LSP	Lomb-Scargle Periodogram
MA	Moving-average (method)
MA-MSE	Moving-average Multivariate Sample Entropy
MCSE	Multiscale Cosine Similarity Entropy
MF-HT	Matched Filtering-Hilbert Transform
MFE	Multiscale Fuzzy Entropy
MMSE	Multivariate Multiscale Sample Entropy
MSE	Multiscale Sample Entropy
NS	Nervous System
NSR	Normal Sinus Rhythm
pNN50	Percentage of Differences Between Adjacent Normal to Normal Intervals
PNS	Parasympathetic Nervous System
PSD	Power Spectrum Density
PT	Pan and Tompkins (algorithm)

QTDB	a database of a wide variety of QRS and ST-T morphologies in ECG
rMSSD	Square Root of The Mean of The Squares of the Differences Between Adjacent Normal to Normal Intervals
RRID	Deviation of the RR-intervals
RS	Resistance to Stress
RSA	Respiratory Sinus Arrhythmia
SDNN	Standard Deviation of All Normal to Normal Intervals
SE	Sample Entropy
Se	Sensitivity
se	Standard Error
sd	Standard Deviation
SNR	Signal-to-Noise Ratio
SNS	Sympathetic Nervous System
TOTPWR	Total Power spectral Power
VLF	Very Low Frequency band
WGN	White Gaussian Noise

Publications

The following publications support the material given in this thesis:

Published Peer-reviewed Journals

- **T. Chanwimalueang**, and D. P. Mandic, "Cosine Similarity Entropy: Self-Correlation-Based Complexity Analysis of Dynamical Systems," *Entropy*, vol. 19, no. 12(652), pp. 1–23, 2017.
- **T. Chanwimalueang**, L. Aufegger, T. Adjei, D. Wasley, C. Cruder, D. P. Mandic, and A. Williamon, "Stage call: Cardiovascular reactivity to audition stress in musicians," *PLOS ONE*, vol. 12, no. 4, pp. 1–14, 2017.
- M. U. Ahmed, **T. Chanwimalueang**, S. Thyyil, and D. P. Mandic, "A Multivariate Multiscale Fuzzy Entropy Algorithm with Application to Uterine EMG Complexity Analysis," *Entropy*, vol. 19, no. 1(2), pp. 1–18, 2016.
- A. Hemakom, **T. Chanwimalueang**, A. C. Garciá, L. Aufegger, A. G. Constantinides, and D. P. Mandic, "Financial stress through complexity science," *IEEE Journal of Selected Topics in Signal Processing*, vol. 10, no. 6, pp. 1112–1126, 2016.

Published Peer-reviewed Conference Proceedings

- **T. Chanwimalueang**, W. von Rosenberg, and D. P. Mandic, "Enabling R-peak Detection in Wearable ECG: Combining Matched Filtering and Hilbert Transform," *In Proceedings of the IEEE International Conference on Digital Signal Processing (DSP 2015)*, pp. 134–138, 2015.
- **T. Chanwimalueang**, L. Aufegger, W. von Rosenberg, and D. P. Mandic, "Modelling stress in public speaking: Evolution of stress levels during conference presentations," *In Proceedings of the IEEE International*

Conference on Acoustics, Speech and Signal Processing (ICASSP 2016)," pp. 1–18, 2016.

- A. C. Garciá, **T. Chanwimalueang**, G. G. Calvi , A. Hemakom, R. M. Ricós, and D. P. Mandic, "Modelling economic stress through financial systemic balance index," *In Proceedings of the IEEE International Conference on Digital Signal Processing (DSP 2016)*, pp. 565–569, 2016.

- W. von Rosenberg, **T. Chanwimalueang**, D. Looney, and D. P. Mandic, "Vital signs from inside a helmet: A multichannel face-lead study," *In Proceedings of the IEEE International Conference on Acoustics, Speech and Signal Processing (ICASSP 2015)*," pp. 982–986, 2015.

Other publications which are not included in the thesis:

- W. Von Rosenberg, **T. Chanwimalueang**, V. Goverdovsky, D. Looney, D. Sharp, D. P. Mandic, "Smart helmet: Wearable multichannel ECG and EEG," *IEEE Journal of Translational Engineering in Health and Medicine*, vol. 4, pp. 1–11, 2016.

- W. Von Rosenberg, **T. Chanwimalueang**, V. Goverdovsky, D. P. Mandic, " Smart helmet: Monitoring brain, cardiac and respiratory activity," *In Proceedings of IEEE International. Conference on Medicine and Biology Society (EMBC 2015)*, pp. 1829-1832, 2015.

- W. Von Rosenberg, **T. Chanwimalueang**, A. Tricia, J. Usman, V. Goverdovsky, D. P. Mandic, "Resolving ambiguities in the LF/HF ratio: LF-HF scatter plots for the categorization of mental and physical stress from HRV," *Frontiers in Physiology*, vol. 8, no. 360, pp. 1–12, 2017.

Chapter 1

Introduction

Analysis of real-world data in the context of structural complexity is important for understanding the dynamical behaviour of physical and biological systems, ranging from individual systems (human) to collaborative networks (economic). Based, for example, on the "complexity loss theory" and the "efficient market hypothesis", complexity measures are able to provide physically meaningful interpretation to describe the occurrence of stress in such systems. Our aim is to study stress in two dynamical systems: i) autonomic nervous (in human), and ii) economic (in financial markets). We collected the Electrocardiogram (ECG) data from two scenarios: i) public speaking, and ii) music performance for studying stress in human, while we obtained four major US stock indices for studying stress in economics. Heart rate variability (HRV) extracted from the recorded ECG is used to analyse stress in humans, since the intrinsic properties of HRV reflect the dynamical mechanism of the autonomic nervous system physiologically in response to stress. Besides, the stress in economy has a close connection with the occurrence the stress in individuals but with regard to behaviours of a vast number of investors in response to incidents/situations (financial stressors); this results in systemic variability which can lead to an occurrence of economic crisis. To quantify structural complexity of the two systems, entropy-based measures are employed, since they are nonlinear metrics used to estimate degrees of uncertainty or correlation, through the examination of similar patterns of the underlying structures of the system.

In this chapter, the brief concepts of physiological stress, heart rate variability, complexity loss theory and efficient market hypothesis are introduced. The review of well-known entropy-based complexity measures is also provided. We

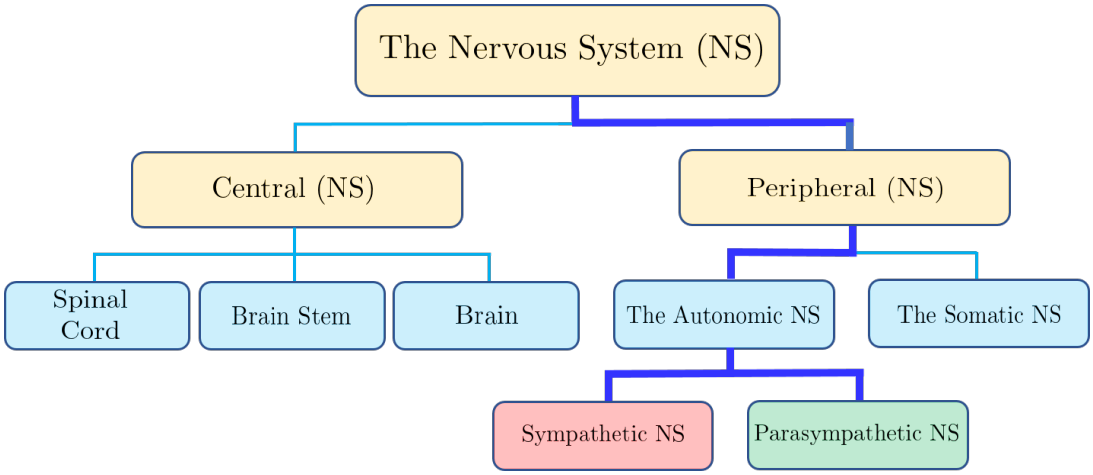

Figure 1.1: **The divisions of the nervous system (NS)**. Physiological stress is directly related to the cooperation between the sympathetic NS (arousing the body) and the parasympathetic NS (calming after arousal), both of which are part of the autonomic NS, a branch of the peripheral NS.

then summarise the original contributions of our studies and the organisation of the thesis.

1.1 Physiological Responses to Stress

The term 'stress' was first generally defined by Selye [1] who described it as "the non-specific response of the body to any demand for change" [2]. For more specific stress-related physiological responses, the term "physiological stress" is used to represent an agglomerate response of multiple systems in the body to external stressors, such as working under pressure, performing various physical or cognitive tasks, rushing to meet a deadline [3, 4].

The physiological system which directly affected by stress is the autonomic nervous system (ANS) (a division within the peripheral nervous system[1] as shown in Figure 1.1) which regulates involuntary bodily processes including heart rate, respiration, digestion and pupil contraction. The ANS is divided into two

[1]The peripheral nervous system is comprised of the autonomic nervous system (ANS) and the somatic nervous system. While the ANS controls involuntary bodily responses/processes, the somatic nervous system is responsible to receive/transmit information between sensory nerves/motor units and central nervous system for any voluntary movements.

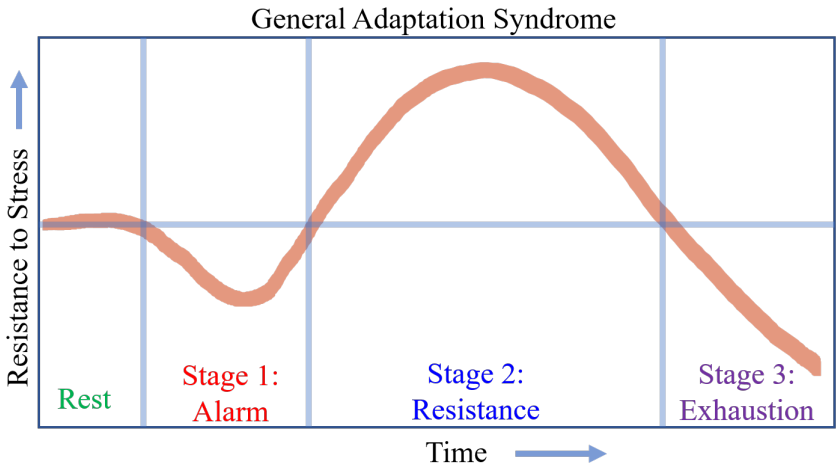

Figure 1.2: **Graphical interpretation of the General Adaptation Syndrome (GAS).** Evolution of resistance to stress over time based on the GAS can be described in 3 stages (rest is excluded): i) alarm, ii) resistance, and iii) exhaustion. The fight-or-flight response (SNS dominates) corresponds to the alarm stage, while the period of coping with stress presents in the resistance stage (PNS dominates), and the stage of perceiving long-term stress (uncooperative SNS and PNS) occurs in the exhaustion stage. This Figure is modified from [5].

sub-systems: i) the sympathetic nervous system (SNS), and ii) the parasympathetic nervous system (PNS), both of which cooperates automatically without conscious direction. The PNS and SNS play an important role in response to stress for which the SNS prepares the body for action, so-called "fight or flight" [7, 8], while the PNS calms and helps the body to conserve energy. The activation of the SNS exhibits an increase in heart rate and respiratory rate, eye dilation, and a decrease in stomach motility, while the activation of the PNS exhibits a decrease in heart rate and respiratory rate, eye constriction and an increase in stomach motility. The system that mainly controls the activation of both the PNS and SNS is called the "hypothalamic-pituitary-adrenal axis"; the complex interactions among the three components: the hypothalamus, the pituitary gland and the adrenal gland, all of which transmits/receives hormonal and neural signals to various organs in response to stress [9]. The activation of SNS and PNS regarding a period of experiencing stress can be described based on the General Adaptation Syndrome

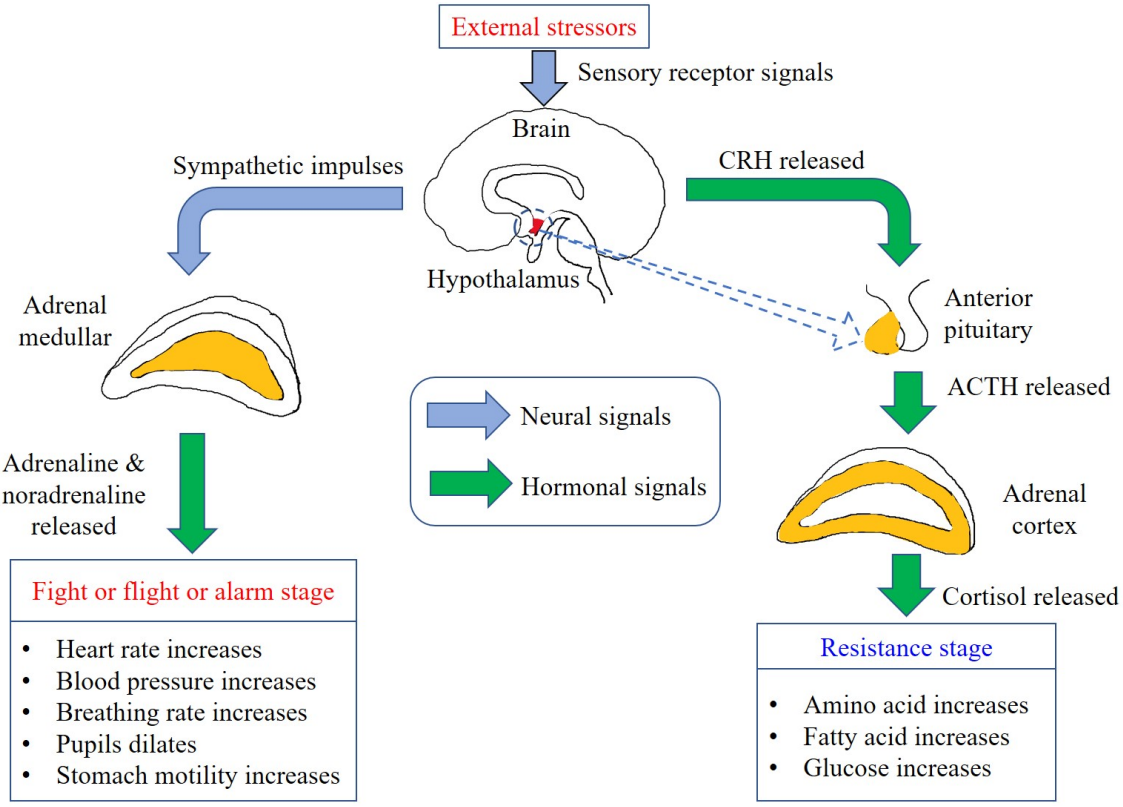

Figure 1.3: **Physiological responses to stress**. The hypothalamus reacts to external stressors by triggering sympathetic impulses to the adrenal medulla which then secretes the adrenaline and noradrenaline hormones. This results in an increase in heart rate, blood pressure, breathing rate, etc. to preparing the body in "fight or flight" mode. In the resistance stage, the hypothalamus releases the corticotropin-releasing (CRH) hormone to the pituitary gland which secretes the adrenocorticotropic hormone (ACTH) to trigger the adrenal cortex which then secretes the cortisol hormone. This results in an increase in blood amino acid, fatty acid, and glucose for supplying cells during a stress period. This figure is modified from [6].

(GAS) proposed in [1]. The GAS elucidates the evolution of stress through the term "Resistance to Stress" (RS) over a period of time as shown in Figure 1.2. At the beginning, the body is in the rest stage, so-called 'homeostasis', for which the activation of both the SNS and PNS is at a normal level (balance). Right after perceiving stressors, the body reacts to stress in the fight-or-flight mode as a response to threat or danger; this period is called the "alarm stage". At this stage, the hypothalamus transmits sympathetic impulses (neural signals) to trigger the adrenal medulla which then secretes the adrenaline and noradrenaline

hormones. This results in an increase in heart rate, blood pressure, stomach motility, respiratory rate, etc and causes a reduction in the RS to the minimum level, i.e. the SNS dominates [6, 9]. After the moment of fight-or-flight, the body attempts to cope and calm by activating the PNS causing a raise in the RS to the homeostasis level. However, this process still continues as the announcement of the "resistance stage" for which the body overwhelms the activation of the PNS (the PNS dominates) for compromising the physiological functions; this results in an increase in the RS to the maximum level. In the resistance stage, the hypothalamus releases the corticotropin-releasing hormone (CRH) to trigger the pituitary gland which then secretes the adrenocorticotropic hormone (ACTH) to activate the adrenal cortex to release the cortisol hormone. This results in an increase in blood amino acid, fatty acid, and glucose for supplying biochemical processes used by cells during a stress period [6, 9]. If the body is able to cope stress at this stage well, the RS level will then decrease to the rest level; otherwise, in case the body still perceives stress for a long period continuously without the ability to cope, the body become exhausted as failure of collaboration in both the SNS and PNS. This causes a reduction in the RS level as an announcement of the exhaustion stage. Note that the stress occurs in the period of the alarm and resistance stages is called "acute stress" which typically lasts for from minutes to hours), while the stress in the period of the exhaustion stage is called "chronic stress" which typically lasts for days, weeks or months). The mechanism of the hypothalamic-pituitary-adrenal axis in response to stress is illustrated in Figure 1.3.

1.2 Heart Rate Variability (HRV)

Heart rate variability (HRV) represents continuous changes in cardiac rhythms which reflect a state of body and mind in response to a stressor. The HRV is an estimation of the RR-intervals extracted from the R-peaks of the recorded[2] ECG.

[2]In practice, ECG recordings are noisy and are contaminated with movement artefacts, so that a robust method is required to the accurate detection of the R-peaks.

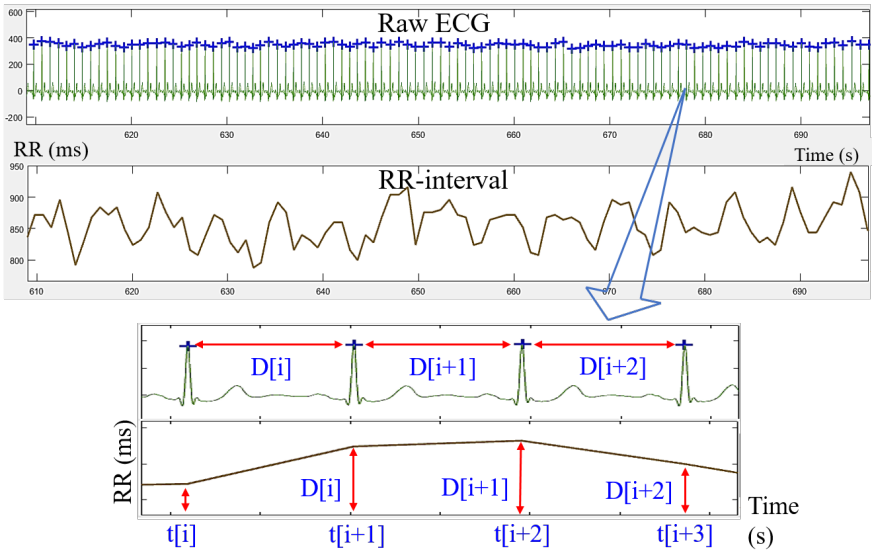

Figure 1.4: **R-peaks detection and RR-intervals**. Top: an example of a 90-sec raw ECG (with R-peaks, + in blue) and its extracted RR-intervals. Bottom: The zoom window of the 3.5-sec raw ECG and its corresponding RR-intervals, whereby any RR-interval, D[i], is obtained from a distance between consecutively pairwise R-peaks.

The RR-intervals are obtained from a series of distances between consecutively pairwise R-peaks of the ECG. Figure 1.4. shows an example of the three RR-intervals, D[i], D[i+1] and D[i+2] calculated from distances between four consecutive R-peaks, D[i] = t[i+1] - t[i], D[i+1] = i[i+2] - t[t+1] and D[i+2]=t[i+3] - t[t+2]. However, these extracted RR-intervals are unevenly sample-spaced data which is not appropriate for time-, frequency- or nonlinear analysis, so that the RR-intervals are re-sampled by using an interpolation technique to obtain equally sample-spaced data, resulting in the HRV.

The underlying intrinsic properties of the HRV have been found in connection with stress based on the GAS [1]. It is believed that the frequency spectrum of the HRV between 0.04-0.4 Hz reflects the mechanism of the ANS, whereby the summation of spectrum power in the low frequency band (LF), between 0.04-0.15 Hz, is thought to reflect the SNS activity, and the summation of spectrum power in the high frequency band (HF), between 0.15-0.4 Hz, is thought to reflect the PNS activity [10, 11]. The well-known index called LF/HF ratio has been

widely used for assessing the balance between SNS activity and PNS activity (so-called "Sympathovagal Balance"), and is also used as an indicator of stress levels [11]. Although the analysis of HRV in the frequency domain can identify and capture changes in stress, nonlinear analysis in the form of structural complexity has recently been used to quantify degrees of determinism versus randomness in signals and has become prevalent [12, 13, 14, 15].

1.3 Entropy-based Complexity Measures

The concept of complexity [16, 17, 18] and complex adaptive systems [19, 20] spans a range of interdisciplinary approaches, from the theory of nonlinear dynamical systems to real-world systems studied in many disciplines, such as physics, mechanics, biology, and economics [20, 21]. Such real-world systems usually exhibit nonlinearity and/or nonstationarity whereby drift and deterministic/stochastic trends locally and globally burried in observational data. This is due to the nature of the aggregated responses from the small functional units/elements embedded in a system which produces similar or different amplitudes and latency (time delays); for example, physiological signals are electrical nerve activities responding to bio-related stimulation and are measured in a form of a summation of neuron action potentials. The production of action potential is considered as a nonlinear process regarding the action potential's "all-or-none law" whereby each neuron fires its potential at a different rate until the sum of voltages reaches a certain threshold value [22, 23]. Another example is financial time series which reflect average prices driven by investors in particular markets. Activities of each investor (analogous to a small unit/element) can vary in terms of: i) an amount of buys or sells (amplitudes) and ii) when they make a decision (a response time), both of which depend on a reaction to simulators, such as news and regional/international regimes. This yields a series of an aggregation of average prices which fluctuates over time. Financial time series have been well modelled using the random-walk process which is effectively used to estimate the deterministic/stochastic trends of such financial data.

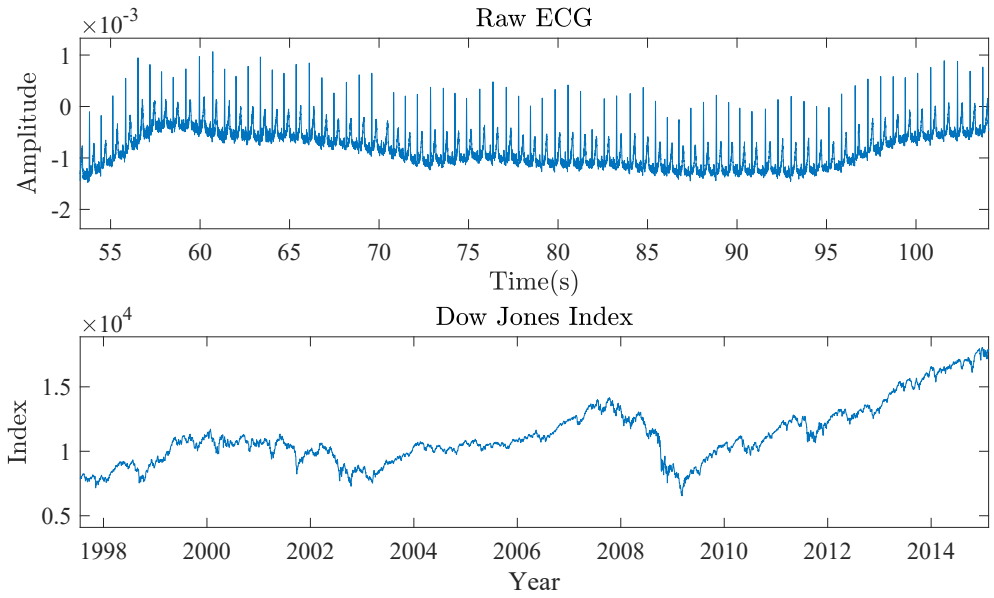

Figure 1.5: **Two examples of real-world data**. A segmented raw ECG (top) is plotted over the interval between 53 and 105 second, and the Dow Jones index (bottom) is plotted over a period of 1997-2015. Observe the nonstationary components are buried in the both data in the form of baseline drift (ECG) and deterministic/stochastic trends (Dow Jones index).

[24, 25, 26]. Figure 1.5 depicts two examples of real-world data are : i) ECG (physiological data) and ii) Dow Jones index (a financial time series).

In the statistical sense, the distribution of such real-world data can present in any forms and is not necessary to be Gaussian. This could make standard linear metrics and the standard descriptive statistic, such as mean, standard deviation, a time or frequency domain analysis, fail to reveal genuinely intrinsic characteristics [27, 28]. Many researchers have realized this issue and therefore attempted to study and invent nonlinear measures for analysing such real-world data. An important principle widely used in nonlinear approaches is called the "Takens embedding theory" [29] which briefly states that "the properties and information of 'smooth' dynamical systems can be analogously represented by their reconstructed observational data (so-called embedding vectors or delay vectors) with an appropriate selection of an embedding dimension m and a time lag τ". The term 'smooth' is referred to a time frame captured continuously for

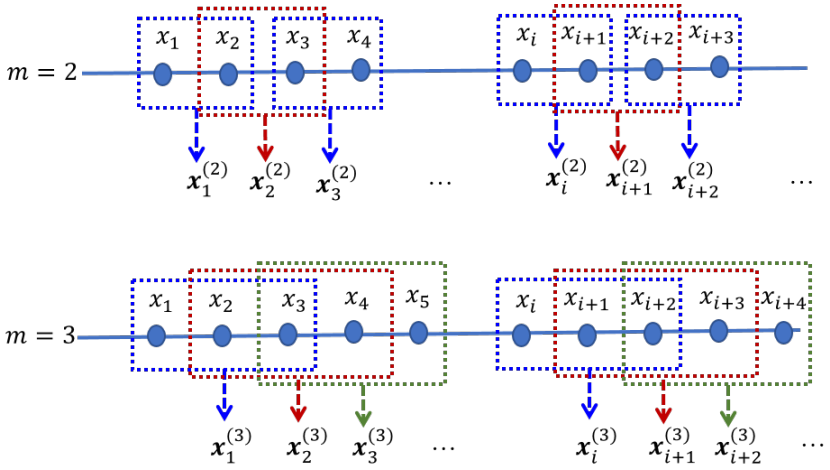

Figure 1.6: **Reconstructed embedding vectors**. For a given time series $\{\boldsymbol{x}_i\}_{i=1}^{N}$, any embedding vector $\boldsymbol{x}_i^{(m)}$ is reconstructed with a chosen embedding dimension (m, i.e. a number of elements in an embedding vector) . Top: embedding vectors $\boldsymbol{x}_i^{(2)}$ with $m = 2$. Bottom: embedding vectors $\boldsymbol{x}_i^{(3)}$ with $m = 3$.

the state space variables of the considered system. The parameter m represents an appropriate number of dimension for reconstructing on a phase space and the parameter τ approximately represents a time delay response of a system. Suppose $\{x_i\}_{i=1}^{N}$ is a time series obtained from any system, an embedding vector $\boldsymbol{x}_i^{(m)}$, can mathematically be generated from equation (1.1). An arrangement of embedding vectors with a given $m = 2$ and $m = 3$ is depicted in Figure 1.6, and an illustrative example of the embedding vectors reconstructed from Lorentz system, a three-variable dynamical system, is shown in Figure 1.7.

$$\boldsymbol{x}_i^{(m)} = [x_i, x_{i+\tau}, ..., x_{(i+(m-1)\tau)}],\ i = 1, ..., N - m + 1 \tag{1.1}$$

Takens embedding theory implies that we are able to model dynamical systems through their embedding vectors reconstructed from a single channel of observational data, which comparably represent the structures or patterns of the original dynamical system. Based on this theory, Pincus [12, 30, 31, 32, 33, 34] exploited the theory and invented a statistical entropy-based measure called the "Approximate Entropy" (ApEn) which is classified as a nonparametric metric (a statistical analysis for any non-Gaussian distributed data) [35]. The ApEn

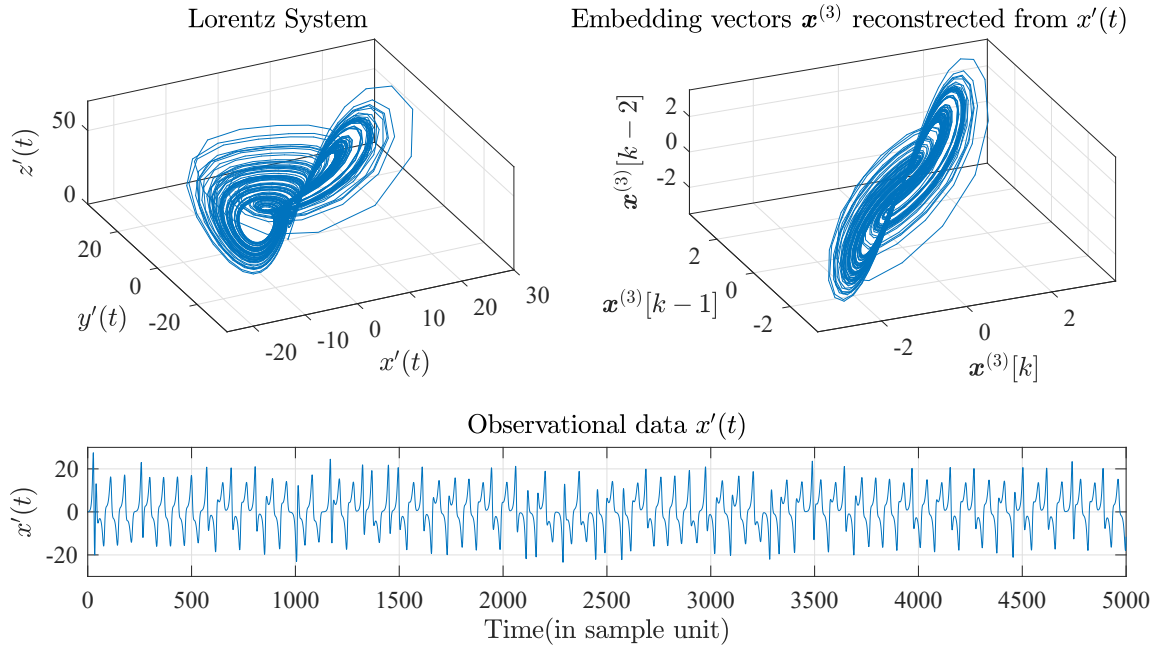

Figure 1.7: **The Lorentz system and its reconstructed embedding vectors**. Top left: the 5,000 samples of the three variables $x'(t)$, $y'(t)$ and $z'(t)$ generated from the Lorentz system, $x'(t)= \sigma(y-x)$, $y'(t) = x(\rho - z)$, $z'(t) = xy - \beta z$, when $\sigma = 10$, $\rho = 28$ and $\beta = 8/3$ with an initial condition $x = y = z = 0.1$. Bottom: the 5,000 samples observed from the single variable $x'(t)$ generated from the Lorentz system. Top right: the reconstructed embedding vectors $\boldsymbol{x}^{(3)}$ from $x'(t)$, with a selection of an embedding dimension $m = 3$ and a time lag $\tau = 1$, are plotted on a three-dimensional phase space. Observe that the trajectory of the embedding vectors $\boldsymbol{x}^{(3)}$ is analogous to the trajectory of the original three-variable Lorenz system. Based on Takens embedding theory, the properties of such Lorenz system can be comparably represented by its reconstructed embedding vectors.

approach has become an essential tool for quantifying 'regularity/irregularity' of dynamical systems [31, 32], whereas in statistical mechanics, entropy may be understood as a measure of 'disorder' within a macroscopic system (especially a thermodynamic system), and in information theory, entropy means a measure of 'uncertainty' of random variables. We should note that the terms, 'irregular', 'disorder' and 'uncertainty', conceptually present a common meaning and can be comprehended as a measure of degrees of similar/dissimilar structures (patterns) in considered observational data [32, 36]. Figure 1.8 illustrates a concept of embedding vector-based similar patterns which is based on an amplitude or angle distance computed from all elements in any embedding vectors. The ApEn

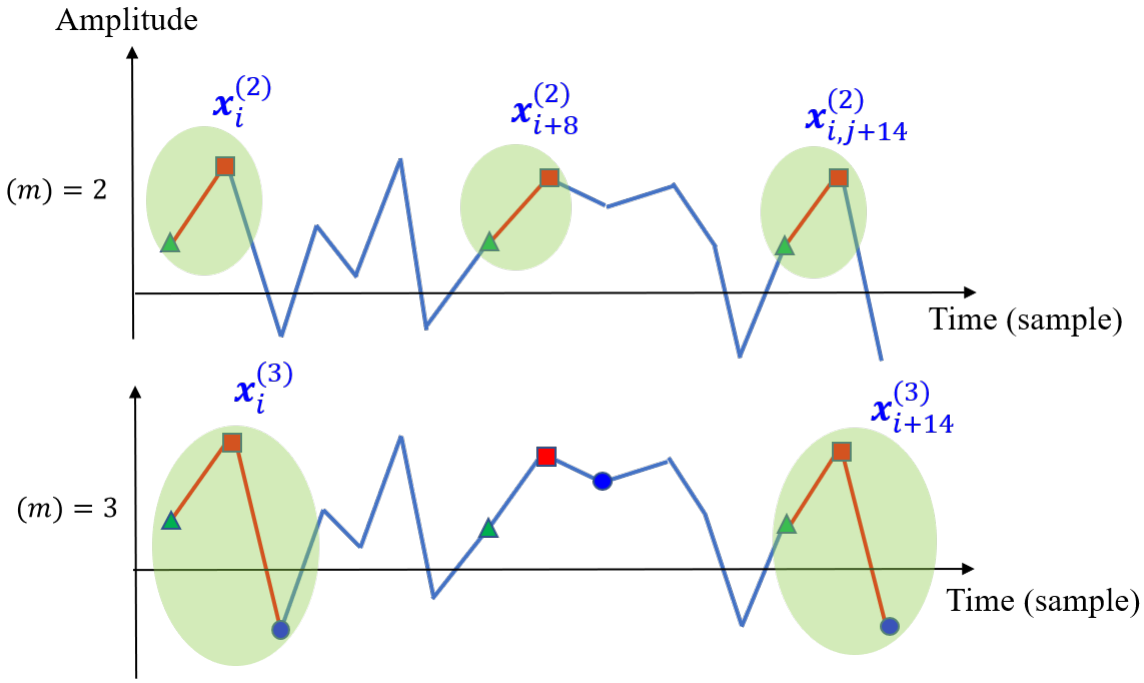

Figure 1.8: **An example of embedding vector-based similar patterns of a time series**. Top: embedding vectors reconstructed from a time series $\{\boldsymbol{x}_i\}_{i=1}^{N}$with a given embedding dimension $m = 2$ and $\tau = 1$. Bottom: embedding vectors reconstructed from a time series $\{\boldsymbol{x}_i\}_{i=1}^{N}$ with a given embedding dimension $m = 3$ and $\tau = 1$. Observe the similar patterns (structures) of both embedding dimensions are detected in the green area whereby any amplitude- or angle-based distance can be used to judge for such similar patterns (an amplitude-based Chebyshev distance is used in the ApEn approach).

method is based on the probability of occurrences of similar patterns found in embedding vectors with a given embedding dimensions, m, and in embedding vectors of a higher dimension, $(m + 1)$. The term 'structures' can be interpreted as a manifestation of intricate inter-connectivity of elements within a system and its surroundings [19] and is represented by the reconstructed embedding vectors [37, 38, 39], and lastly "similar structures" (similar patterns) are judged by small different distances among embedding vectors (the Chebyshev distance method is used in the ApEn approach). The steps of computing approximate entropy are summarised in Algorithm 1.1.

Algorithm 1.1. Approximate Entropy

For a time series $\{x_i\}_{i=1}^{N}$ with a given embedding dimension (m), tolerance (r_{ae}) and time lag (τ):

1. Construct the embedding vectors from $\{\boldsymbol{x}_i\}_{i=1}^{N}$ using
$$\boldsymbol{x}_i^{(m)} = [x_i, x_{i+\tau}, ..., x_{(i+(m-1)\tau)}]\,, i = 1, ..., N-m+1$$
2. Compute the Chebyshev distance for all pairwise embedding vectors as
$$ChebDis_{i,j}^{(m)} = max_{l=1,2,...,m}\{\boldsymbol{x}_i^{(m)}[i+l-1] - \boldsymbol{x}_j^{(m)}[j+l-1]\}$$
3. Obtain the number of similar patterns, $P_i^{(m)}(r_{ae})$, when a criterion $ChebDis_{i,j}^{(m)} \leq r_{ae}$ is fulfilled
4. Compute the local probability of occurrences of similar patterns, $B_i^{(m)}(r_{ae})$, given by
$$B_i^{(m)}(r_{ae}) = \tfrac{1}{N-m+1} P_i^{(m)}(r_{ae})$$
5. Compute the global probability of occurrences of similar patterns, $B^{(m)}(r_{ae})$, using
$$B^{(m)}(r_{ae}) = \tfrac{1}{N-m+1} \textstyle\sum_{i=1}^{N-m} ln\, B_i^{(m)}(r_{ae})$$
6. Repeat Step 1 to Step 6 with an embedding vector $(m+1)$ and obtain $B^{(m+1)}(r_{ae})$ from
$$B^{(m+1)}(r_{ae}) = \tfrac{1}{N-m+1} \textstyle\sum_{i=1}^{N-m} ln\, B_i^{(m+1)}(r_{ae})$$
7. Approximate entropy is then estimated in the from
$$ApEn(m, \tau, r_{ae}, N) = B^{(m)}(r_{ae}) - B^{(m+1)}(r_{ae})$$
.

However, as ApEn counts all such sequences, including self-matches, this introduces a bias in the entropy value which causes ApEn to greatly depend on the time series length [13]. To address the lack of consistency in the ApEn estimates, Richman and Moorman [13] introduced the "Sample Entropy" (SE) algorithm. SE is an improved version of the ApEn, whereby the occurrences of the self-similar patterns are not considered; this results in unbiased entropy estimates. The recent "Fuzzy Entropy" (FE), an improved version of the SE, has been proposed in [14, 40, 41, 42]. The FE provides a more robust examination of the similarity between embedding vectors by replacing the Heaviside function,

used as a criterion in the SE, with a fuzzy membership function, such as Sigmoid or Gaussian. The FE has been proven to be superior to the SE for short sample sizes and insensitivity to spikes [14]. The full steps of SE and the FE algorithms are described in details in Chapter 3.

Besides, Costa et al. [15] noticed a discrepancy in the SE estimates when applied to physiological time series and attributed this to the fact that SE estimates were only defined for a single scale (scale here means the scaled data generated using any temporal or spatial scaling-based method). *They argued that the dynamics of a complex nonlinear system manifests itself in multiple inherent scales of the observed time series and, thus, SE estimates calculated over a single scale are not sufficient descriptors.* This led to the "Multiscale Sample Entropy" (MSE) method in which the multiple scales of input data are first extracted using the so-called "Coarse Graining Process" (CGP) and SE estimates are subsequently calculated for each scale separately [15, 43] (the full steps of the MSE algorithm are described in Chapter 3). The CGP is based on moving average with non-overlapped windows of a time series $\{x_i\}_{i=1}^{N}$ and yields a new, successively shorter, time series. The coarse-grained scale is mathematically generated by

$$y_i^{(\epsilon)} = \frac{1}{\epsilon} \sum_{i=(j-1)\epsilon+1}^{j\epsilon} x(i),\ 1 \leq j \leq N/\epsilon \tag{1.2}$$

The coarse graining process with the two scale factors, $\epsilon = 2$ and $\epsilon = 3$ is depicted in Figure 1.9, and an examples of the coarse graining process applied to the random white noise and the truly complex self-similar and infinitely repeating noise, so-called $1/f$ noise, are depicted in Figure 1.10. By applying the MSE to the random white noise and $1/f$ noise, Costa found that the random white noise at the smallest scale factor has a higher entropy than the entropy of $1/f$ noise. However, with an increase in the scale factor, the entropy of random noise decreases, while the entropy of the $1/f$ noise remains constant over the whole range of scale factors [15, 43] (see Figure 1.11). This means that we should consider an entropy curve

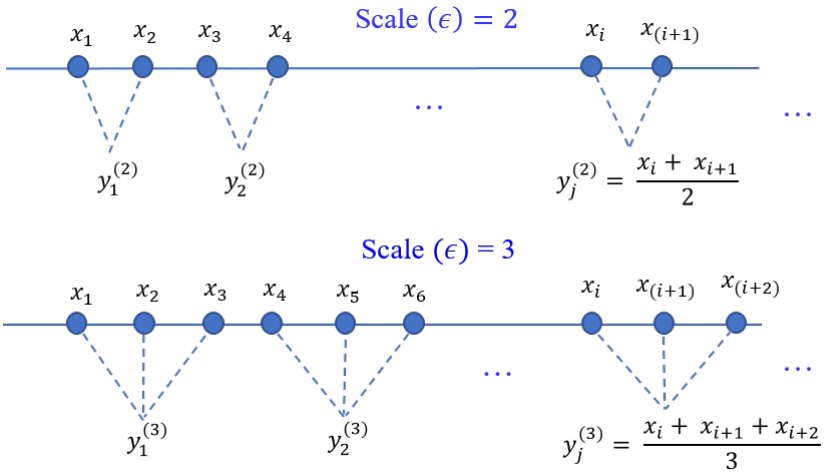

Figure 1.9: **Coarse graining process**. For a given a time series $\{\boldsymbol{x}_i\}_{i=1}^{N}$, any scale $y_i^{(\epsilon)}$ is calculated from the coarse graining process with the scale factor ϵ (analogous to a non-overlapped moving average window method). Top: coarse-grained scale of $\epsilon = 2$. Bottom: coarse-grained scale of $\epsilon = 3$.

over a broad scale factor rather than consider only single scale. Costa defined this entropy curve as a "complexity profile" of a system, however, due to a variety of definitions of the term 'complexity' [45, 46, 47, 48], it is reasonable to use the term "structural complexity" whereby the term 'structures' mean the patterns of the embedding vectors [37, 38, 39], and the term complexity means degrees of regularity/irregularity [12, 30, 31, 33, 34] or degrees of uncertainty [13, 49, 50] quantified through an entropy curve over meaningful scale factors [15, 43]. The MSE method has been successfully applied across biomedical research, such as in fluctuations of the human heartbeat under pathological conditions [15], EEG and MEG in patients with Alzheimer's disease [51], complexity of human gait under different walking conditions [52]. Recently, Ahmed and Mandic [53, 44] extended the original MSE to suit multivariate/multichannel recordings. To that cause, they proposed a multivariate sample entropy (MSE) algorithm for performing multiscale entropy analysis simultaneously over a number of data channels. This extension, termed the multivariate multiscale entropy (MMSE) [53, 44], was shown to cater for linear and/or nonlinear within- and cross-channel correlations as well as for complex dynamical couplings and various degrees of synchronization over multiple

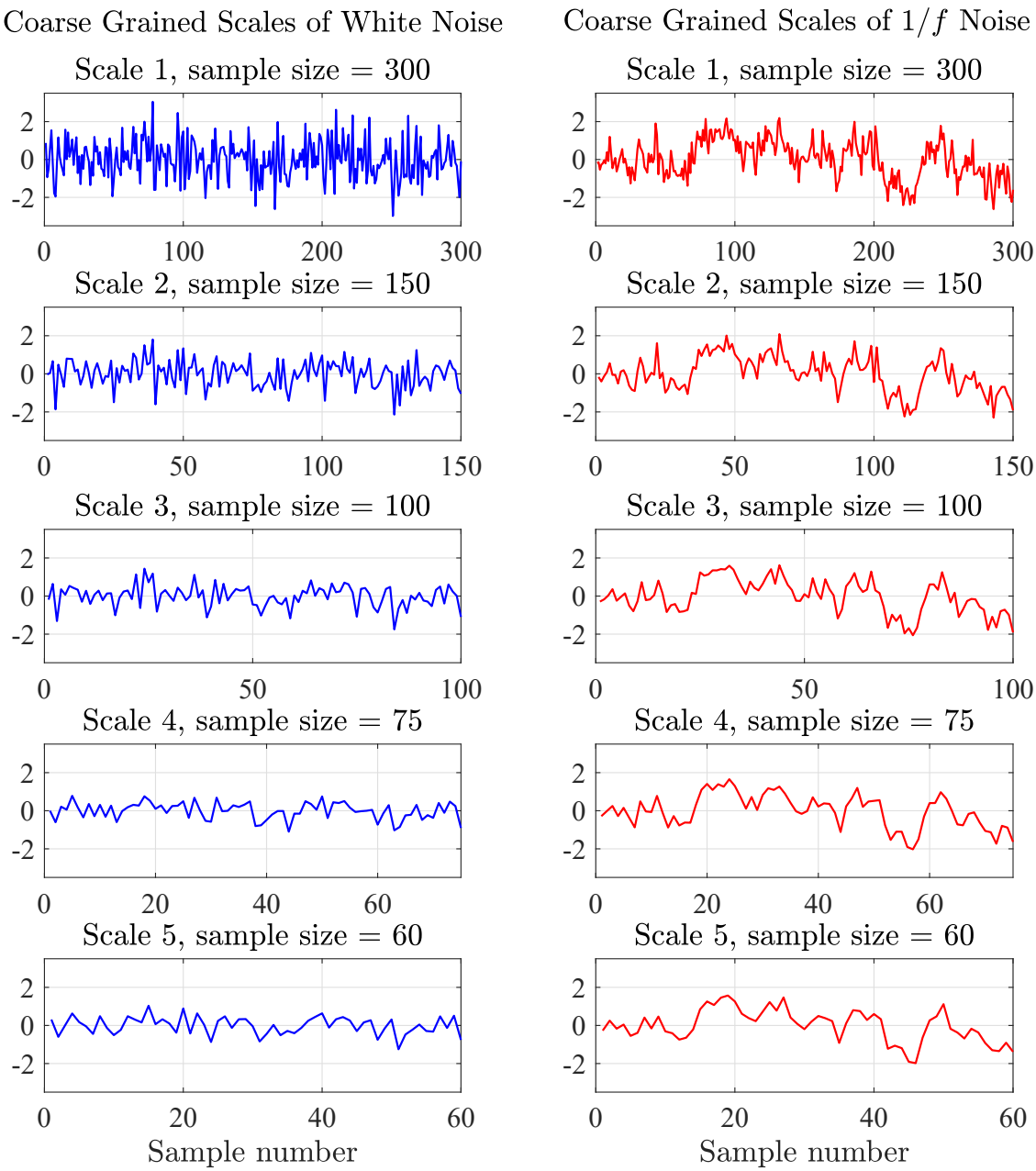

Figure 1.10: **Coarse gaining process (CGP) applied to the 300 samples of random white noise and $1/f$ noise**. Left: the coarse-grained scales of the random white noise with the given scale factors from 1 to 5 (top to bottom). Right: the coarse-grained scales of the truly complex self-similar and infinitely repeating $1/f$ noise with the given scale factors from 1 to 5 (top to bottom). Observe the higher the scale factor the lower the number of samples generated from the CGP. The coarse-grained scales also reflect the low pass filtering of the original data since the method is based on the non-overlapping moving average [44].

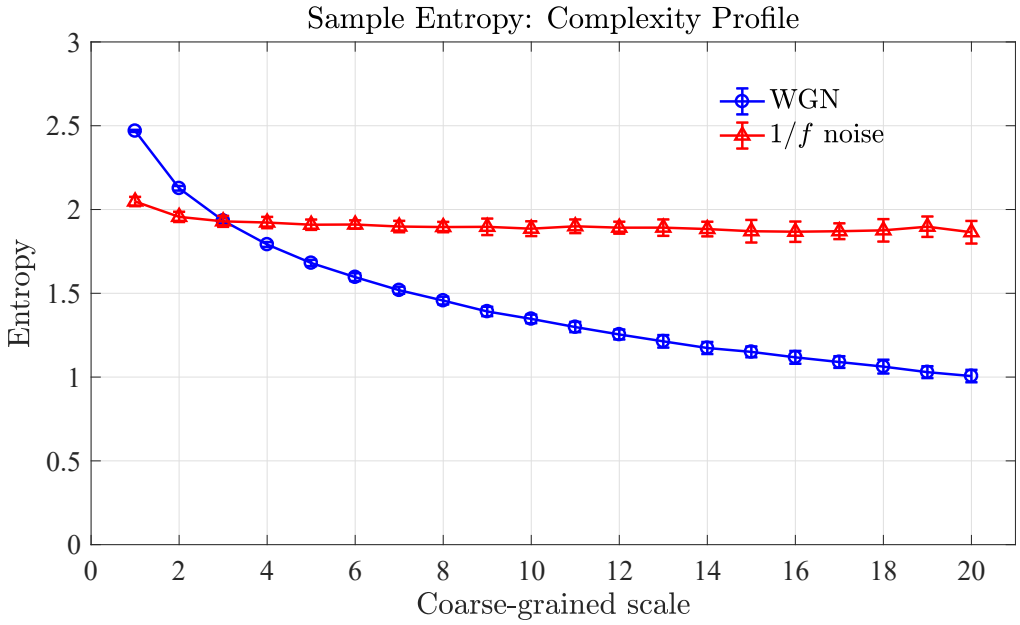

Figure 1.11: **Complexity profile of white Gaussian noise and $1/f$ noise through sample entropy**.The 20 independent realizations with 10,000 samples were generated for the white Gaussian noise and $1/f$ noise. The sample entropy with a given embedding dimension $m = 2$ and a given time lag $\tau = 1$ is applied to both noises. The mean entropies with their standard deviations are plotted against the 20 coarse-grained scales. Observe an increase in the scale factor, the entropy of random noise decreases, while the entropy of the $1/f$ noise remains constant over the whole range of scale factors.

scales, thus allowing for a direct analysis of multichannel data.

Figure 1.12 shows two illustrative examples of structural complexity: i) distribution of stars, and ii) mixing process of two substances, changing over a spatial and temporal scales. The distribution of stars consists of three images: i) random stars, ii) a structural galaxy (comprised of multiple systems), and iii) multiple galaxies, which are obtained from a telescope with fine, medium and coarse resolutions respectively. These correspond to low (no structure), high (a structural galaxy) and low (few structures) degrees of structural complexity. The mixing process of ink and water over time (temporal scale) can be described as follows. In the beginning (short period), the two substances are separated, so this state is considered as low complexity (few structures). When the ink and the water start mixing, the ink gradually diffuses through the water; forming

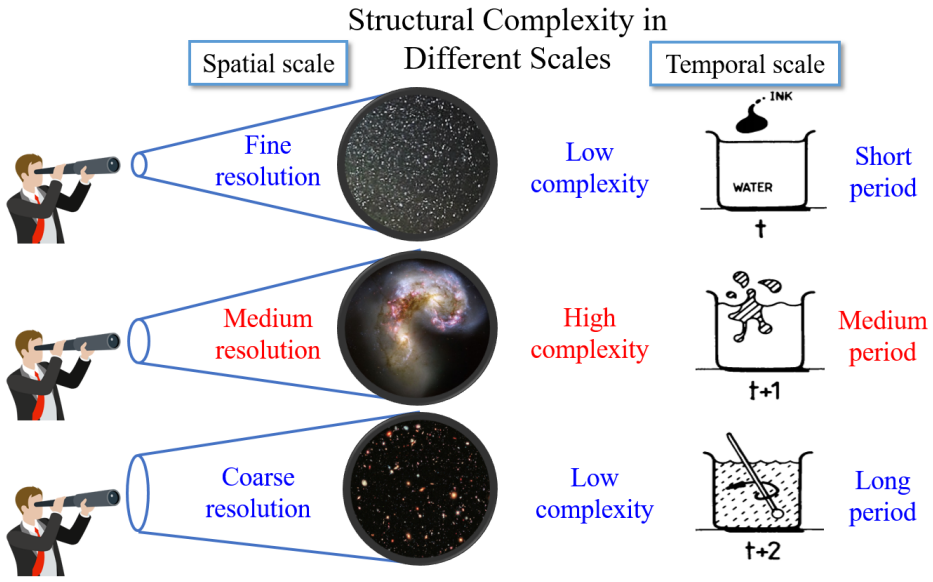

Figure 1.12: **A concept of structural complexity**. Left: from top to bottom, three images: i) random stars, ii) a structural galaxy (comprised of multiple systems), and iii) random galaxies, are obtained from a telescope with fine, medium and coarse resolutions. These correspond respectively to low, high and low degrees of structural complexity. Right: from top to bottom, three states of a mixing process between ink and water: i) separation, ii) diffusion, and iii) homogeneity are revealed over short, medium and long period of time. These correspond respectively to low, high and low degrees of structural complexity. This Figure is modified from [54].

complex structures, and hence this state is considered as high complexity. Finally, when both substances are completely mixed within a long period of time, they become homogeneous and is considered as low complexity (no structure) [54].

1.4 Complexity Loss Theory and Efficient Market Hypothesis (EMH)

This nonparametric metric [35, 55] is conveniently interpreted though the complexity loss theory [27], which asserts that physiological responses in organisms under constraints (illness, aging, and other inhibitions such as stress) exhibit lower structural complexity (fewer degrees of freedom) than physiological

responses in healthy organisms [15]. Among the available entropy measures, the sample entropy (SE) methods are particularly interesting; low levels of SE indicate a time series of high regularity, while high level of SE correspond to a greater degree of irregularity [13]

The efficient market hypothesis (EMH) is a cornerstone of modern financial theory and states that current security prices (the underlying value of the asset) incorporate and reflect all relevant information (news and regional/international regimes) that could be gathered, so that stocks always trade at fair value [56]. This implies that in normal situations markets cannot be consistently beaten over long time; in other words, the security prices tend to exhibit a random walk type of behaviour, characterised by poor predictability from their historical values and high uncertainty in the rate of change of stock prices. However, when abnormal situations occur, the buyers tend to overestimate stock values while anticipating the growth or recession of markets, which in turn brings less uncertainty to the rate of change of future prices.

1.5 Aims of Research

This thesis aims to

1. Model/quantify physiological stress levels in humans based on the theory of complexity loss and general adaptation syndrome;
2. Identify/capture stress patterns (crises) in economics based on the complexity loss theory and efficient market hypothesis;
3. Develop a new entropy-based complexity measure for quantifying structural complexity of dynamical systems in the context of self-correlation.

1.6 Original Contributions

- A robust R-peaks detection algorithm, namely "Matched Filtering-Hilbert Transform" (MF-HT). The approach is robustly able to detect R-peaks of wearable ECG recordings, which is noisy and contains movement artefacts, while the standard "Pan-Tompkins" approach is sensitive to such noise and atefacts; resulting in lower accuracy compared to the MF-HT. This algorithm was published in an IEEE conference [57] and is outlined in Chapter 2.

- The novel entropy measures, namely "Cosine Similarity Entropy" (CSE) and "Multiscale Cosine Similarity Entropy" (MCSE). The CSE and the MCSE are able to quantify structural complexity for a short length of data and yield physically meaningful interpretation in the context of self-correlation in systems with different degrees of freedom. , unlike the standard SE and MSE which yield undefined entropy for short samples and give inconsistent entropy values when applied to such systems. These approaches was publishes in the Entropy journal [58] and are outlined in Chapter 3.

- A novel analysis framework for modelling evolution of individual stress (in human). The proposed framework enables modelling evolution of stress in a subject who performs public speaking, and yields a meaningful interpretation in terms of physiological stress corresponding to the complexity loss theory. The framework was published in an IEEE conference [59] and is outlined in Chapter 4.

- A rigorous analysis framework for quantifying stress in a public performance. The framework was successfully used for quantifying stress levels of a group of musicians who perform in high and low stress scenarios, and yields a meaningful interpretation of stress levels corresponding to the complexity loss theory. The framework was published in the PLOS ONE journal [60] and is outlined in Chapter 5.

- An enhanced multivariate entropy measure, namely "Moving-average Multivariate Sample Entropy" (MA-MSE). The MA-MSE brings complexity science to the analysis of financial indices and makes it possible to model financial stress in connection with the occurrence of economic crises, based on the complexity loss theory and efficient market hypothesis. This algorithm was published in an IEEE journal [61] and is outlined in Chapter 6.

1.7 Thesis Organisation

- **Chapter 2: Enabling R-peak Detection in Wearable ECG**. This chapter describes the MF-HT algorithm used for detecting R-peaks in noisy ECG, i.e. ECG recorded from wearable devices. The background of matched filtering and Hilbert transform are provided. Comparison of performance and accuracy between the MF-HT and the standard Pan-Tompkins when applied to real-world recordings (clean and noisy ECG) is revealed.

- **Chapter 3: Standard Entropy Measures and an Introduction to Cosine Similarity Entropy**. This chapter introduces the standard entropy-based complexity measures; SE, FE, MSE and MFE. The review of limitations of the standard approaches, and the introduction of novel entropy measures; CSE and MCSE are explained. This includes the backgrounds of angular distance, the Shannon entropy and the coarse-grained scale. Comparison of the performances among the SE, FE and CSE as a function of embedding dimension, sample size is depicted. Complexity profiles over synthetic noises, signal-generation systems, and real-world heart rate variability though the MSE, MFE and MCSE are evaluated.

- **Chapter 4: A Novel Framework for Modelling Evolution of Stress for a Case Study: Public Speaking.** This chapter describes a new

analysis framework used for modelling evolution of stress in a real-life scenario (individual): public speaking. The concept of the framework including the two robust pre-processing methods: i) the MF-HT, and ii) HRV detrending is explained. Details of experiment and data collections are provided. The results of the analysis are revealed and discussed.

- **Chapter 5: Stress Analysis though Entropy-based Complexity Measures for a Case Study: Music Performance.** This chapter describes a robust framework for quantifying stress in music performance. The review of complexity loss theory, pros and cons of time- and frequency-measures vs nonlinear/complexity measures is provided. Details of experimental protocol, data collections and analysis results are revealed and discussed.

- **Chapter 6: Analysis of Financial Data through Complexity Science.** This chapter introduces a concept of the efficient market hypothesis linked to complexity loss theory. The standard multivariate entropy measure (MMSE) and the proposed MA-MSE method used for quantifying multivariate financial indices are described. Details of obtained data and results of MA-MSE are provided. Furthermore, the new method, "Assessment of Latent Index of Stress" (ALIS), is introduced for the examination of stress in individual market. The results of the ALIS and their interpretations in terms of stress-related financial crises are revealed and discussed.

- **Chapter 7: Conclusions and Future Work**. Concluding remarks drawn from the thesis and ideas for future works are outlined in this chapter.

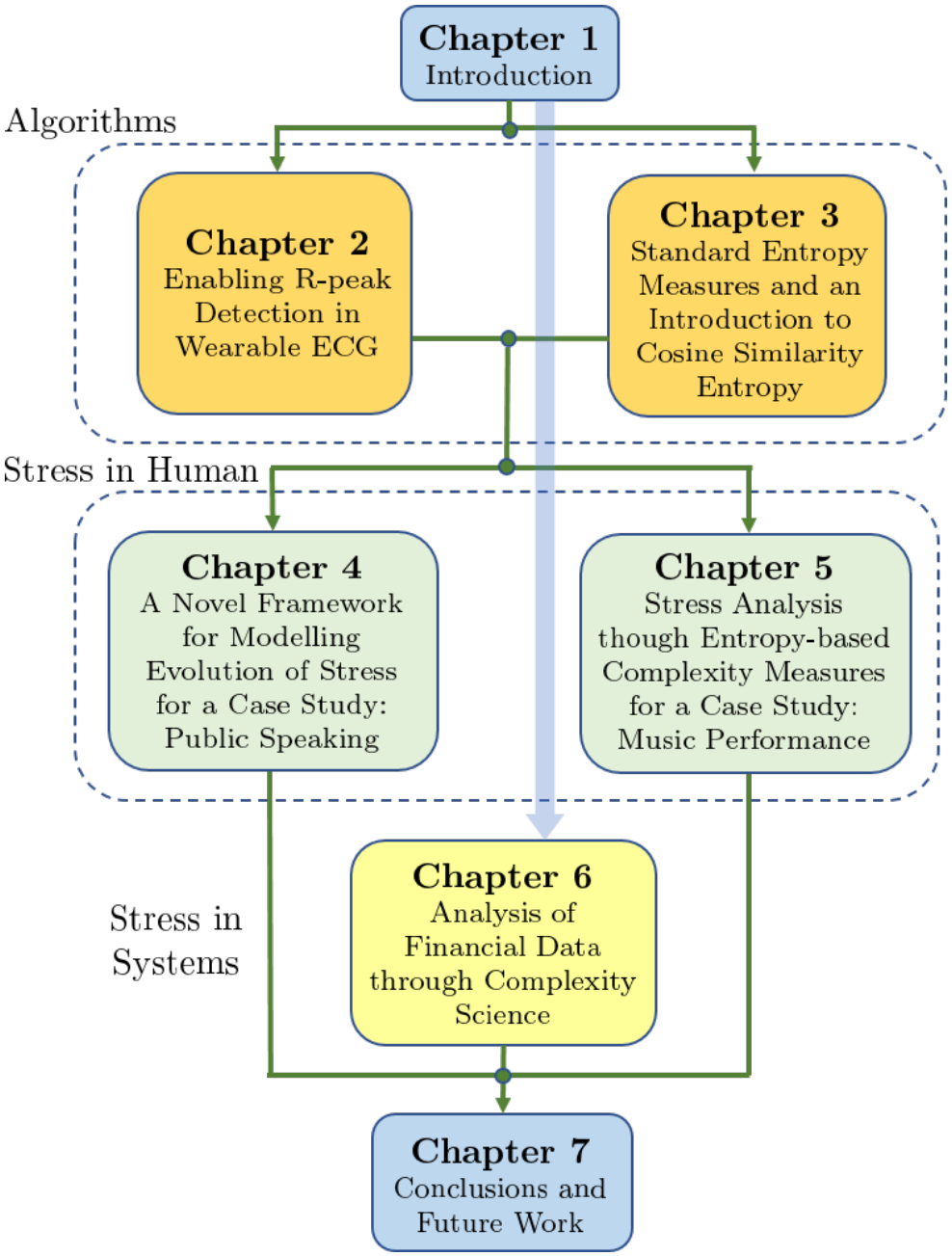

Figure 1.13: **Thesis structure**. Two main proposed algorithms: i) MF-HT, and ii) CSE and MCSE (Chapter 2 and 3) are provided for analysing stress (in human) of two study cases: i) public speaking, and ii) music performance (Chapter 4 and 5), while the proposed MA-MSE method is implemented for studying the financial stress (Chapter 6).

Chapter 2

Enabling R-peak Detection in Wearable ECG

2.1 Introduction

Heart rate variability (HRV) is an important parameter for evaluating physiological mechanisms. An example of using the HRV is to measure the balance between sympathetic and parasympathetic nervous systems, where the power ratio of low and high frequencies in the HRV frequency spectrum and the sample entropy of the HRV can indicate the level of stress [62]. The electrical currents flowing through the heart muscle while triggering its contractions can be measured on the body surface. In the obtained electrocardiogram (ECG), the most prominent segment in every ECG cycle is the QRS complex, a term for the combination of three peaks of ECG which occur owing to the depolarization of the right and left ventricle which is characterised by a sharp waveform with a high amplitude (see Figure 2.1). The R-peak is the point with the maximum amplitude in this interval. The time period between two consecutive R-peaks, the RR-interval, is commonly used to calculate the heart rate and its variability over time. However, artefacts in the signal produce a number of ambiguous peaks that can potentially be the R-peak in the ECG-cycle. In stationary and wearable ECG, the causes of artefacts are mostly moving and inadequately attached electrodes [63]. Other sources of physiological signals, such as muscle contractions, also induce interfering signals. Especially when examining the HRV, the localisation of R-peaks in the ECG needs to be precise, and in case of uncertainties, they need to be examined visually by the user [63].

The extraction of R-peaks using matched filtering has been studied for many years. One approach [65] uses the QRS complex as a pattern and searches for similarities in the ECG. To remove nonlinear and nonstationary components in

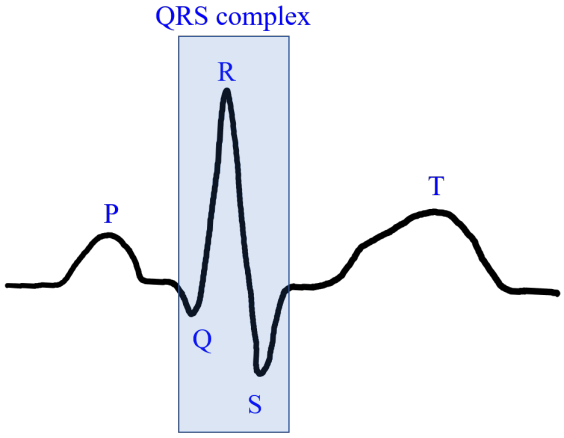

Figure 2.1: **QRS complex of a standard ECG waveform.** The significant peaks of electrocardiogram consist of the P, Q, R, S and T (from left to right). The QRS complex is defined as a prominent interval from the peak Q to S which occurs due to the depolarization of the right and left ventricles of the heart.

noisy ECG, matched filtering was combined with an artificial neural network [66] and yielded a high accuracy when applied to ECG with arrhythmia obtained from the Physionet database (namely the MIT/BIT arrhythmia database). In [67, 68] matched filtering was implemented in a hardware digital signal processing unit for a real-time R-peak detection. Another approach [69, 70] applies the Hilbert (HT) transform for extracting an ECG envelope where the R-peaks were located at the maximum amplitude of the envelope. A narrow bandpass filter (8-20 Hz) is applied to eliminate motion artefacts and muscle activity and the derivative is utilised to remove the baseline drift [71, 72]. The approach by Pan and Tompkins (PT) [73] exhibits a high sensitivity for the R-peak detection – approximately the same as the five other algorithms compared in [74] – and its source code is publicly available. It will be used to evaluate the performance of the approach presented in this study.

Apart from such approaches for the R-peak detection, there also exist the approaches for the QRS complex detection, for instance, a wavelet-based QRS detection, neural network approaches and the QRS detection based on maximum a posteriori (MAP) estimation reported in [75]. However, these approaches are

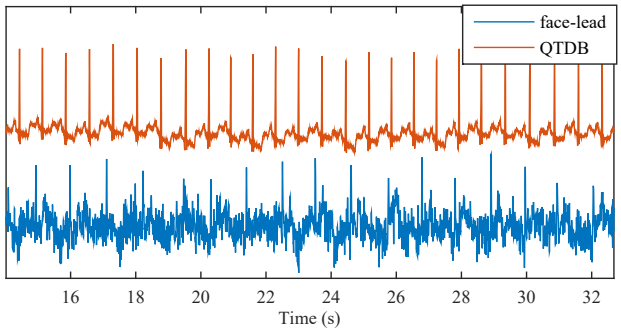

Figure 2.2: **The two ECG databases (clean and noisy).** Above: ECG obtained from the QTDB (a Physionet database consists of 105 fifteen-minute and includes a broad variety of QRS and ST-T morphologies [64]) with a high SNR. Below: face-lead ECG with a low SNR (the amplitudes are not to scale and the sets were recorded independently). Both types of ECG signals were used to evaluate the performances of the proposed MF-HT and the PT.

usually performed on ECG data acquired from stationary devices in hospitals; new methods are therefore needed for real-world data, such as (noisy) ECG data obtained from wearable devices. This study proposes a new method which combines the matched filtering and Hilbert transform (MF-HT) approaches. The former is used to find a number of potential QRS which are similar to a template QRS pattern and the exact R-peaks are located by the latter. The approach utilises a single QRS pattern manually selected once to avoid artefacts when estimating the QRS computationally. In case of multiple ambiguous R-peaks, the possible occurrences in time are limited by a dynamical time window which depends on the standard deviation of previously detected RR-intervals. Subsequently, the selection of the R-peaks is computed using the cross correlation between potential QRS and the template.

Another aspect of this work is to offer the R-peak detection software to users and researchers in medicine or psychology. The extraction and editing of the HRV from ECG data is facilitated by an interactive graphic user interface (GUI). The design of the software allows users to configure three important parameters: i) the range of the ECG data of interest; ii) a template QRS pattern; and iii) the percentage error of the RR-intervals. The main feature is the automated R-peak

search using the MF-HT algorithm and the simultaneous computation of the RR-intervals. The R-peak detection runs automatically until an uncertain peak is found. The program pauses and the user can select the R-peak from various choices: i) one of the suggested peaks as identified by MF-HT; ii) manually selecting a peak; or iii) ignoring the detected peak. The ECG, detected R-peaks, and the calculated RR-intervals are continuously displayed graphically. Furthermore, a window in the software allows the user to enlarge an area to observe potential R-peaks in detail. The software can import .mat, .csv and .txt file formats and saves the results and configuration settings in .mat and .txt files.

2.2 Matched Filtering and Hilbert Transform

Before proposing an algorithm for detecting R-peaks in ECG, the principles of the matched filtering and Hilbert transform are described below.

2.2.1 Matched Filtering

The idea of matched filtering is to start from a defined waveform or function and to search for a similar pattern in a time series. This is performed by taking the convolution between the conjugate of the defined mother pattern $h(k)$ and the original signal $x(n)$ with length N as shown in equation 2.1.

$$y(k) = \Sigma_{k=0}^{N-k} h(k)x(n-k) \tag{2.1}$$

The result of the convolution results in a high amplitude at times when the time series resembles the mother pattern and a low amplitude elsewhere. This technique is useful for locating the QRS complex in the ECG because the R-peak usually exhibits a high amplitude and the shape of QRS is unique even in noisy intervals.

2.2.2 Hilbert Transform

The Hilbert transform is a tool used to extend a real function into the complex domain. The Hilbert transform of a real function, $x(t)$, is generally defined using the Cauchy principal value (denoted by $p.v.$) and a time shift, τ_s, as described in equation (2.2). The transform can be defined in a convolution form (of $h(t)$ and $x(t)$, where $h(t) = p.v.\frac{1}{\pi t}$) as written in equation (2.3) and in the explicit form in 2.5. The complex form (frequency domain) of the Hilbert transform can be derived by taking the Fourier transform as given by equation (2.5) and (2.6), where the Fourier transform of the $h(t)$ is $-j(sgn(\omega))$ (sgn is the signum function). This results in a $\pi/2$ phase-lead for a negative frequency and a $\pi/2$ phase-lag for a positive frequency as presented in equation (2.7).

$$x^{(h)}(t) = H(x(t)) = \frac{1}{\pi} p.v. \int_{-\infty}^{\infty} x(\tau_s) \frac{1}{t - \tau_s} d\tau_s \tag{2.2}$$

$$x^{(h)}(t) = h(t) * x(t),\ h(t) = p.v.\frac{1}{\pi t} \tag{2.3}$$

$$x^{(h)}(t) = \frac{1}{\pi} \lim_{\varepsilon \to 0} \int_{\varepsilon}^{\infty} \frac{x(t + \tau_s) - x(t - \tau_s)}{\tau_s} d\tau_s \tag{2.4}$$

$$F(x^{(h)}(t)) = F(h(t)) \cdot F(x(t)) \tag{2.5}$$

$$X^{(h)}(j\omega) = K(j\omega) \cdot X(j\omega) \tag{2.6}$$

$$K(j\omega) = -j(sgn(\omega)) = \begin{cases} -j, & 0 < \omega < \pi \\ +j, & -\pi < \omega < 0 \end{cases} \tag{2.7}$$

The Hilbert transform can also be written in terms of a pair of real function $x(t)$ and imaginary functions ($jx^{(h)}(t)$) as shown in equation (2.8). The Euclidean norm of the complex form in equation (2.8) can be written as equation (2.9). The amplitude of the norm represents the local maxima or the envelope of $x(t)$.

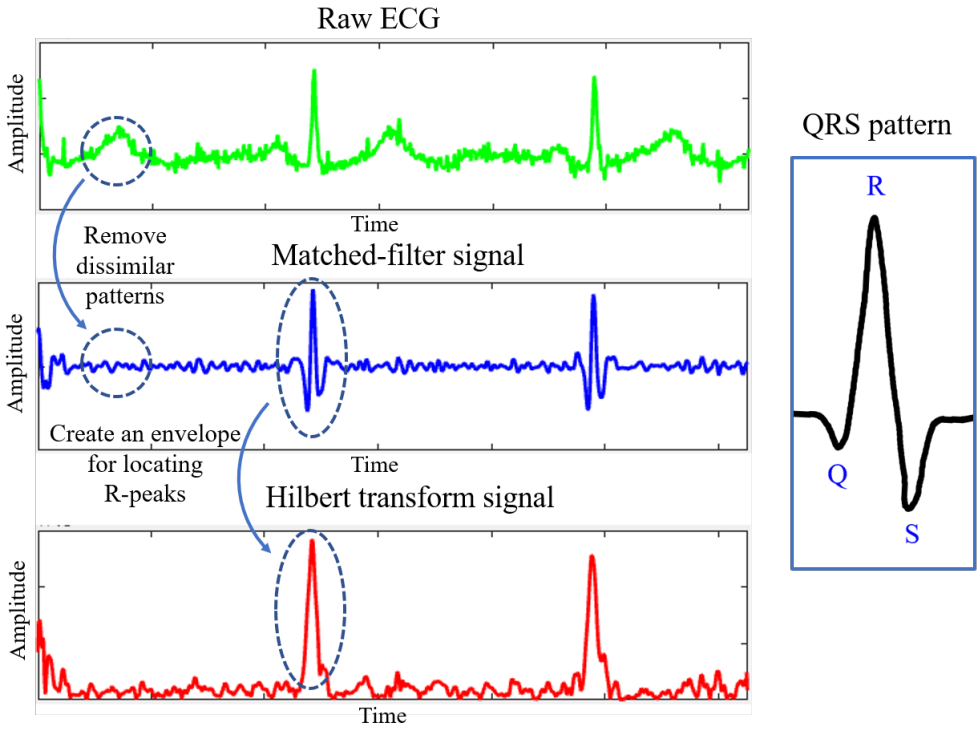

Figure 2.3: **Concept of the Matched Filtering and Hilbert transform (MF-HT) approach**. A QRS pattern is selected from the raw ECG data (top) and used in the matched filtering step. Dissimilar patterns are removed after applying matched filtering (middle). Envelope extraction is then performed using the Hilbert transform for locating R-peaks (bottom).

Applying the HT to $x(t)$ and its norm $|s(t)|$ result in a positive envelope of the signals (ECG) conveniently to locate the R-peak within a specific time window.

$$s(t) = x(t) + jx^{(h)}(t) \tag{2.8}$$

$$|s(t)| = \sqrt{x^2(t) + (x^{(h)})^2(t)} \tag{2.9}$$

The concept of combining the MF and HT methods for identifying R-peaks in ECG data (with a pre-defined QRS complex pattern) is illustrated in Figure 2.3.

2.3 A Proposed Algorithm for R-peak Detection

The MF-HT algorithm is performed on shifting time windows for the length of the ECG time series. The approach can be divided into three main steps: preprocessing, R-peak detection, and peak examination as shown in Figure 2.4. During the preprocessing, a notch filter (band stop) of the power line frequency (50 Hz) and a filter with a pass band of 8-30 Hz, the frequency range composing the QRS [71, 72], are applied to the original ECG data. Both filters are 6^{th} order IIR Butterworth filters. The QRS pattern QRS_{pt} is manually selected by the user within the GUI. For the R-peak detection, two time windows are created. The trend is removed in the first with its range set to 2.5 seconds which spans over more than one ECG cycle and is large enough to estimate the local trend. A differential of consecutive samples and a median subtraction are applied to the data in the window and to QRS_{pt}. The second time window is created inside the first with a smaller duration to limit the minimum and maximum heart rate. It starts at 20% of and ends at 150% of the mean of the cumulative RR-intervals, RR_{mean}, after the last identified R-peak. The first RR-interval is set to 1 second. Therefore, the constraint for the R-peaks covers a heart rate ranging from 67% to 500% of the mean heart rate and this range is dynamically updated depending on the variation of the underlying RR-intervals. Matched filtering and Hilbert transform are applied to QRS_{pt} and the ECG data in the first window. The result from MF-HT is used to locate potential R-peaks within the second window using a minimum time threshold of $0.2 \times RR_{mean}$ to avoid physically impossible R-peaks. The length L of QRS_{pt} (in sampling points) is used to define new intervals spanning from the centre of the potential R-peaks, $QRS_{pp}(j)$, by $\pm L/2$ to both sides where j is the index of potential peaks. The root mean squares of the cross correlation between the QRS_{pt} and each $QRS_{pp}(j)$ are computed. This results in the degree of similarity $C_{rms}(j)$ for each j. The highest value of

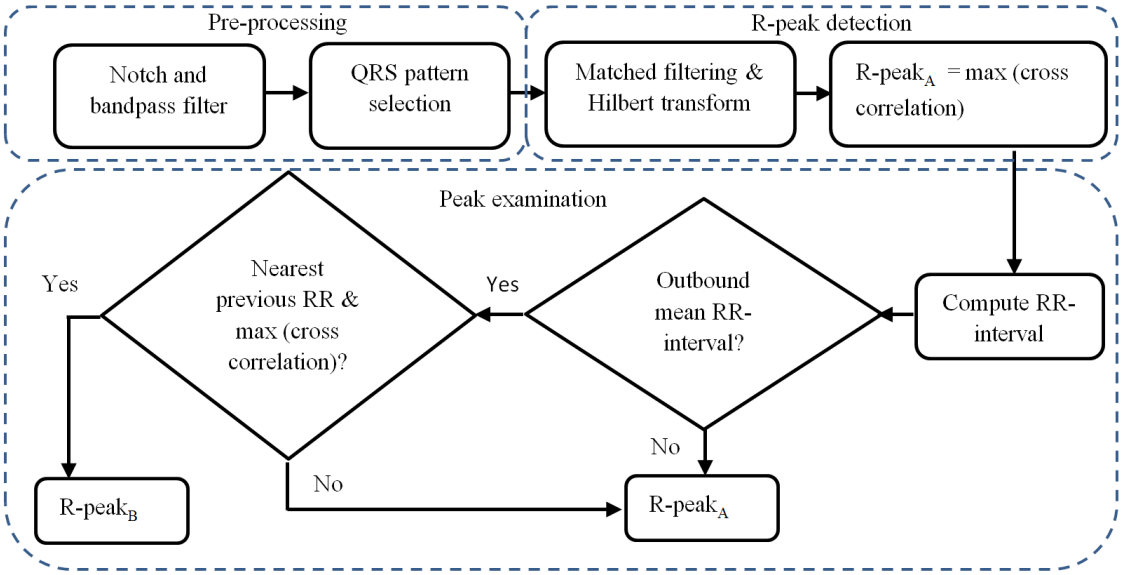

Figure 2.4: **The flow chart of the matched filtering and Hilbert transform (MF-HT) algorithm.** The MF-HT algorithm consists of three parts: Pre-processing, R-peak detection and peak examination. The MF-HT is established based on the combination of the matched filtering method and the Hilbert transform.

$C_{rms}(j)$, $C_{rms}(j_{max})$, is automatically chosen and selected as first R-peak, R-peak$_A$. The RR-interval is calculated as the temporal distance between the current and the previous R-peak. The second examination becomes effective when the recently computed RR-interval differs from the defined error. This error is calculated from the standard deviation of the cumulative RR-intervals multiplied with the user-defined weight value. In the second examination, if a peak j in $QRS_{pp}(j)$ – where R-peak$_A$ is excluded – leads to the closest RR-interval compared to the previous one and also exhibits a high $C_{rms}(j)$ among the remaining possible peaks, the peak j, R-peak$_B$, is selected instead of the previous one. The MF-HT can be summarised in Algorithm 2.1

Algorithm 2.1. Matched Filtering and Hilbert Transform (MF-HT)

For the length N of the ECG data $x(k)$ the MF-HT algorithm can be summarised in the following iteration steps:
While $k \leq N$

1. Create the first time window of filtered ECG data with a length of 2.5 seconds, beginning at the current R-peak.
2. Remove the local trend of the first window by taking the differential and subtracting its median from the data.
3. Define the second window ranging from $0.2 \times RR_{mean}$ to $1.5 \times RR_{mean}$ after the previous R-peak.
4. Apply matched filtering to the QRS_{pt} and the data in the first window.
5. Apply the Hilbert transform to the result from 4).
6. Find potential peaks using a minimum time threshold of $0.2 \times RR_{mean}$
7. Create $QRS_{pp}(j)$ by expanding by $\pm L/2$ from the centre of each potential QRS to both sides.
8. Calculate cross correlation between QRS_{pt} and $QRS_{pp}(j)$ and take their root mean square resulting in $C_{rms}(j)$. $max[C_{rms}(j)]$ at j_{max} is selected to be the R-peak$_{\mathrm{A}}$ at $QRS_{pp}(j_{max})$.
9. Calculate the current RR-interval.
10. If the RR-interval is outside of the predefined error, compute RR-intervals of all j of $QRS_{pp}(j)$, where R-peak$_{\mathrm{A}}$ from 8) is excluded.
11. If the potential peak j results in the closest RR-interval value compared to the previous RR-interval and has $max[C_{rms}(j)]$ among the rest, it is selected as R-peak$_{\mathrm{B}}$ replacing R-peak$_{\mathrm{A}}$.

The GUI of the software is shown in Figure 2.5.

2.4 Performance Evaluation and Results

The algorithm was evaluated on two different databases: i) a standard database from PhysioNet [76], the QT database (QTDB) [64]; and ii) a set of recordings partially used in [77] (their examples were depicted in Figure 2.2). The latter were

Figure 2.5: **Software for R-peak extraction using the MF-HT algorithm**. Four windows are designed to visualise: ECG and identified R-peaks, the RR-intervals, a close-up R-peak examination with suggested choices, and the QRS pattern selection and settings.

recorded with a wearable device, a motorbike helmet and show a lower signal-to-noise ratio (SNR) (Figure 2.2). In the first case, only the first channel was used and in the second case, one exemplary channel, a bipolar measurement between the two sides of the jaw, was selected. Out of the first 34 datasets in the QTDB (107 datasets in total), four were excluded for the following reasons: the annotations were missing for large parts of the file, the annotations were incorrect, or the annotations were inconsistent, i.e. they alternated between different parts of the QRS-intervals – in some instances the markers were closer to the Q-peaks, in other closer to the S-peaks).

After scanning the two databases for R-peaks, the detected positions in time were classified using a reference. For the QTDB, the supplied annotations were used and for the second database, a simultaneous recording of ECG obtained from the arms was utilised. Its peaks were well defined and its occurrences in time were verified visually. An R-peak was classified as correctly identified if the time

difference between the R-peak in the reference and the R-peak as identified by the algorithms is smaller or equal to 20 ms which corresponds to approximately 2% of the duration of an average ECG cycle. Afterwards, the results were quantified using the parameters Sensitivity (Se) and positive predictivity ($+P$) [75]:

$$Se = \frac{TP}{TP + FN} \qquad +P = \frac{TP}{TP + FP}$$

where TP represents the number of correctly identified R-peaks, FN the number of missed R-peaks and FP the number of points falsely labelled as R-peaks.

However, in the case where the algorithm consistently identifies R-peaks wrongly due to noise or movement artefacts, further parameters are considered: i) the deviation of the RR-intervals (RRID) as obtained from the R-peak detection algorithms from the RR-intervals of the reference signal; and ii) the analogue value for the heart rate deviation (HRD). This is quantified via the root-mean-square error of the difference between the two values at every second. The smaller the value, the more accurate was the detection of R-peaks. An example where the second method excels is the case sel808 in the QTDB. The markers for all R-peaks are positioned too early in the signal (closer to the Q-peaks). Therefore, Se and $+P$ were less than 8% for the MF-HT. However, the RRID and the HRD are comparatively low – 47 ms and 2.0 bpm. While results for the HRD are more intuitive, since it is common to state the pace of the heart in beats per minute and not the average time interval between two heart beats, it is more prone to misleading results. For example, when a false R-peak was identified close to a real R-peak, the resulting heart rate will be mistakenly very high due to taking the inverse of a short time period. This explains why the values RRID and HRD in Table 2.1, row MF-HT, do not show corresponding results.

The algorithm presented here was compared to a well established method by Pan and Tompkins [73]. The results for the two databases are displayed in Table 2.1

Table 2.1: **Comparison of performance between PT method and our proposed MF-HT method on standard ECG data**. Both approaches were tested on 30 datasets QTDB (relatively clean ECG) obtained from Physionet database. The computational time (Comp. time) is measured in Matlab which is used to implement both algorithms.

Algorithm	Se	+P	RRID(ms)	HRD(bpm)	Comp. time(ms)
PT	91.2%	91.2%	1779.8	7.6	652
MF-HT	95.3%	93.5%	235.8	9.6	5347

Table 2.2: **Comparison of performance between PT method and our proposed MF-HT method on noisy wearable ECG data**. Both approaches were tested on 6 datasets with lower SNR. The computational time (Comp. time) is measured in Matlab which is used to implement both algorithms.

Algorithm	Se	+P	RRID(ms)	HRD(bpm)	Comp.time(ms)
PT	86.6%	49.6%	408.4	105.9	111
MF-HT	83.1%	86.8%	140.8	11.5	1817

and Table 2.2. For the QTDB, the MF-HT achieved higher values for Se and $+P$ and furthermore resulted in a smaller value for RRID. Since the MF-HT performed better according to the three mentioned parameters, it can be concluded that the higher value for HRD was due to an effect caused by inverting the RR-intervals to obtain the heart rate (as explained above).

The second set of ECG recordings measured with a mobile device, features a lower SNR due to electrodes placed on the head instead of the chest or the limbs. Therefore the performance of both methods was reduced. The Se of PT was a few percentage points higher than the Se of the MF-HT. However, overall PT listed significantly more R-peaks that do not exist which lead to a low value for $+P$. The same behaviour is perceptible in the columns RRID and HRD: the deviation of the estimated RR-intervals and the heart rate from the real values was substantially lower for the MF-HT compared to the PT.

The observation that the Se and $+P$ of the MF-HT are in general lower than

in other publications (e.g. in [75]), can probably be explained by assuming that this study is more strict towards the time difference between the actual and the estimated R-peak to classify the detection as correct.

2.5 Conclusions

A robust R-peak detection method has been established based on a combination of the matched filtering and the Hilbert transform (MF-HT). The RR-intervals and cross-correlation have been employed in conjunction to not only automatically locate the R-peaks but also to display the candidate ambiguous peaks via an interactive graphical user interface (GUI). The MF-HT approach has been evaluated by implementing two types of ECG databases: i) standard clean ECG, and ii) low signal to noise ratio ECG (noisy ECG) obtained from wearable ECG. The performance of the approach has been compared to the performance of the well-known Pan-Tompkins algorithm. The proposed MF-HT has shown a distinctly higher positive predictivity and has led to more satisfying overall outcomes, especially for the critical call of noisy ECG.

2.6 Future work

Future work will include the verification of these results on additional standard ECG databases and real-world ECG obtained from a variety of wearable devices. Nonlinear techniques for eliminating baseline wander and movement artefacts in noisy ECG will be investigated to the improvement of the accuracy of the R-peak detection. The HRV estimation (from RR-intervals) and HRV cleaning process will be included. Moreover, a user-friendly GUI for the approach will be designed and implemented.

Chapter 3

Standard Entropy Measures and an Introduction to Cosine Similarity Entropy

3.1 Introduction

Entropy-based structural complexity assessment is one of the most important nonlinear analysis tools for quantifying degrees of regularity/irregularity in signals and systems. However, observational data from real-world systems usually exhibit nonlinearity and/or nonstationarity, so that standard linear metrics and standard descriptive statistic, such as mean, standard deviation, time or frequency domain analysis, fail to reveal genuinely intrinsic characteristics [27, 28]. A well-known statistical entropy method, called Approximate Entropy (ApEn) [12, 30, 31, 32, 33, 34], has therefore been developed particularly for the analysis of physiological signals, such as heart rate variability (HRV). Such an approach is based on the statistics of occurrences of similar patterns in a time series. These are found in reconstructed elements, so-called embedding vectors, which preserve the underlying dynamical properties of the system when an appropriate embedding dimension (m) is chosen [37, 78]. The Sample Entropy (SE) estimator, proposed by [13], is an improved version of the ApEn, whereby the occurrences of the self-similar patterns are not considered; this results in unbiased entropy estimates; this enhanced robustness has made the SE become an extremely popular in practical applications. However, there are some limitations of the SE which are related to: i) a short length of sample size, ii) spikes or erratic noise in data, and iii) unconstrained bounds on entropy values. To provide insight into these limitations and outline the proposed solutions, it is important to notice that in the SE approach, entropy is estimated based on conditional probability, whereby the probability of

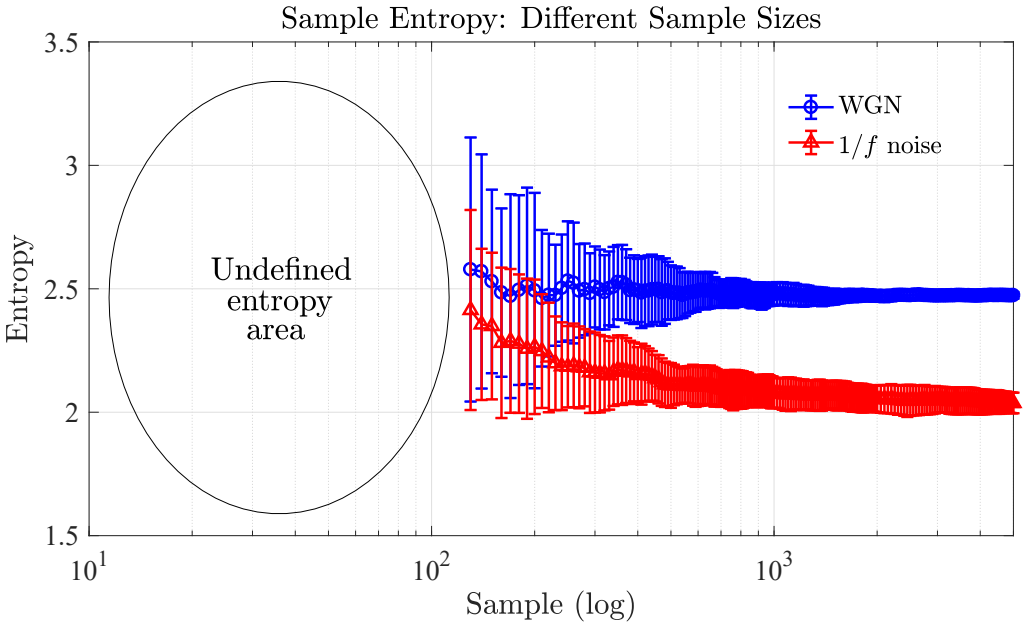

Figure 3.1: **Undefined entropy of white Gaussian noise (WGN) and $1/f$ noise**. The 30 independent realizations with data lengths from 10 to 5,000 samples were generated for WGN and $1/f$ noise. The sample entropy with a given embedding dimension $m = 2$ and a given time lag $\tau = 1$ is applied to both noises. The mean entropies with their standard deviations are plotted against data length. Observe the entropy values are undefined when the data lengths are too short (less than 120 samples). Based on sample entropy formula (see Algorithm 3.1), entropy values are calculated from the natural logarithm of the ratio between the probability of occurrences of similar patterns found in embedding vectors with a given embedding dimension m, and one with embedding dimension $(m+1)$; the ratio approaches zeros for such short data lengths and therefore results in infinite values (undefined entropy values).

occurrences of similar patterns found in the embedding vectors with a small dimension (m) is compared to the probability of the occurrences of similar patterns found in the embedding vectors with a larger dimension $(m+1)$, defined as a reference frame. This method is effective when a time series has enough samples (10^m to 30^m as a rule of thumb [79]), however for a short time series (the first issue above), undefined entropy can arise due to the convergence in probability to zero; i.e. few occurrences of similar patterns are found in embedding vectors with the dimension of either m or $(m+1)$ [80] (see Figure 3.1 for entropy values of the 30 independent realizations with a sample sizes ranging from 10 to 5,000 samples generated for WGN and $1/f$ noise). Regarding the

second issue, since the assessment of the similarity in the SE is based on the amplitude-based distance called the Chebyshev distance, spurious peaks or high amplitude of spikes[1] present in a time series directly affect such a distance metric and consequently alter a number of occurrences of similar patterns found in the embedding vectors for both the dimensions m and $(m+1)$; this results in either a reduction or increase in entropy [82, 81] and exemplifies that the rapid changes of amplitudes cause inconsistent entropy estimates. Furthermore, the estimation of entropy is based on the natural logarithm which gives an uncontrollable range entropy values for small values of the proxy for probability (the third issue above). To this end, the recent fuzzy entropy (FE), an improved version of the SE, has been proposed in [14, 40, 41, 42]. To provide more robust examination of the similarity between embedding vectors. This is achieved by replacing the Heaviside function or a hard threshold, used as a criterion in the SE, with a fuzzy membership function, such as a Sigmoid or Gaussian. The FE has been proven to be superior to the SE for short sample sizes and is robust to spikes [14]. However, the SE and FE yield different entropy estimates (for sufficient samples), whereby the FE yields lower entropy values and their variation than the entropy estimated from the standard SE.

In addition, the SE behaves monotonically with respect to the degrees of uncertainty, meaning that the higher the randomness the greater the entropy. *This implies that the SE is effectively a tool for quantifying degrees of uncertainty-based complexity* [13, 49, 50]. However, completely random signals have no structure and are therefore not complex, and the complexity should be considered in the context of (self) correlation over small to large temporal scales, as shown in the coarse-grained scales employed in the Multiscale Sample Entropy (MSE), proposed in [15, 52]. Indeed, it is the MSE that make a guarantee step forward in the way we understand and deal with complexity of real-world data.

[1]These typically present in real world data, such as in QRS complexes of the Electrocardiogram (ECG), epilepsy seizures in Electroencephalogram (EEG), movement artifacts, or any failures of recording devices or of sensors [81].

An illustrative example of the complexity analysis using the MSE is a comparison of a long-term correlated signal ($1/f$ fractal noise with a tremendous amount of structure) and uncorrelated random noise [43]. Random noise at the smallest scale factor (sample entropy) has a higher entropy than the entropy of the truly complex self-similar and infinitely repeating $1/f$ noise. However, with an increase in the scale factor, the entropy of random noise decreases, while the entropy of the $1/f$ noise remains constant over the whole range of scale factors. Finally, at the largest scale factor, the entropy of random noise reduces dramatically and is lower than that of the $1/f$ noise; *the implication of this result is the concept of the quantification of complexity based on self-correlation over small to large scale factors which is emphasized in this study.*

We proposed the algorithm called "Cosine Similarity Entropy" (CSE) and its extended multiscale version called "Multiscale Cosine Similarity Entropy" (MCSE) are based on the modification as exploiting the SE and the MSE approaches, whereby we employ Shannon entropy instead of the conditional entropy owing to its rigorous properties: i) anti-monotonicity (an increase in entropy with a decrease in probability and vice versa); ii) for a uniform distribution of probability, it exhibits a unique maximum entropy; and iii) entropy is zero only if the probability is 1 (no new information) [83]. In terms of a distance metric, we employ the angular distance, a family of the cosine similarity distances (a measure of similarity between two non-zeros vectors by calculating a norm of inner product space of the two vectors; more details are given in Section 3.3), which is an amplitude-independent-based distance. The angular distance also complies with the four axioms of the distance in metric spaces: i) non-negativity; ii) identity for indiscernibles; iii) symmetry; and iv) triangle inequality [84, 85]. We examine the characteristic of the CSE over varying tolerance levels for four synthetic signals: i) white Gaussian noise (WGN), ii) $1/f$ noise, iii) first order autoregressive model, AR(1), and iv) second order autoregressive model, AR(2). The four synthetic signals are tested

regarding their distinctive characteristics: i) the WGN represents a complete random signal (no structure), while the $1/f$ noise represents a long-term correlation signal (complex structures), and ii) the AR(1) and AR(2) represent one and two degrees of freedom of the signal-generation systems (intermediate complex structures); these four signals are hence an appropriate choice for testing their characteristics in terms of structural complexity. The effects of different embedding dimensions and sample sizes on the SE, FE and CSE approaches are also compared. For the multiscale approaches, the performances of the corresponding multiscale versions, MCSE, MSE and MFE, are investigated by evaluating the complexity profiles of these four characteristic synthetic signals over small to large scales. The effectiveness of the three multiscale approaches is finally verified on real-world heart rate variability obtained from three different conditions of cardiac pathology. Physically meaningful interpretations of these conditions based on the proposed correlation based complexity approach are demonstrated, and its enhanced robustness to short data sizes, artefacts in data as amplitude-independence and a stable range of values are verified.

3.2 Sample Entropy, Fuzzy Entropy and a Multiscale Approach

Estimation of sample entropy is based on the conditional probability of the occurrences of similar patterns in a time series, whereby similar patterns found in the reconstructed embedding vectors with a given embedding dimension (m) are compared to similar patterns found in the reconstructed embedding vectors with a higher embedding dimension ($m + 1$), regarded as a reference frame. The patterns are judged similar when a distance (Chebyshev distance, $ChebDis$) between two embedding vectors is less than or equal to a given tolerance level (r_{se}). The steps of the SE approach are summarized in Algorithm 3.1.

Algorithm 3.1. Sample Entropy

For a time series $\{x_i\}_{i=1}^{N}$ with a given embedding dimension (m), tolerance (r_{se}) and time lag (τ):

1. Construct the embedding vectors from $\{\boldsymbol{x}_i\}_{i=1}^{N}$ using
$$\boldsymbol{x}_i^{(m)} = [x_i, x_{i+\tau}, ..., x_{(i+(m-1)\tau)}]\,, i = 1, ..., N-m+1$$
2. Compute the Chebyshev distance for all pairwise embedding vectors as
$$ChebDis_{i,j}^{(m)} = max_{l=1,2,...,m}\{\boldsymbol{x}_i^{(m)}[i+l-1] - \boldsymbol{x}_j^{(m)}[j+l-1]\},\ i \neq j$$
3. Obtain the number of similar patterns, $P_i^{(m)}(r_{se})$, when a criterion $ChebDis_{i,j}^{(m)} \leq r_{se}$ is fulfilled
4. Compute the local probability of occurrences of similar patterns, $B_i^{(m)}(r_{se})$, given by
$$B_i^{(m)}(r_{se}) = \tfrac{1}{N-m} P_i^{(m)}(r_{se})$$
5. Compute the global probability of occurrences of similar patterns, $B^{(m)}(r_{se})$, using
$$B^{(m)}(r_{se}) = \tfrac{1}{N-m} \textstyle\sum_{i=1}^{N-m} B_i^{(m)}(r_{se})$$
6. Repeat Step 1 to Step 6 with an embedding vector $(m+1)$ and obtain $B^{(m+1)}(r_{se})$ from
$$B^{(m+1)}(r_{se}) = \tfrac{1}{N-m} \textstyle\sum_{i=1}^{N-m} B_i^{(m+1)}(r_{se})$$
7. Sample entropy is then estimated in the from
$$SE(m, \tau, r_{se}, N) = ln[\tfrac{B^{(m)}(r_{se})}{B^{(m+1)}(r_{se})}]$$

.

In a multiscale version of the sample entropy approach proposed by [15, 52, 43], scales are generated using the coarse graining process which is based on moving average with non-overlapped windows of a time series $\{x_i\}_{i=1}^{N}$, and yields a new, successively shorter, time series of length N/ϵ, defined as

$$y_i^{(\epsilon)} = \frac{1}{\epsilon} \sum_{i=(j-1)\epsilon+1}^{j\epsilon} x(i) \tag{3.1}$$

where ϵ represents a scale factor and $1 \leq j \leq N/\epsilon$.

For the Multiscale Sample Entropy (MSE) algorithm, only the coarse graining process is required prior to proceeding with steps in the SE. For a given scale factor ϵ, the coarse-grained scale obtained from equation (3.1) is substituted for $\{\boldsymbol{x}_i\}_{i=1}^{N}$, to serve as an input series to the SE algorithm. The estimation of the multiscale sample entropy therefore assumes the for

$$MSE(m, \tau, r_{se}, N, \epsilon) = ln[\frac{B_{(\epsilon)}^{(m)}(r_{se})}{B_{(\epsilon)}^{(m+1)}(r_{se})}] \tag{3.2}$$

where $B_{(\epsilon)}^{(m)}(r_{se})$ and $B_{(\epsilon)}^{(m+1)}(r_{se})$ are respectively the global probabilities of the occurrences of similar patterns for a given m and $(m+1)$.

Note that for $\epsilon = 1$, the coarse-grained time series is equal to the original time series, thus at this scale factor, the MSE results in an entropy which is identical to entropy estimated from the standard SE, given in Algorithm 3.1.

In the FE approach, the computational steps in the SE are replicated with two modifications: i) in the first step of the SE, reconstructed embedding vectors are centered by their own means; i.e. they become zero-mean, and ii) in the fourth step of the SE, instead of obtaining a number of similar patterns, $P_i^{(m)}(r_{cse})$, the FE obtains the fuzzy similarity, $S_i^{(m)}(r_{fe}, \eta)$, calculated from a fuzzy membership function, such as the Z-shape [86] or the Gaussian (a family of the exponential function) [14]. Similar entropy values are found when applying the FE with both functions with recommended parameters (entropy values resulting from such functions can be different depending on a selection of parameters for each function) [86], In our study, we chose the Gaussian membership function which is suggested by [14, 41]. The steps of the FE approach are summarized in Algorithm 3.2.

For the Multiscale Fuzzy Entropy (MFE) algorithm, only the coarse graining process is required prior to proceeding with other steps in the FE. For a given scale factor ϵ, the coarse-grained scale produced from equation (3.1) is

Algorithm 3.2. Fuzzy Entropy

For a time series $\{x_i\}_{i=1}^N$ with given embedding dimension (m), tolerance (r_{fe}) and time lag (τ):

1. Construct the centered embedding vectors from $\{\boldsymbol{x}_i\}_{i=1}^N$ as
   $\boldsymbol{x}_i^{(m)} = [x_i, x_{i+\tau}, ..., x_{(i+(m-1)\tau)}] - \frac{1}{i+(m-1)\tau}\sum_i^{i+(m-1)} x_i \, , i = 1, ..., N-m+1$
2. Compute the Chebyshev distance for all pairwise embedding vectors from
   $$ChebDis_{i,j}^{(m)} = max_{l=1,2,...,m}\{\boldsymbol{x}_i^{(m)}[i+l-1] - \boldsymbol{x}_j^{(m)}[j+l-1]\},\ i \neq j$$
3. Obtain the fuzzy similarity, $S_i^{(m)}(r_{fe}, \eta)$, using the Gaussian function
   $$S_i^{(m)}(r_{fe}, \eta) = e^{\frac{(ChebDis_{i,j}^{(m)})^\eta}{r_{fe}}}, \text{ where } \eta \text{ is a chosen order}$$
4. Compute the local probability of occurrences of similar patterns, $B_i^{(m)}(r_{fe})$, using
   $$B_i^{(m)}(r_{fe}) = \frac{1}{(N-m)} S_i^{(m)}(r_{fe}, \eta)$$
5. Compute the global probability of occurrences of similar patterns, $B^{(m)}(r_{fe})$, as
   $$B^{(m)}(r_{fe}) = \frac{1}{N-m}\sum_{i=1}^{N-m} B_i^{(m)} r_{fe}$$
6. Repeat Step 1 to Step 6 with the embedding dimension $(m+1)$ and obtain $B^{(m+1)}(r_{fe})$ from
   $$B^{(m+1)}(r_{fe}) = \frac{1}{N-m}\sum_{i=1}^{N-m+1} B_i^{(m+1)} r_{fe}$$
7. Fuzzy entropy is then estimated in the form
   $$FE(m, \tau, r_{fe}, N) = ln[\frac{B^{(m)}(r_{fe})}{B^{(m+1)}(r_{se})}].$$

substituted for $\{\boldsymbol{x}_i\}_{i=1}^N$, to serve as an input series to the FE algorithm. Estimation of the multiscale fuzzy entropy can be then performed based on

$$MFE(m, \tau, r_{fe}, N, \eta, \epsilon) = ln[\frac{B_{(\epsilon)}^{(m)}(r_{fe})}{B_{(\epsilon)}^{(m+1)}(r_{fe})}] \tag{3.3}$$

where $B_{(\epsilon)}^{(m)}(r_{cse})$ and $B_{(\epsilon)}^{(m+1)}(r_{cse})$ are respectively the global probabilities of the occurrences of similar patterns for given embedding dimensions m and $(m+1)$.

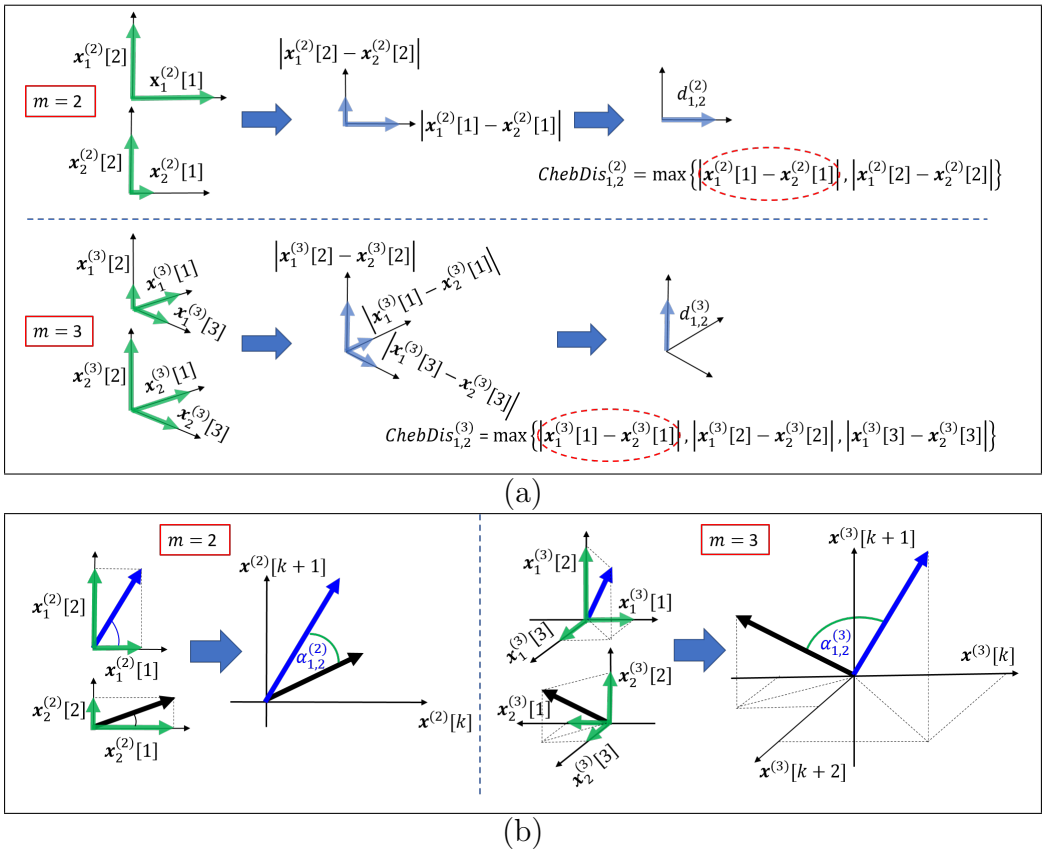

Figure 3.2: **Geometric interpretation of the Chebyshev and angular distances in Cartesian coordinates**. (a) Chebyshev distance of two embedding vectors $\boldsymbol{x}_1$ and $\boldsymbol{x}_2$, with embedding dimensions $m = 2$ and $m = 3$. Chebyshev distances are chosen from the coordinate-wise maximum amplitude difference of the two embedding vectors. (b) Angular distance of embedding vectors $\boldsymbol{x}_1$ and $\boldsymbol{x}_2$with $m = 2$ and $m = 3$; the angles $(\alpha_{1,2}^{(m)})$ and the angular distance between the two embedding vectors are calculated using equations (3.6) and (3.7).

3.3 Cosine Similarity Entropy (CSE)

Prior to introducing the proposed CSE algorithm and its multiscale version, MCSE, we shall provide an insight into the geometry of angle-based association measures of embedding vectors.

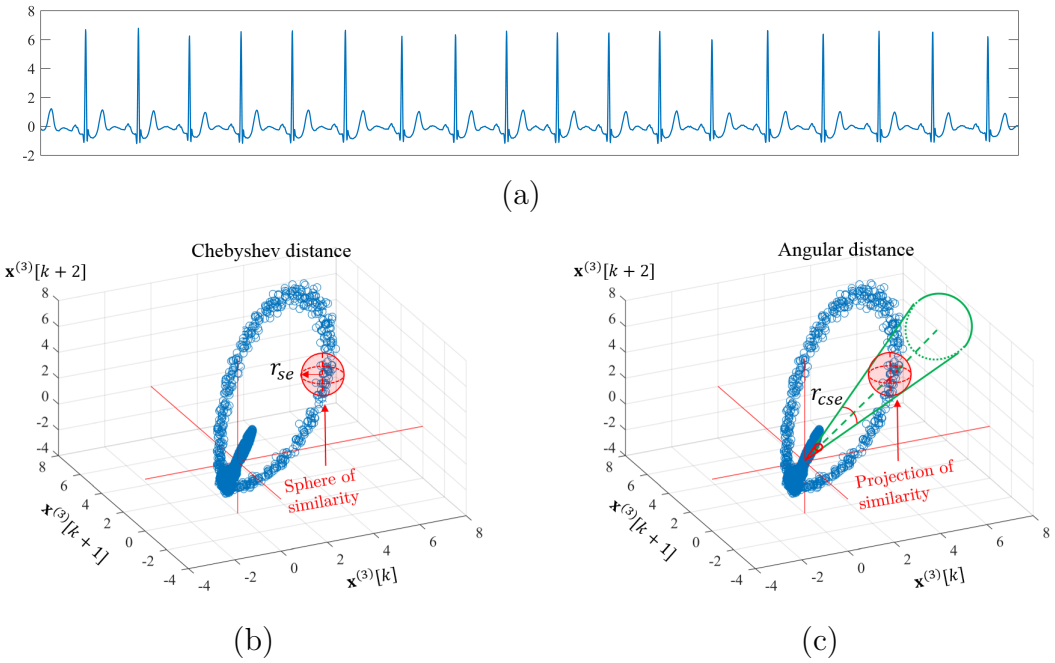

Figure 3.3: **Geometric interpretation of similar patterns in a three-dimensional phase space**. The embedding vector, $x^{(3)}$ (with a given $m = 3$), is reconstructed from an Electrocardiogram (ECG) time series. (a) Normalized raw ECG. (b) Using the Chebyshev distance with a given a tolerance r_{se} (see section 3.4.1 for more details), similar patterns are detected inside the red sphere. (c) Similar patterns, derived from the angular distance with a given r_{cse}, are detected inside the green projection cone.

3.3.1 Angular Distance

The Chebyshev distance used in the SE is obtained from the maximum amplitude difference among elements of the two embedding vectors (for a given m), however, this amplitude based distance is sensitive to spikes or erratic peaks in data. In the sense of structural similarity, it is reasonable to consider similar patterns as spans of a prototype vector, or alternatively any embedding vectors which are scaled by multiplying gains (within a given small tolerance). With this rationale, we show that the angular distance ($AngDis$), which rests upon of the angle between two embedding vectors as a distance metric, is an appropriate choice for the determination of the similar patterns in a noisy time series. The major advantage of the angular distance is its low sensitivity to any changes in

vector norms as long as the angle between the considered vectors is maintained a desired amplitude-independent-based distance.

3.3.2 Properties of Angular Distance

It is important to mention that the angular distance belongs to the family of cosine distances ($CosDis$) which are derived from the cosine similarity ($CosSim$) metric. Cosine similarity is defined as an inner product of two vectors divided by the product of their norms, giving a range from -1 to 1. To produce a distance metric allowing for only positive values, the cosine distance is simply modified by subtracting its value from 1, to yield a range from 0 to 2. *However, the cosine similarity and the cosine distance are not proper distance metrics, as they violate the triangle inequality property of a metric in normed vector spaces* [87, 88]. Namely, the properties of any valid distance should satisfy of the following. Let $\boldsymbol{a}, \boldsymbol{b}, \boldsymbol{c}$ be any vectors in a subspace of $\mathbb{R}^m$and $Dis(\boldsymbol{a}, \boldsymbol{b})$ a distance between the vector $\boldsymbol{a}$ and vector $\boldsymbol{b}$. The properties of a valid distance are: i) non-negativity ($Dis(\boldsymbol{a}, \boldsymbol{b}) \geq 0$), ii) identity of indiscernibles ($Dis(\boldsymbol{a}, \boldsymbol{b}) = 0$ only if $\boldsymbol{a} = \boldsymbol{b}$), iii) symmetry ($Dis(\boldsymbol{a}, \boldsymbol{b}) = Dis(\boldsymbol{b}, \boldsymbol{a})$), and iv) triangle inequality ($Dis(\boldsymbol{a}, \boldsymbol{b}) \leq Dis(\boldsymbol{a}, \boldsymbol{c}) + Dis(\boldsymbol{c}, \boldsymbol{b})$) [84, 85]. Even though the cosine distance is not a proper distance, it has been used in some applications, such as face recognition [89], speech processing [90] and text mining [91]. The angular distance is defined as a normalized angle between two vectors and is calculated from $cos^{-1}(CosSim)$ divided by π, so that the boundary values of the angular distance range from 0 to 1. This means that any two vectors are similar when $AngDis$ approaches 1 and they are dissimilar when $AngDis$ approaches 0. *The properties of the angular distance now do obey the axioms of the proper distance metric, including the triangle inequality* [92].

For given embedding vectors $\boldsymbol{x}_i^{(m)} \cdot \boldsymbol{x}_j^{(m)}$ with an embedding dimension m, the cosine similarity, $CosSim_{i,j}^{(m)}$, cosine distance, $CosDis_{i,j}^{(m)}$, actual angle, $\alpha_{i,j}^{(m)}$, and

angular distance, $AngDis_{i,j}^{(m)}$, of any two embedding vectors $\boldsymbol{x}_i^{(m)}$ and $\boldsymbol{x}_j^{(m)}$where $i \neq j$ are defined as.

$$CosSim_{i,j}^{(m)} = \frac{\boldsymbol{x}_i^{(m)} \cdot \boldsymbol{x}_j^{(m)}}{|\boldsymbol{x}_i^{(m)}||\boldsymbol{x}_j^{(m)}|} \tag{3.4}$$

$$CosDis_{i,j}^{(m)} = 1 - CosSim_{i,j}^{(m)} \tag{3.5}$$

$$\alpha_{i,j}^{(m)} = cos^{-1}(CosSim_{i,j}^{(m)}) \tag{3.6}$$

$$AngDis_{i,j}^{(m)} = \frac{\alpha_{i,j}^{(m)}}{\pi}. \tag{3.7}$$

$$PearCorr_{i,j}^{(m)} = \frac{(\boldsymbol{x}_i^{(m)} - \bar{\boldsymbol{x}}_i^{(m)}) \cdot (\boldsymbol{x}_j^{(m)} - \bar{\boldsymbol{x}}_j^{(m)})}{|\boldsymbol{x}_i^{(m)} - \bar{\boldsymbol{x}}_i^{(m)}||\boldsymbol{x}_j^{(m)} - \bar{\boldsymbol{x}}_j^{(m)}|} \tag{3.8}$$

The geometric interpretation of $AngDis$ and $ChevDis$ in the Euclidean space is illustrated in Figure 3.2, and the geometric interpretation of similar patterns obtained using the Chebyshev and angular distance is illustrated in Figure 3.3.

Despite its obvious amplitude independence, the angular distance is sensitive to any offsets in a time series, including baseline wander generally presenting in real world signals. To eliminate the influence of offsets, the centered cosine similarity version (so-called Pearson correlation) as given by equation (3.8) [93, 94]. The method effectively reduces the influence of the offset by centering the input vectors using their own vector means. Besides, such methods are usually applied to high dimensional vectors which are enough to represent their intrinsic distributions, so their vector means are a good proxy to the global means of the population. However, in practice the reconstructed embedding vectors are of low dimensions, e.g. $m = 2$ or $m = 3$ [34], so that centering such embedding vectors by their local means would compromise the accuracy of their global correlation estimate and could lead to bias when examining similar patterns. To resolve this issue, we propose a simple (optional) pre-processing to remove such offset by using a zero-median method [95], while preserving its amplitude range (unnormalised amplitude). We opt for the zero-median rather than the

zero-mean approach because of its robustness to outliers and spikes, erratic amplitudes to which the zero-mean approach is sensitive. With such pre-processing, the angular distance is made robust to baseline wander.

3.3.3 Cosine Similarity Entropy and Multiscale Cosine Similarity Entropy

The robust entropy algorithm proposed in this study is referred to as the "Cosine Similarity Entropy" (CSE), whereby for consistent entropy estimation within a general framework of Algorithm 3.1, the Chebyshev distance is replaced with the angular distance and the Shannon entropy is employed instead of the standard conditional probability. The Shannon entropy is mathematically described as

$$H(x) = -\sum_{i=1}^{n} p(x_i) \log_b p(x_i), \tag{3.9}$$

where $p(x_i)$ is the probability mass function of random variables $x_i = \{x_1, x_{2,\ldots,}x_N\}$.

For a case of 1-bit data length ($n = 2$) with a given logarithm base $b = 2$, Shannon entropy can be written as

$$H(x) = -(p(x_1) \log_2 p(x_1) + p(x_2) \log_2 p(x_2) \tag{3.10}$$

where $p(x_1)$ is the probability mass function of the random variables $x_1 = 0$ and $p(x_2)$ is the probability mass function of the random variables $x_2 = 1$.

Recall that $p(x_1) + p(x_2) = 1$, so the equation (3.10) can be re-written as

$$H(x) = -[p(x_1) \log_2 p(x_1) + p(1 - x_1) \log_2 p(1 - x_1)]. \tag{3.11}$$

Notice that unlike for the SE, the undefined entropy values only occur when

$p(x_i) = 0$, meaning that none of the similar patterns is found for a given tolerance level (which is unlikely to happen). When the 1-bit data length has a uniformly distributed probability, $p(x_1) = p(x_2) = 0.5$, the unique maximum entropy calculated from equation (3.11) is 1, thus $H(x)$ ranges from 0 to 1.

In the proposed CSE algorithm, the steps in the SE approach, given in Algorithm 3.1, are replicated with three modifications: i) in the first step of the SE, we provide optional pre-processing for removing the offset in a time series, ii) in the third step of the SE, angular distance is used instead of the Chebyshev distance, and iii) in the last step of the SE, we estimate the entropy based on equation (3.11), by substituting the global probability of occurrences of similar patterns $B^{(m)}(r_{cse})$ and its complementary probability $(1 - B^{(m)}(r_{cse}))$ for the terms $p(x_1)$ and $p(x_2)$. The steps of the CSE approach are summarized in Algorithm 3.3.

For the Multiscale Cosine Similarity Entropy (MCSE) algorithm, only the coarse graining process is required prior to proceeding with other steps in the CSE. For a given scale factor ϵ, the coarse-grained scale produced from equation (3.1), is substituted for $\{\boldsymbol{x}_i\}_{i=1}^{N}$ as an input series to the CSE algorithm, and the estimation of the multiscale cosine similarity entropy is given by

$$MCSE(m, \tau, r_{cse}, N, \epsilon) = -[B_{(\epsilon)}^{(m)}(r_{cse}) \log_2 B_{(\epsilon)}^{(m)}(r_{cse}) + (1 - B_{(\epsilon)}^{(m)}(r_{cse})) \log_2 (1 - B_{(\epsilon)}^{(m)}(r_{cse})] \quad (3.12)$$

where $B_{(\epsilon)}^{(m)}(r_{cse})$ and $B_{(\epsilon)}^{(m+1)}(r_{cse})$ are respectively the global probabilities of occurrences of similar patterns for a given m and $(m + 1)$.

Note that in the SE and FE algorithms, $ChebDis$ can be obtained for any two embedding vectors with a minimal $m = 1$, since the distance is based on the operation on individual element of two vectors, while in the CSE, $AngDis$ can be obtained for any two embedding vectors with a minimal $m = 2$, since vectors with a single dimension are always aligned to their single basis vector (a trivial angular

Algorithm 3.3. Cosine Similarity Entropy

For a time series $\{x_i\}_{i=1}^{N}$ with given embedding dimension (m), tolerance (r_{cse}) and time lag (τ):

1. (Optional pre-processing) Remove the offset and generate a zero median series $\{\boldsymbol{s}_i\}_{i=1}^{N}$ as
$$s = x_i - median(\{\boldsymbol{x}_i\}_{i=1}^{N}) \, , i = 1, ..., N - m + 1$$
2. Construct the embedding vectors, $\boldsymbol{x}_i^{(m)}$ from $\{\boldsymbol{x}_i\}_{i=1}^{N}$ (or from $\{\boldsymbol{s}_i\}_{i=1}^{N}$) using
$\boldsymbol{x}_i^{(m)} = [x_i, x_{i+\tau}, ..., x_{(i+(m-1)\tau)}] - \frac{1}{i+(m-1)\tau} \sum_i^{i+(m-1)} x_i \; i = 1, ..., N - m + 1$
3. Compute angular distance for all pairwise embedding vectors as
$$AngDis_{i,j}^{(m)} = \frac{1}{\pi} cos^{-1}\left(\frac{\boldsymbol{x}_i^{(m)} \cdot \boldsymbol{x}_j^{(m)}}{|\boldsymbol{x}_i^{(m)}||\boldsymbol{x}_j^{(m)}|}\right), \; i \neq j$$
4. Obtain the number of similar patterns $P_i^{(m)}(r_{cse})$ when a criterion
$AngDis_{i,j}^{(m)} \leq r_{cse}$ is fulfilled
5. Compute the local probability of occurrences of similar patterns, $B_i^{(m)}(r_{cse})$, as
$$B_i^{(m)}(r_{cse}) = \frac{1}{N-m} P_i^{(m)}(r_{cse})$$
6. Compute the global probability of occurrences of similar patterns, $B^{(m)}(r_{cse})$, from
$$B^{(m)}(r_{cse}) = \frac{1}{N-m} \sum_{i=1}^{N-m} B_i^{(m)}(r_{cse})$$
7. Cosine similarity entropy is now estimated from
$$CSE(m, \tau, r_{cse,N}) = \\ -[B^{(m)}(r_{cse}) \log_2 B^{(m)}(r_{cse}) + (1 - B^{(m)}(r_{cse})) \log_2 (1 - B^{(m)}(r_{cse})].$$

distance), so that $AngDis$ is valid only when applied to vectors with $m \geq 2$ (see equations (3.4)-(3.7) and Figure 3.2); this is practically perfectly valid.

3.4 Selection of Parameters

Selection and robustness of the parameter values of the proposed CSE approach is next demonstrated over several benchmark scenarios.

3.4.1 Selection of the Tolerance (r_{cse}) for CSE

In the SE and the FE approaches, tolerance is defined as a product of a given ratio value (r) and the standard deviation (sd) of a considered time series, that is, $r_{se} = r_{fe} = r \times \text{sd}$. The recommended tolerance level, r_{se}, for the SE, is between 0.1 and 0.25 [32, 79]. The recommended tolerance level, r_{fe} , for the FE is between 0.1 and 0.3 [14]. In our proposed CSE and MCSE algorithms, we examined how entropy changes as a function of r_{cse} on four synthesized signals:

1. White Gaussian Noise (WGN),
2. $1/f$ noise,
3. The first order autoregressive model (AR(1)) generated from $x(t) = 0.9x(t-1) + \varepsilon(t)$ and
4. The second order autoregressive model (AR(2)) generated from $x(t) = 0.85x(t-1) + 0.1x(t-2) + \varepsilon(t)$, where $\varepsilon(t) \sim \mathcal{N}(0, 1)$.

We generated 20 independent realizations with 10,000 samples for each synthetic signal with the recommended $m = 2$ [34], $\tau = 1$ [96], and varied r_{cse} from 0.01 to 0.99 with an incremental step of 0.02 (as the boundary values of the angular distance ranges from 0 to 1). Since Shannon entropy is employed in the proposed CSE algorithm, it is anticipated that the outcomes of the CSE versus r_{cse} are analogous to the properties of Shannon entropy versus probability of a selected event, $Pr(X = 1)$, when using 1-bit data, as shown in Figure 3.4(a). Figure 3.4(b) illustrates the results of the CSE plotted as mean entropies with their sd against r_{cse}. Observe a rise of mean entropies in all the four CSE curves from low to high entropy with an increase in r_{cse} from 0.01 to 0.49, and a decrease in mean entropies in all the four curves with an increase of r_{cse} from 0.51 to 0.99. This means that, as anticipated, the characteristics of the CSE resemble the characteristics of the Shannon entropy where the unique maximum entropy

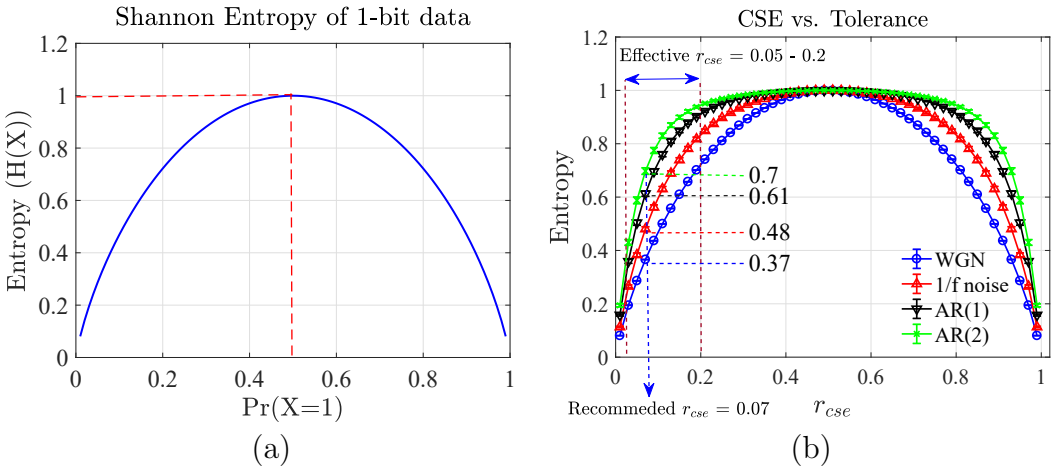

Figure 3.4: **Selection of the tolerance parameter for the CSE algorithm**. (a) Standard Shannon entropy curve as a function of probability of a selected event ($Pr(X = 1)$) when using 1-bit data. (b) Four CSE curves for WGN, $1/f$ noise, AR(1) and AR(2), when varying r_{cse} from 0.01 to 0.99.

occurs at $r_{cse} = 0.5$. We can thus approximately define an optimal range of the r_{cse} for which the mean entropies of the four synthetic signals are (visually and statistically) discriminated to between[2] 0.05 and 0.2. For a comparison between the mean entropies among the four synthetic signals, we empirically selected $r_{cse} = 0.07$, for which the corresponding mean entropies of the WGN, $1/f$ noise, AR(1) and AR(2) were respectively 0.37, 0.48, 0.61 and 0.7.

3.4.2 Effect of Embedding Dimension and Sample Size

The sample size, N, and embedding dimension, m, are important parameters which affect the outcomes of the SE and FE approaches[3]. In practical applications, it is acceptable to select a small embedding dimension such as $m = 2$ [34, 97, 14] for both approaches, while the rule of thumb for appropriate N is as low as $10^m - 30^m$ for the SE [32, 79], but not for the FE for which N can be selected to be down to

[2]The region of r_{cse} between 0.51 and 0.99 can also be used since the entropy values of this region are comparable to the region of r_{cse} between 0.01 to 0.49, but we considered the later due to the fact that the smaller the tolerance the greater the similarity.

[3]We do not consider varying the time lag, τ, parameter because this is analogous to a number of samples used in a downsampling method. Hence, we fix $\tau = 1$ [96] for the structural preservation of the original data.

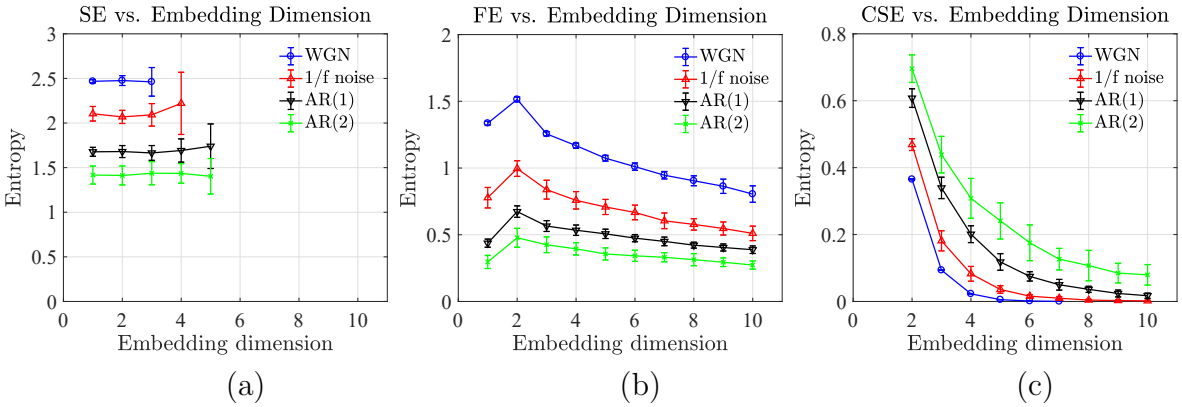

Figure 3.5: **Comparison of the entropy curves over a varying embedding dimension using the SE, FE and CSE approaches.** The 30 independent realizations with 1,000 samples were generated for each of the four synthetic signals; WGN, $1/f$ noise, AR(1) and AR(2). The mean entropies with their standard deviations are plotted against the embedding dimension. (a) Results of the SE, (b) Results of the FE, and (c) Results of the CSE.

50 samples [14]. We next tested the performances of the three entropy approaches (SE, FE and CSE) as the functions of: 1) embedding dimension and 2) sample size. In the first test, we generated 30 realizations for each of the four synthetic signals; WGN, $1/f$ noise, AR(1) and AR(2), as mentioned in Section 3.4.1, with the selection of $N = 1,000$, $\tau = 1$, $r_{se} = r_{fe} = 0.15$ [79], $r_{cse} = 0.07$ and $\eta = 2$ [14] (an order of the Gaussian membership function used in the FE [14]), while varying m from 1 to 10 (for the CSE, m was varied from 2 to 10 as mentioned in Section 3.3). In the second test, we generated 30 independent realizations for each of the four synthetic signals with the values of $m = 2$, $\tau = 1$, $r_{se} = r_{fe} = 0.15$, $r_{cse} = 0.07$ and $\eta = 2$, while varying N with three different step sizes: i) for the sample sizes from 10 to 1000, the incremental step was 10 samples ($N = 10 : 10 : 1000$), ii) for the sample sizes from 1020 to 2000, the incremental step was 20 samples ($N = 1020 : 20 : 2000$), and iii) for the sample sizes from 2050 to 5000, the incremental step was 50 samples ($N = 2050 : 50 : 5000$).

Figure 3.5 shows the results of mean entropies with their sd against embedding dimension m. Figure 3.5(a) depicts the results of the SE in which the mean entropies behaved consistently over different ranges of m for each synthetic signal:

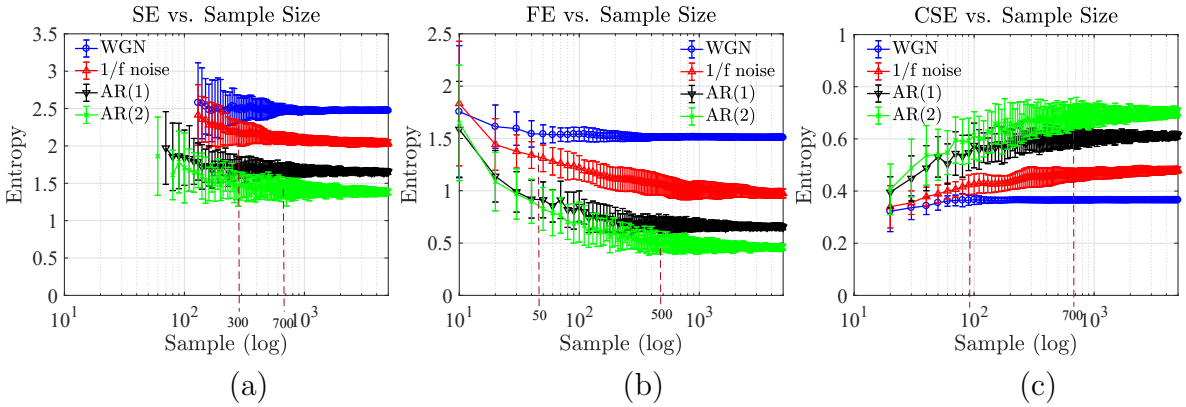

Figure 3.6: **Comparison of the entropy curves over varying sample sizes using the SE, FE and CSE approaches**. The 30 independent realizations with a range of sample sizes from 10 to 5,000 samples were generated for each of the four synthetic signals; WGN, $1/f$ noise, AR(1) and AR(2). The mean entropies with their standard deviations are plotted against data length N. (a) Results of the SE. (b) Results of the FE. (c) Results of the CSE. Observe the excellent stability of CSE estimates, even for samples sizes as small as 50 samples.

i) WGN: $m = [1, 2, 3]$, ii) $1/f$ noise: $m = [1, 2, 3, 4]$, iii) AR(1) and AR(2): $m = [1, 2, ..., 5]$. *However, for any m outside the ranges mentioned, the SE resulted in undefined entropy.* Figure 3.5(b) illustrates the results of the FE in which the mean entropies of all synthetic signals showed a slow decline with an increase in m, and the mean entropies peaked at $m = 2$. Figure 3.5(c) shows the results of the CSE in which the mean entropies decreased with an increase in m, and when $m \geq 6$, the mean entropies of the WGN and $1/f$ noise approached zero.

Remark 1. From Figure 3.5 the SE gives valid entropy values only for $m = [1, 2, 3]$.

Figure 3.6 shows the results of the second test (varied N) plotted as mean entropies with their sd against N. Figure 3.6(a) depicts the results of the SE approach in which the entropy values of the WGN and $1/f$ noise were valid for $N \geq 130$, for the AR(1), entropy was valid for $N \geq 70$, and for the AR(2), entropy was valid for $N \geq 60$. By visually selecting any N at which the sd of the two mean entropies were non-overlapped, the separation of mean entropies between the WGN and the $1/f$ noise was significant when $N \geq 300$, and for between the AR(1) and the AR(2) the separation was achieved when $N \geq 700$. Figure 3.6(b) illustrates the results of

the FE in which the entropy of all synthetic signals was valid over the whole range of the sample sizes. The separation of mean entropies between the WGN and the $1/f$ noise was discernible when $N \geq 50$, and between the AR(1) and the AR(2) the separation of mean entropies was pronounced when $N \geq 500$. Figure 3.6(c) shows the results of the CSE approach in which the entropy of all synthetic signals was valid even when the numbers of samples was as low as 20. The separation of mean entropies between the WGN and the $1/f$ noise was observed when $N \geq 100$, while between the AR(1) and AR(2), separation of mean entropies was pronounced when $N \geq 700$.

Remark 2. From Figure 3.6, for the separation of mean entropies between WGN and $1/f$ noise, the CSE requires a smaller sample size ($N = 100$) than that of the SE ($N = 300$).

3.5 A Comparison of Complexity Profiles using MSE, MFE and MCSE

After having established the basic properties of the proposed CSE approach, we now evaluate the usefulness of its multiscale version, the multiscale CSE (MCSE), for the quantification of the structural complexity over the coarse-grained scales (see equation (3.12)).

3.5.1 Complexity Profiles of Synthetic Noises

To examine the behaviors of the multiscale versions - MSE, MFE and MCSE - over the coarse-grained scales (complexity profiles [43]), we generated 20 independent realizations of 10,000 samples for each of the four synthetic signals; WGN, $1/f$ noise, AR(1) and AR(2), as described in Section 3.4.1. For the three multiscale entropy approaches, we selected $m = 2$ [52], $\tau = 1$, $r_{se} = r_{fe} = 0.15$, $r_{cse} = 0.07$,

$\eta = 2$ and the scale factor, ϵ, from 1 to 20. Figure 3.7 illustrates the results of the three approaches plotted as mean entropies with their sd against the scale factors. Figure 3.7(a) depicts the results of the MSE from which distinctive profiles of the entropy curves can be observed. At $\epsilon = 1$, the order of the mean entropies from high to low corresponded to the WGN, $1/f$ noise, AR(1) and AR(2), while at a large scale, $\epsilon = 20$, both the AR(1) and AR(2) yielded the highest mean entropies, and the lower mean entropies were the $1/f$ noise followed by the WGN. The distinctive behavior for each synthetic signal can be characterized as follows: i) for the WGN, the entropy curve decreased as the scale increased; i.e. at ϵ=1, the mean entropy was 2.5, and at $\epsilon = 20$, the mean entropy fell to 1.0; ii) for the $1/f$ noise, the entropy curve was relatively consistent over all scale factors (mean entropies varied between 1.87 and 2.04); iii) for the AR(1) and AR(2), the entropy curves gradually ascended as the scale increased; i.e. at $1 \leq \epsilon \leq 17$, the entropy curve of the AR(1) was above the entropy curve of the AR(2) while at $\epsilon \geq 18$, the entropy curves of both the AR(1) and AR(2) converged and then overlapped at the mean entropy values of 2.12. Figure 3.7(b) shows the results of the MFE approach in which all the entropy curves were similar to the corresponding entropy curves of the MSE. The only difference was that the MFE produced lower mean entropies than the MSE.

Figure 3.7(c) illustrates the results of the MCSE from which distinctive complexity profiles can be observed. At $\epsilon = 1$, the order of high to low mean entropies was the AR(2), AR(1), $1/f$ noise and WGN, while at $\epsilon = 20$, the order of high to low mean entropies was the $1/f$ noise, AR(2), AR(1) and WGN, *that is the correct order of structural complexity*. This can be explained as follows: i) for the WGN, the mean entropy value of 0.37 was consistent over the whole range of the scale factors; ii) for the $1/f$ noise, the entropy curve slowly decreased or was almost consistent with small variation of mean entropies (between 0.45 and 0.49); in addition, as desired the mean entropies of the $1/f$ noise were higher than those of the WGN over all the scale factors; iii) for the AR(1) and AR(2), the entropy curves gradually decayed

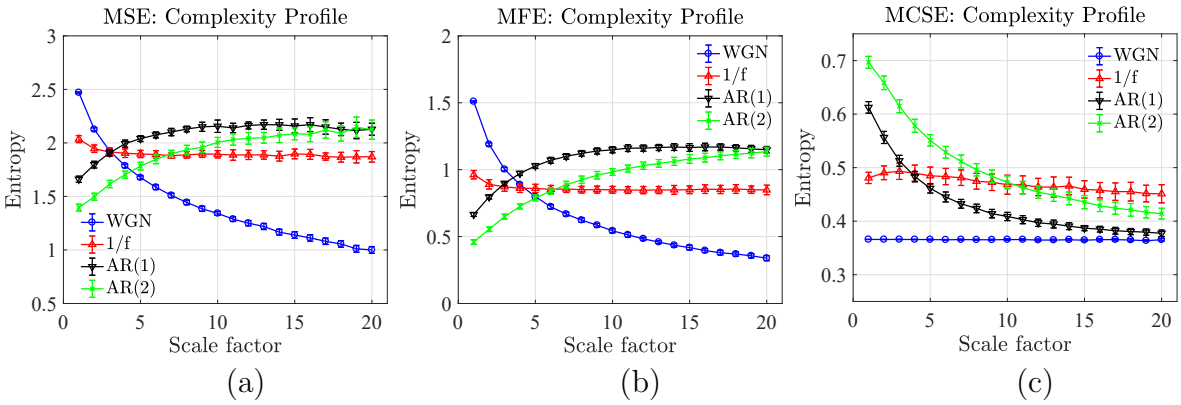

Figure 3.7: **Comparison of the complexity profiles of the four synthetic signals, WGN, $1/f$ noise, AR(1) and AR(2), using the MSE, MFE and MCSE approaches**. The 20 independent realizations with 10,000 samples were generated for each of the four synthetic signals. The mean entropies with their standard deviations are plotted against the coarse-grained scales. (a) Results of the MSE. (b) Results of the MFE. (c) Results of the MCSE. Observe the very consistent and correct behaviors of MCSE in plot (c), especially for large scales, unlike the MSE and MFE in plots (a) and (b).

as the scale factor increased; as desired the entropy curves of the AR(1) was lower than those of the AR(2) for the whole range of the scale factors; i.e. at $\epsilon = 1$, mean entropies of the AR(1) and AR(2) had the values of 0.61 and 0.7, while at $\epsilon = 20$, the mean entropies the AR(1) and the AR(2) were 0.38 and 0.41.

Remark 3. From Figure 3.7, at a large scale factor, the MCSE gives a well defined separation of mean entropies among all the synthetic signals, WGN, $1/f$ noise, AR(1) and AR(2), while the MSE and MFE only yield a good separation of mean entropies between the WGN and the $1/f$ noise. In addition, unlike MSE and MFE, for the proposed MCSE, the complexity of the $1/f$ noise was higher than that of the WGN for the whole range of the scale factors.

3.5.2 Complexity Profiles of Autoregressive Models

We next examined the complexity profiles of an ensemble of autoregressive processes (AR) over the coarse-grained scales, through the MSE, MFE and

MCSE. To this end, we generated two groups of AR processes including i) AR(1)s with nine different correlation coefficients (α_1, where $\alpha_1 = [0.1, 0.2, ..., 0.8, 0.9]$) and ii) AR($p$) processes of nine orders (p, where $p = [1, 2, ..., 8, 9]$) with the pre-defined correlation coefficients (see more details in Appendix A). We generated 20 independent realizations of 10,000 samples for the WGN which was also used as the driving noise for all nine AR(1)s and for all nine orders of the AR(p) processes. For the three multiscale entropy approaches, we selected $m = 2$, $\tau = 1$, $r_{se} = r_{fe} = 0.15$, $r_{cse} = 0.07$, $\eta = 2$ and ϵ from 1 to 20.

Remark 4: Our hypothesis is that a consistent complexity estimator should give the same quantification of complexity for all nine AR(1) processes, independent of the correlation function as all these processes have only one degree of freedom. Similarly, the complexity of the AR(p) processes, $p = [1, 2, ..., 9]$, should increase with the order p.

Figure 3.8 illustrates the results of the three approaches applied to the first group of the synthetic AR processes. The results are plotted as mean entropies with their sd against the scale factors. Figure 3.8(a) depicts the results of the MSE; at $\epsilon = 1$, the WGN yielded the highest mean entropy, and the lower mean entropies were ranked in a descending order corresponding to the low to high correlation coefficients of the AR(1) (i.e. $\alpha_1 = [0.1, 0.2, ..., 0.8, 0.9]$). At $\epsilon = 20$, the mean entropies were ranked in a descending order corresponding to the high to low correlation coefficients of the AR(1) (i.e. $\alpha_1 = [0.9, 0.8, ..., 0.2, 0.1]$), while the lowest mean entropy was that of the WGN. Figure 3.8(b) shows the results of the MFE where all the entropy curves were similar to the corresponding entropy curves of the MSE. The only difference was that the MFE produced lower mean entropies than those of the MSE. Figure 3.8(c) illustrates the results of the MCSE from which distinctive profiles of the entropy curves can be observed. At $\epsilon = 1$, the mean entropies were ranked in a descending order corresponding to the high to low correlation coefficients of the AR(1) (i.e. $\alpha_1 = [0.9, 0.8, ..., 0.2, 0.1]$), while the lowest mean entropy belonged to the WGN, which was constantly 0.37 for the whole range of the scale factors.

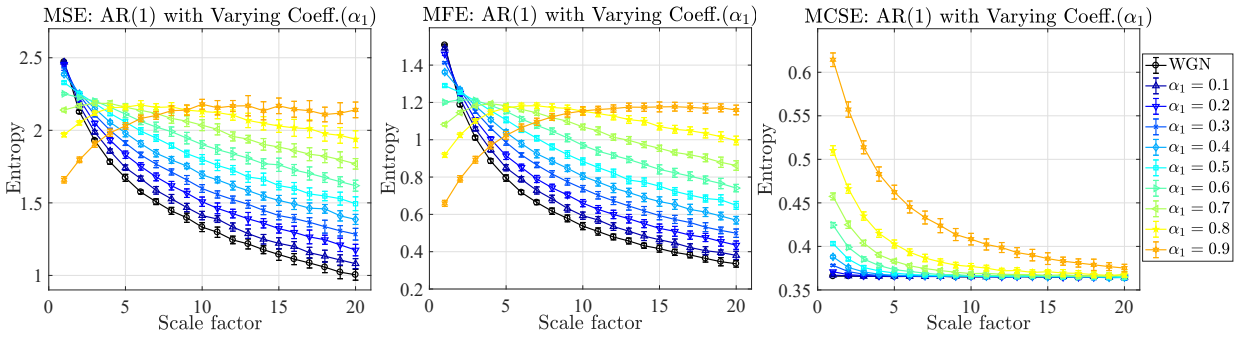

Figure 3.8: **Comparison of the complexity profiles of AR(1) processes with a varying α_1, using the MSE, MFE and MCSE approaches**. The independent 20 realizations with 10,000 samples of WGN were generated as a driving noise for each of the nine AR(1) with a varying correlation coefficient α_1 ($\alpha_1 = [0.1, 0.2, ..., 0.8, 0.9]$, see more details in Appendix A). The mean entropies with their standard deviations are plotted against the coarse-grained scales. (a) Results of the MSE, (b) Results of the MFE and (c) Results of the MCSE.

At a large scale, $\epsilon = 20$, the mean entropies were ranked in a descending order corresponding to the decreasing correlation coefficients of the AR(1). Notice that all the entropy curves asymptotically converged correctly, including that all the AR(1) processes have the same complexity.

Remark 5: From Figure 3.8, for the ensemble AR(1) processes of a varying correlation coefficients, the MCSE, unlike the other methods considered, provided robust, accurate and physically meaningful quantification of complexity of the system. In other words only the MCSE was able to assess the correct complexity of the underlying signal-generation system, the AR(1).

Figure 3.9 illustrates the results of the three approaches applied to the second group of synthetic AR processes. The results are plotted as mean entropies with their sd against the scale factors. Figure 3.9(a) depicts the results of the MSE; at $\epsilon = 1$, WGN yielded the highest mean entropy, and the lower the mean entropies were ranked in a descending order corresponding to the low to high orders of the AR(p) (i.e. $p = [1, 2, ..., 9]$), while at $\epsilon = 20$, the mean entropies of the AR(p)s were ranked in a descending order corresponding to the order AR(p)s as AR(3), AR(4),

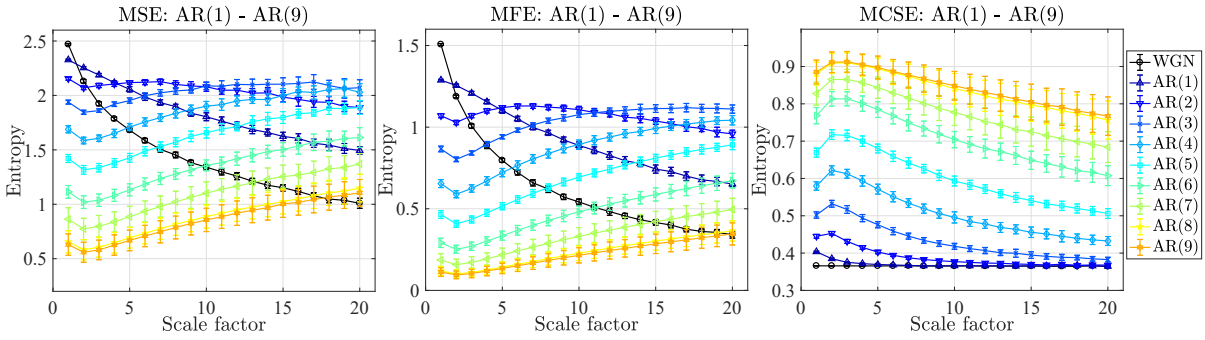

(a) (b) (c)

Figure 3.9: **Comparison of the complexity profiles of AR(p) processes, where p is the AR order ranging from 1 to 9, using the MSE, MFE and MCSE approaches**. The independent 20 realizations with 10,000 samples of WGN were generated as a driving noise for each of the nine AR(p) processes with pre-defined correlation coefficients (for details see Appendix A). The mean entropies with their standard deviations are plotted against the coarse-grained scales. (a) Results of the MSE, (b) Results of the MFE and (c) Results of the MCSE.

both the AR(2) and AR(5) (overlapped), AR(6), AR(1), AR(7), AR(8), AR(9), the lowest mean entropy belonged to WGN. Figure 3.9(b) shows the results of the MFE in which all the entropy curves were similar to the entropy curves of the MSE. The two differences were that: i) the MFE produced lower mean entropies than those of the MSE, and ii) at $\epsilon = 20$, the mean entropies of the AR(2) were higher than that of the AR(5) (not overlapped as the result of the MSE). Figure 3.9(c) illustrates the results of the MCSE, with the correct distinctive profiles of the entropy curves observed. At $\epsilon = 1$, the mean entropies were ranked in a descending order corresponding to the high to low orders of the AR(p) processes (i.e. $p = [9, 8, ..., 1]$), and the lowest mean entropy was that of the WGN (no structure), with a constant value of 0.37 over the whole range of the scale factors. At a large scale, $\epsilon = 20$, the mean entropies of the AR(p)s were ranked in a descending order corresponding to the order of the AR(p)s as at $\epsilon = 1$. Notice that all the entropy curves exhibited a slight decrease in their mean entropies with an increase in the scale factor.

Remark 6: From Figure 3.9, only the proposed MCSE was able to distinguish

between the structural complexities of the signal-generation system which ranged from one degree of freedom (AR(1)) to nine degrees of freedom (AR(9)).

3.5.3 Complexity Profiles of Heart Rate Variability

We next examined the entropy behavior of heart rate variability (HRV) over the coarse-grained scales through the MSE, MFE and MCSE. Three cardiovascular pathologies of one-hour RR intervals: i) Normal Sinus Rhythm (NSR, 18 subjects); ii) Congestive Heart Failure (CHF, 20 subjects); and iii) Atrial Fibrillation (AF, 20 subjects), were obtained from the Physionet database (for more details see Appendix B). We estimated the HRV time series of the three cardiac conditions by re-sampling the obtained RR intervals at the frequency of 8 Hz using the shape-preserving piecewise cubic interpolation [98]. The HRVs were segmented into trials of 10-min length (5-min length is recommended by [98] but this yields a sample size of 2,400 which is effectively enough only for computing entropy within the scale factors of less than 10, so we extended the segment length of the HRV to 10-min for computing entropy with the scale factor up to 20). For the three multiscale approaches, we selected $m = 2$, $\tau = 1$, $r_{se} = r_{fe} = 0.15$, $r_{cse} = 0.07$, $\eta = 2$ and varied ϵ from 1 to 20.

Figure 3.10 illustrates the results of the three approaches plotted as mean entropies with their standard errors (se) against the scale factors. Figure 3.10(a) depicts the results of the MSE; at $\epsilon = 1$, AF and NSR yielded the highest mean entropies (the mean entropy of the AF (0.36) was slightly higher than the mean entropy of the NSR (0.31)), and the CHF yielded the lowest mean entropy (mean entropy was 0.2). At $\epsilon = 20$, the order of the mean entropies from high to low was the NSR, AF and CHF. Figure 3.10(b) shows the results of the MFE where all the entropy curves were similar to the entropy curves of the MSE. The only two differences were: i) the MFE produced lower mean entropies than the MSE, ii) at $\epsilon = 1$, the highest mean entropy was to the AF (0.17), followed by the mean entropies of

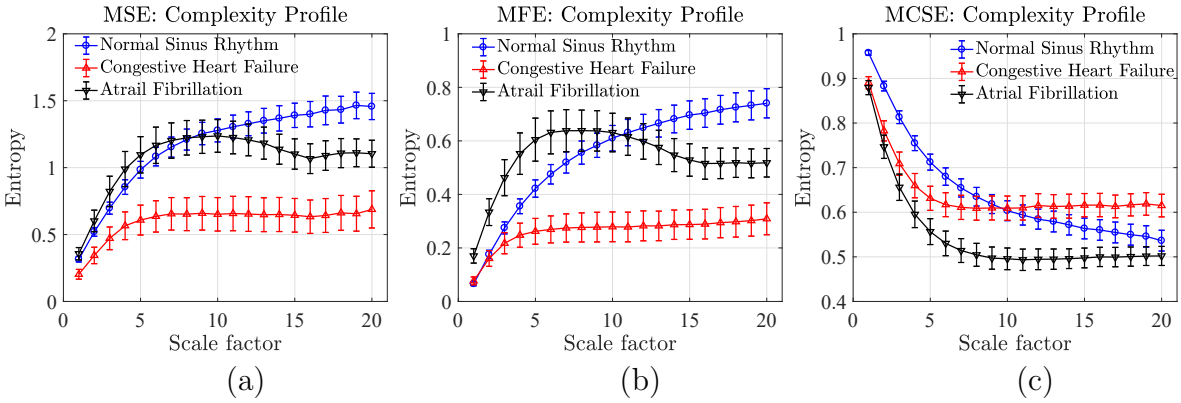

Figure 3.10: **Comparison of the complexity profiles of heart rate variability using the MSE, MFE and MCSE approaches**. Three conditions of heart rate variability were considered: i) Normal sinus rhythm, ii) Congestive heart failure and iii) Atrial fibrillation were which were obtained from the Physionet database (for more details see Appendix B). Mean entropies and their standard errors are plotted against the coarse-grained scales. (a) Results of the MSE, (b) Results of the MFE and (c) Results of the MCSE.

both the CHF and NSR (overlapped at 0.08). Figure 3.10(c) illustrates the results of the MCSE; at $\epsilon = 1$, the order of the mean entropies from high to low was the NSR, CHF and AF (the mean entropy of the CHF (0.89) was slightly higher than the mean entropy of the AF (0.88)), while at the $\epsilon = 20$, the order of the mean entropies from high to low was the CHF, NSR and AF.

3.6 Discussion and Conclusions

We have introduced the Cosine Similarity Entropy (CSE) and the Multiscale Cosine Similarity Entropy (MCSE) algorithms to robustly quantify the structural complexity of real-world data. This has been achieved based on the similarity of embedding vectors, evaluated through the angular distance, the Shannon entropy and the coarse-grained scale. We have examined the characteristic of the CSE by varying the tolerance level and have found the optimal range for the tolerance to be between 0.05-0.2. The effects the parameters including the embedding dimension and the sample size on the three approaches, the SE, FE and CSE, have also been evaluated over the four synthetic signals, the WGN, $1/f$ noise,

Table 3.1: Recommended parameters ranges for the SE, FE and CSE algorithms.

Parameter/Approach	SE	FE	CSE
Tolerance (r)	0.1-0.25 [79]	0.1-0.3 [14]	0.05-0.2
Embedding dimension (m)	1-3	1-10	2-5
Min. sample size (N) for WGN & $1/f$ noise	300	50	100
Min. sample size (N) for AR(1) & AR(2)	700	500	700

AR(1) and AR(2) processes. The appropriate selection[4] of m and N for the three approaches are summarized in Table 3.1. The advantage of the CSE over the SE is that the CSE requires a small sample size for the separation of mean entropies between WGN and $1/f$ noise (the CSE requires 100 samples while the SE requires 300 samples), but in every case, the FE requires the minimum sample size compared to the sample sizes required in the SE and CSE.

The proposed CSE algorithm has been demonstrated to quantify degrees of self-correlation-based complexity in a time series rather than to quantify degrees of uncertainty-based complexity as in the SE and FE algorithms. We have also determined how the entropy values of the four synthetic signals, WGN, $1/f$ noise, AR(1) and AR(2), behave over the coarse-grained scale, so-called complexity profiles through the corresponding multiscale versions- MSE, MFE and MCSE. The results of the MSE and MFE at the first scale factor have revealed that the degrees of the structural complexity (uncertainty-based) from high to low correspond to the WGN, $1/f$ noise, AR(1) and AR(2), whereas the results of the MCSE sort the degrees of the structural complexity (self-correlation-based) from high to low as AR(2), AR(1), $1/f$ noise and WGN. In terms of self-correlation, as an uncorrelated signal, WGN has no structure, the $1/f$ noise is a long-term correlated signal and hence with maximum structure, and the AR(1) and AR(2) processes exhibit different degrees of short-term correlation, whereby the AR(2) can be more correlated than the AR(1) owing to its higher order (more degree of

[4]The low embedding dimension, $m = 2$ [52], is recommended for the multiscale versions; MSE, MFE and MCSE, due to a decrease in the number of samples with an increase in the scale factor.

freedom or more correlated terms). Therefore, at a small scale factor (short-term), the degrees of the self-correlation-based complexity from high to low correspond to the AR(2), AR(1), $1/f$ noise and WGN, while at large scale factor (long-term), the degrees of the self-correlation-based complexity ordered from high to low correspond to the correct order, $1/f$ noise, AR(2), AR(1), and WGN. We have found that only the results from the MCSE have been able to correctly reveal this short- to long-term structural complexity order and to give physically meaningful estimates. The results of the MCSE have also shown that the mean entropies of WGN have yielded the lowest complexity and were consistent over the whole range of the scale factors, meaning that the WGN has no correlation in the short- or long-term and can thus be used as a "reference complexity" (no structure in an uncorrelated signal).

We have also tested the three approaches over the nine varying correlation coefficients of the AR(1), and nine increasing orders of the AR(p) process. We have hypothesized that the low to high degrees of complexity are in a direct relationship with the small to large values of the correlation coefficients of the AR(1), and the increasing orders of the AR(p) (degrees of freedom), and have found that the results of the three multiscale entropy estimates quantify relationships with these AR processes as follows:

- The results of the MSE and MFE have unveiled that the high to low mean entropies (complexity) were in agreement with the high to low values of the correlation coefficients of the AR(1) only at the large scale factor, while the results of the MCSE correctly indicate the corresponding orders of the mean entropies over all the scale factors, which is rather significant at the small scale factor.

- The results of the MSE and MFE have showed that the mean entropies at the first scale factor from high to low coincide with the small to large orders of the AR(p), while the results of the MCSE disclosed the corresponding

orders of the mean entropies over all the scale factors, illustrating as the robust nature of the proposed algorithms.

This indicates that the MCSE can be used to quantify degrees of complexity based on self-correlation in the short- and long-term, while the MSE and MFE estimates are physically meaningful only when considering entropy at a large scale factor. However, at a large scale factor, the MSE and MFE yielded mixed orders of complexity of the synthetic AR(p), as described in Section 3.5.2, so the interpretation of degrees of self-correlated complexity by using both of the MSE and MFE should be made with caution, as these metrics are not reliable when assessing the number of degrees of freedom of the underlying signal-generation process.

Finally, we have applied the three approaches to the real-world HRVs obtained from the three cardiac pathologies, NSR, CHF and AF (with an unknown order of complexity) and have found that the three approaches resulted in different complexity profiles, which can be summarized as follows:

- The MSE resulted in equal complexity (overlapped mean entropies) for the NSR and the AF, which were higher than the complexity of the CHF at the first scale factor. When increasing the scale factor, the complexity of the three HRVs increased toward the largest scale factor, where the order of degrees of complexity from high to low were the NSR, AF and CHF.

- The MFE resulted in equal complexity (overlapped mean entropies) for both the NSR and CHF, which were higher than the complexity of the AF at the first scale factor. When increasing the scale factor, the complexity of the three HRVs increased toward the largest scale factor, where the degrees of complexity from high to low were the NSR, AF and CHF, analogous to results of the MSE.

- The MCSE gave equal structural complexity for both the CHF and AF

(overlapped mean entropies) which were higher than the complexity of the NRS at the first scale factor. When increasing the scale factor, the complexity of the three HRVs decreased, and at the largest scale factor the degrees of structural complexity from high to low were the CHF, NRS and AF.

Based on the "Complexity Loss Theory"(CLT) [27], the highest degree of complexity is deemed to correspond to the NRS (normal healthy subjects), while the other health conditions are deemed to exhibit lower complexity (pathologies) [15]. However, this hypothesis is based on degrees of irregularity, whereas our proposed MCSE quantifies structural complexity based on degrees of self-correlation, for which the CHF exhibits highest self-correlated complexity (followed by the NRS and AF). Our proposed measures therefore still admits the concept of the CLT, but with a new definition *"pathology or aging exhibits loss in self-uncorrelated complexity"*. **In other words, pathology or aging exhibits an increase in self-correlated complexity**. Additionally, even though the MCSE yields results which are in contrast to the results from the MSE and MFE, we can still see the good separations of mean entropies among the three cardiac conditions in all approaches. Lastly, the proposed algorithms are demonstrated to be able to quantify degrees of structural complexity in the context of self-correlation over small to large temporal scales, yielding physically meaningful interpretations and rigour in the understanding the intrinsic properties of the system such as the number of degrees of freedom.

3.7 Future work

Future work on the CSE and the MCSE will be related to baseline wander of a time series. Within this issue, we can eliminate an offset of a time series by subtracting the median of a time series, but the baseline wander is likely to contain some non-stationary components usually found in real-world signals. This requires more advanced nonlinear techniques to remove such a baseline for

the improvement of the calculation of the angular distance. We will also examine the robustness of the CSE and MCSE to spikes and erratic peaks, and will investigate the performances of the CSE and MCSE over a variety of real-world recordings, such as biomedical data and financial data. In terms of computational cost, the proposed algorithms will be evaluated against the standard algorithms to assess their potential in applications of online complexity measurements. Moreover, multivariate (and multiscale) version of the CSE will be studied and proposed.

Chapter 4

A Novel Framework for Modelling Evolution of Stress for a Case Study: Public Speaking

4.1 Introduction

The analysis of the electrocardiogram (ECG) is a de-facto standard for providing insight into the state of the cardiovascular system. For example, it captures the atrial depolarization (P wave), the depolarization of the right and left ventricles (QRS complex) and the recovery of the ventricles (T wave). While the clinical use of ECG is well understood, much less is known about how to utilise ECG for the analysis of the balance between the sympathetic (SNS) and parasympathetic (PNS) nervous system, and hence mental and physical stress levels in real-life scenarios. The aim of this study is therefore two-fold: i) to deal with the multiple artefacts in wearable scenarios, and ii) to illuminate the usefulness of the proposed signal processing techniques through the study of the evolution of stress levels of two students presenting their work in an academic conference. For rigour, the analysis is cast into a framework of complexity science, whereby the "Complexity Loss Theory" (CLT) establishes that an organism under constraints (illness, aging) exhibits lower structural complexity of physiological responses than a healthy organism [27]. Our hypothesis is that stress, being a psychophysiological impediment, modulates physiological responses so that they lose degrees of freedom, thereby reducing structural complexity. To this end, stress-related HRV are analysed through i) Sample Entropy (SE) [13], ii) Fuzzy Entropy (FE) [14, 40, 41, 42], and iii) a novel entropy measure, Cosine Similarity Entropy (CSE), as they are designed to operate on real-world nonlinear and non-stationary data. We also include conventional frequency-domain measures; low frequency (LF) and high frequency (HF) power of the HRV frequency

spectrum, and their ratio (LF/HF). In the SE and FE methods, while a decrease in entropy means a rise in degrees of regularity which is linked to high levels of stress [62] as corresponded to the CLT, an increase in complexity corresponds to an increase in randomness in the data, suggesting a physically rest (homeostasis) state [99], *in other words a reduction in degrees of irregularity in HRV suggests high stress levels*. Besides, as we found that the CSE approach yield contrast in entropy (complexity) levels compared to the SE and FE (see more details in Chapter 3), a decreased in entropy (complexity) estimated from the CSE means a reduction in degrees of (self) uncorrelation which is linked to high levels of stress, *in other words an increase in self-correlation in HRV suggests high stress levels*. Although not without controversy, the LF band in HRV, 0.04-0.15 Hz, is thought to reflect the activity of the sympathetic nervous system (SNS; high stress) and the baroreflex, while the HF band, 0.15-0.4 Hz, is believed to correspond to the activity of the parasympathetic nervous system (PNS; relaxed state) and respiratory sinus arrhythmia (RSA), naturally occurring heart rate modulations due to breathing [100, 101]. The ratio of the power in the LF and HF reflects the degree of sympathovagal balance [11], with a higher ratio representing dominant sympathetic activity and a lower ratio indicating an increased vagal modulation [102].

In a previous study, we introduced a new algorithm to extract R-peaks from ECG using a combination of matched filtering and Hilbert transform (MF-HT) [57]. The approach is semi-automatic with the user required to select a QRS waveform mother pattern from the recorded ECG. To locate R-peaks in noisy ECG, the user is provided with several R-peak estimates when an abnormal QRS waveform or heart rate is detected. This is achieved through a user-friendly graphical interface facilitating straightforward data processing.

After detecting the R-peaks, the HRV is constructed from the R-R intervals, the temporal difference between two subsequent R-peaks, yielding an unevenly sampled time series. In order to perform spectral estimation, the HRV is

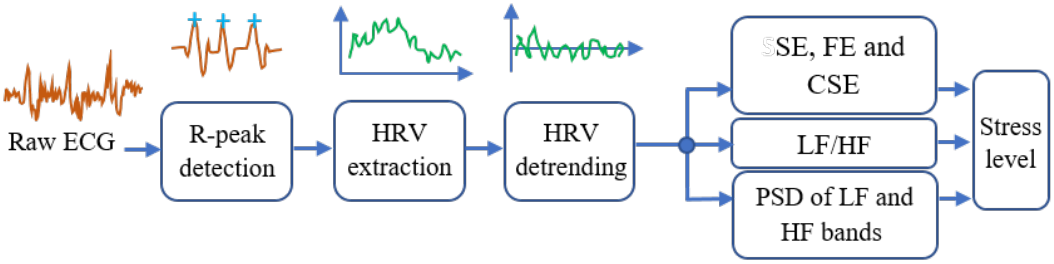

Figure 4.1: **A conceptual block diagram of the proposed framework for stress analysis**. The MF-HT method is employed for R-peaks detection. Nonstationary components of the HRV, estimated from extracted RR-intervals, is removed using the EMD-based HRV detrending method (proposed in this study). Finally, quantification of stress levels is achieved through frequency domain analses (LF/HF, LF and HF power) and entropy-based complexity measures (SE, FE and CSE).

resampled to create a regularly spaced time series using a linear or cubic spline interpolation with a sampling frequency in the range 2-10 Hz [98]. However, oversampling typically leads to an oversampled LF/HF ratio when Fourier transform (FT) is applied [103], and consequently a wrong interpretation. To this end, the Lomb-Scargle periodogram (LSP) [104, 105], a spectral estimation technique for unevenly spaced data, has been applied to the original HRV yielding more reliable results compared to the classical FT [10, 106]. In order to apply the stress-related metrics including the frequency-domain and the nonlinear-domain, it is assumed that the extracted HRV is weakly stationary, in other words, there is no change in the variance and mean in sliding data windows. However, real HRV is typically non-stationary, a signature of changes in psychological and physiological mechanisms [107], and the original HRV is therefore detrended in a pre-processing step. This is achieved based on the empirical mode decomposition (EMD) algorithm [108], whereby the analysis is made physically meaningful by the power spectrum density (PSD) of the HF as the stopping criterion.

This work aims to extract maximum information from HRV related to stress biomarkers by introducing a new signal processing framework (see Figure 4.1) for

mobile cardiovascular scenarios. This has made it possible to: i) detect correct R-peaks in noisy ECG, ii) robustly obtain accurate biomarkers of stress from HRV, and iii) illuminate the utility of the proposed framework in identifying changes in physiological responses due to psychological stress in real-life scenarios. The concept is validated by analysing the stress levels of two presenters during their oral and poster presentations.

4.2 Proposed a Signal Processing Framework

4.2.1 R-peak Detection Algorithm

Our MF-HT algorithm for R-peak detection operates as summarised in Algorithm 4.1 It combines pattern matching with the Hilbert transform and first identifies possible QRS complexes from noisy mobile ECG, followed by the application of the Hilbert transform to identify the R-peak.

4.2.2 HRV Detrending Method

The intrinsic mode function (IMF) resulting from EMD have properties similar to filter banks and are arranged according to their average instantaneous frequency, where IMFs with the highest instantaneous frequencies have the lowest indices. The HF band is thus contained in the IMF indices ranging from the first to the highest one in which the PSD of HF band is still contained. It is therefore possible to use the ratio between the HF power spectrum density of the current IMF and the power spectrum density HF of the previous lower IMF as a threshold parameter to stop the sifting process of the EMD algorithm. In this work, the threshold of the ratio was set to 0.2 (the HF power spectrum density of the current IMF is 5 times less than the HF power spectrum density of the previous IMF) to ensure that the resulting IMF spectrum retains as much as possible of the original HRV spectrum. This is combined with the original stopping condition of the EMD algorithm, the

Algorithm 4.1. Matched Filtering and Hilbert Transform (MF-HT)

Pre-iteration

1. Select a mother QRS waveform from the raw ECG.
2. Locate the first R-peak

For each W_i:

1. Create a window W_i beginning at the previous R-peak and ending at the longest realistic heart beat interval
2. Remove local trend by taking the difference between consecutive sample points
3. Apply a matched filter between the mother QRS and the W_i, resulting in a degree of correlation K_{mf}
4. Apply the Hilbert transform to K_{mf} to identify candidate R-peaks C_j
5. Locate the correct R-peak by selecting the peak C_j with the highest cross-correlation with the mother QRS

End For

Post-iteration

Construct HRV from the time difference between subsequent R-peaks.

standard deviation *sd* of which is 0.2 - 0.3 [108].

Since the original HRV is irregularly sampled, the LSP is well suited to estimate the PSD. The detrending algorithm is described in Algorithm 4.2

Interpolation after detrending is still required because a low number of sample points is prohibitive for the estimation of entropy through the SE, FE and CSE and may lead to unreliable results. A shape-preserving piecewise cubic interpolation was therefore applied to the detrended data. The 4 Hz sampling frequency is selected for interpolation based on the reasons outlined in [98, 103].

Algorithm 4.2. EMD-based HRV Detrend

Denote by $x'(t)$ be the input of each iteration.
For each iteration:

1. Locate lower and upper maxima, e_{min} and e_{max} of $x'(t)$
2. Apply cubic spline interpolation to e_{min} and e_{max}
3. Compute the local mean $m(t) = (e_{max} + e_{min})/2$
4. Obtain the local oscillation $d(t) = x'(t) - m(t)$
5. Examine whether sd fulfills the stopping condition, compute PSD_m of $d(t)$ using LSP and go to step 6, else set $x'(t) = d(t)$ and go to step 1
6. Examine the ratio of PSD_m/PSD_{m-1}. If the ratio is less than 0.2, stop the sifting process and go to step 7 – otherwise extract the IMF, $IMF_m = d(t)$, where m is the IMF number, and set $x'(t) := x'(t) - \sum_{i=1}^{m} IMF_i$
7. Compute the detrended HRV by summing all released IMFs, $dt(t) = \sum_{i=1}^{m-1} IMF_i$.

4.2.3 Selection of Parameters

In the SE, FE and CSE, the required parameters for estimating entropy include embedding dimension m, time lag τ and tolerance levels r_{se}, r_{fe} and r_{cse}. The appropriate selection of m and τ relies on the underlying dynamics of time series. Pincus in [32] suggested that using $m = 2$ or $m = 3$ is sufficient for a low-dimensional system such as the human cardiovascular system. Kaffashi *et al.* [96] recommended that using $\tau = 1$ is sufficient to estimate the complexity of a system, while Pincus [30] recommended that r can be taken as 0.1 – 0.2 times the standard deviation, in order to avoid small unpredictable changes in time series. Therefore, in this study, $m = 2$, $\tau = 1$, $r_{se} = r_{fe} = 0.15$ and $r_{cse} = 0.07$ (see more details in Chapter 3) were chosen. For the frequency-domain analysis, Periodogram based spectral estimation is applied to the detrended HRV followed by a calculation of the PSD in the LF and HF bands and the LF/HF ratio.

4.3 Analysis Results

A sliding window based approach was used for computing the SE, FE, CSE, PSD of LF, PSD of HF, and LF/HF ratio, the metrics chosen to quantify the evolution of stress levels. Different window lengths of 5 min [98] were set respectively for the poster and oral presentation, based on the duration of the recordings. A 15-second sliding time segment was chosen to maintain approximately constant statistical variations over time.

In Figure 4.2 and Figure 4.3, the plots from the top to the bottom show the raw and the detrended HRV, SE estimates (in reversed axis plot), FE estimates (in reversed axis plot), CSE estimates, LF/HF ratio and the PSD of LF, and PSD of HF. The whole recording was divided into three sections: i) the pre-presentation period (Section (a)), ii) the presentation period (Section (b)), and iii) the post-presentation (Section (c)). Note that the reversed axes for the SE and FE estimates are for comfortably interpreting stress levels (the lower the entropy estimates the greater the stress levels).

In the interactive poster presentation, the results from the SE, FE, CSE, LF/HF, the PSD of the HF, the PSD of the LF are shown in Figure 4.2 and can be summarised within the three performance periods, Section (a), (b) and (c), as follows.

- The entropy values of the SE and FE (the third and fourth graph from top of Figure 4.2) gradually decreased from Section (a) to (b), i.e. approximately from 1.1 to 0.7 for the SE and from 0.6 to 0.25 for the FE, (a gradually increased in their curves in both the reversed axes plots), this is followed by an increase in entropy values in Section (c), i.e. approximately from 0.7 to 1.1 for the SE and from 0.3 to 0.65 for the FE, (a decrease in entropy curves in the reversed axes plots). This means a reduction in degrees of irregularity from the pre-performance period to the performance period, and an increase

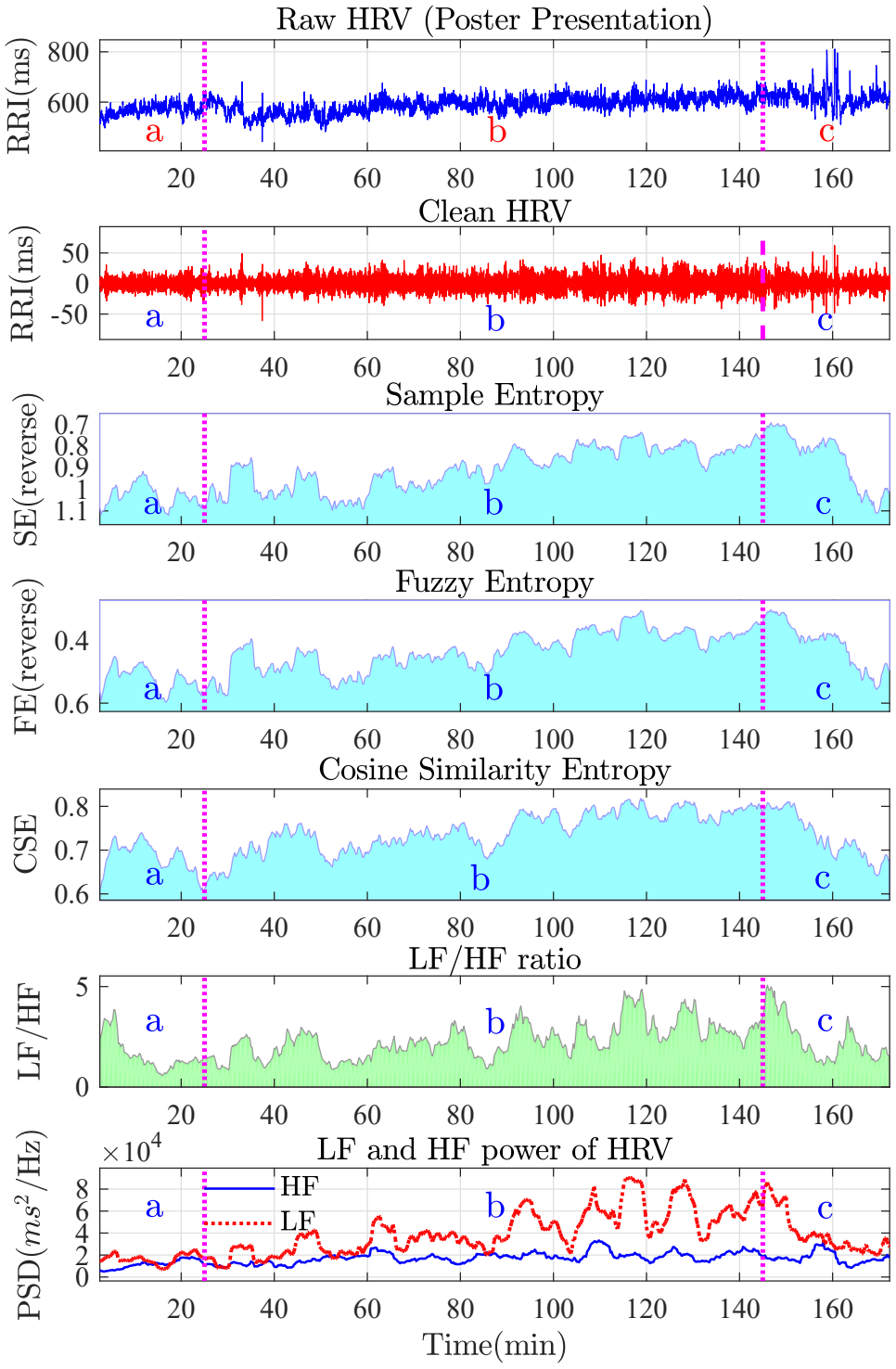

Figure 4.2: **Analysis of evolution of stress in the study case - poster presentation.** Top to bottom: HRV, detrended HRV, SE estimates (in reversed axis), FE estimates (in reverse axis), CSE estimates, LF/HF ratio and the PSD of both the LF and HF bands. The segments a, b and c represent the pre-performance (25 min), performance (120 min) and post-performance (25 min). Notice that an gradually increase in stress levels were revealed through all metrics.

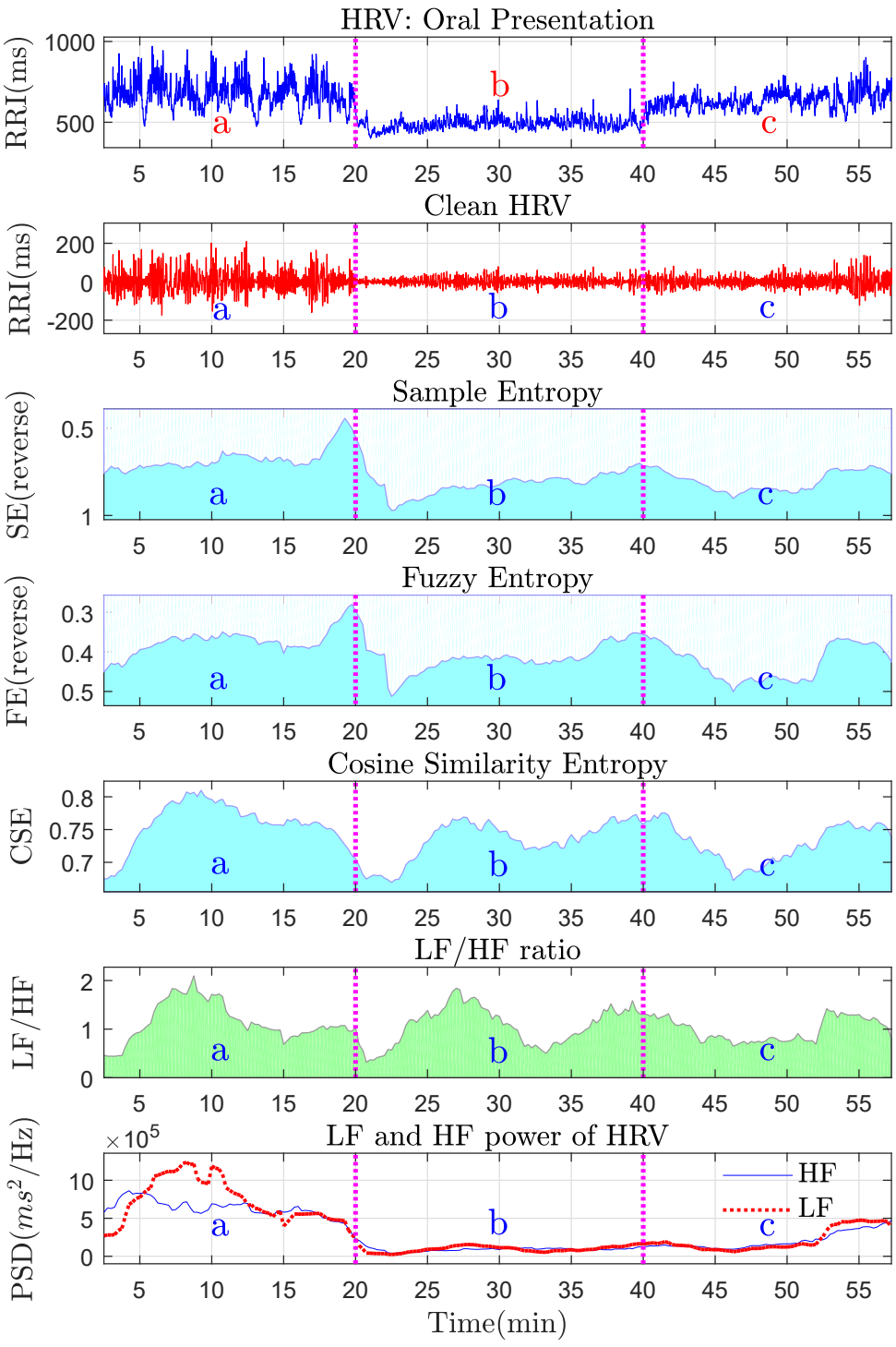

Figure 4.3: **Analysis of evolution of stress in the study case - oral presentation**. Top to bottom: HRV, detrended HRV, SE estimates (in reversed axis plot), FE estimates (in reverse axis plot), CSE estimates, LF/HF ratio and the PSD of LF, and the PSD of HF. The segments a, b and c represent the pre-performance (20 min), performance (20 min) and post-performance (20 min).

in degrees of irregularity in the post-performance period.

- The entropy values of the CSE (the fifth graph from top of Figure 5.2) gradually increased from Section (a) to (b) (from approximately 0.65 to 0.8) with some fluctuations; this was followed by a decrease in entropy values in Section (c) (from approximately 0.8 to 0.65). This means an increase in degrees of self-correlation from the period of the pre-performance to the period of the performance, and a reduction in degrees of self-correlation in the post-performance period.

- The LF/HF ratios and the PSD of the LF and HF (the sixth and seventh graph from top of Figure 5.2) showed an increase in both trends from Section (a) to Section (b) but with frequent fluctuations. This was followed by a decrease in both trends in the Section (c), while the HF exhibited relatively stead trend over all sections.

The entropy-based complexity measures suggested the "low to high stress period" corresponding to from the pre-performance to the performance periods and the "recovery period" corresponding to the post-performance period. The presenter of the poster confirmed an increased level of stress and psychosocial engagement towards the end of the presentation due to an increase in a number of the audience who interacts well beyond the presentation end. In contrast, the HF remained similarly low throughout the scheduled performance, indicating a strong PNS withdrawal and thus a less relaxed state, while the LF/HF ratio exhibited distinctive fluctuations compared to those trends of the entropy estimate results.

In the oral presentation, the results from the SE, FE, CSE, LF/HF, the PSD of the HF, the PSD of the LF are shown in Figure 4.3 and can be summarised within the three performance periods, section (a), (b) and (c), as follows.

- In section (a), the entropy curves of the SE and FE (the third and fourth

graph from top of Figure 4.3) exhibited steadily low levels (0.75 for the SE and 0.4 for the FE), but at the end of this section the entropy values suddenly declined (from 0.75 to 0.5 for the SE and from 0.4 to 0.3 for the FE). Continuously, at the beginning of section (b), both the entropy curve immediately rose to their maximum levels (approximately 1.0 for the SE and 0.5 for the FE) and then gradually decreased toward the end of the section (b), i.e. approximately from 1 to 0.75 for the SE and from 0.5 to 0.45 for the FE. In section (c), both entropy curves slowly increased and then slowly decrease toward the end of this section (the last entropy values are approximately 0.75 for the SE and 0.5 for the FE). This means that a reduction in degrees of irregularity occurred in the pre-perfomance period and peaked just before starting the performance period, while the higher degrees of irregularity were captured in the post-performance period.

- In section (a), the entropy curve of the CSE (the fifth graph from top of Figure 4.3) exhibited average high levels (approximately 0.75) but dramatically reduced to lowest levels (approximately 0.65) in the beginning of section (b). In section (b), the entropy curve increased and then slowly fluctuated toward the end of the section. In section (c), the entropy curve slowly declined and then rose toward the end of this section (the last entropy values are approximately 0.75). This means a high degrees of correlation in the performance period and low degrees of correlation in the performance period were captured.

- The LF/HF ratios showed the same trend as that of the CSE (the sixth graph from top of Figure 4.3), while the PSD of the LF and HF (the seventh graph from top of Figure 4.3) exhibited high levels in section (a) and steadily low levels in section (b) toward section (c) with a slight increase in their levels at the end of this section.

The entropy-based complexity measures and the LF/HF ratio suggested that the "high stress periods" corresponds to the pre-performance period (Section (a)), and the "low stress period or coping period" corresponds to the performance period (Section (b)) and lastly the "rest (recovery) period" corresponds to the post-performance period (Section (c)). Besides, the slightly higher levels of the PSD of LF than the levels of the PSD of HF occurred in the pre-performance which also suggests "high stress period", but the steadily low levels in performance period toward the post-performance period may be suggested as the "coping period" (the interpretation of stress mechanism from the LF/HF ratio, PSD of HF and PSD of LF should make with caution [101, 109, 110, 111, 112, 102]). The presenter of the oral presentation confirmed an increased level of stress before presenting and psychosocial engagement towards the end of the presentation due to questions of audience raised in between and after presenting.

4.4 Conclusions

Public presentations target to inform listeners in a structured, deliberate, and entertaining manner. They can take place in controlled environments - on stage - where the presenter regulates the process, or in settings which are highly interactive and require an increased engagement with the audience. Our study has proposed a new framework for the analysis of HRV in real-life public performances, in order to provide robust and accurate biomarkers of the evolution of stress. Novel R-peak and HRV analyses of mobile ECG in real-life scenarios have been established based on frequency-domain and nonlinear-domain metrics; SE, FE, CSE, PSD of LF, PSD of HF and LF/HF ratio. The analysis has shown a limitation of the frequency domain analysis when an occurrence of small values of the the PSD of the HF power (approaching zero), the LF/HF ratio can yield undefined value, so that this makes the LF/HF ratio rather sensitive compared ton other metrics, and should therefore be interpreted with caution. *Based on degrees of regularity, the SE, FE have shown*

that the pre-performance period corresponds to a stressful period for which entropy values decreased (low uncertainty), and the performance period corresponds to a coping period for which entropy values increased with fluctuations (high uncertainty). Our novel self-correlation based CSE has also revealed that a stressful period corresponds to the pre-performance period for which entropy values increased (high self-correlation), and a coping period corresponds to the performance periods for which entropy values decreased (low self-correlation). This corresponds to a new definition of the complexity loss theory: loss in uncorrelation-based complexity implies the occurrence of perceiving stress in humans. These entropy-based results correspond to the "General Adaptation Syndrome" (GAS) theory described in Chapter 1, section 1.1 and can be summarised as follows:

1. The high stress period occurs during the pre-performance period and corresponds to the alarm stage whereby the sympathetic nervous system activates to prepare the body for a fight or flight situation, and this results in the low level of the resistance to stress curve.

2. The low stress period occurs during the performance period and corresponds to the resistance stage whereby the parasympathetic nervous system activates to calm the body, and this results in the high level of the resistance to stress curve.

3. The rest (recovery) period occurs during the post-performance period and corresponds to the homeostasis stage whereby the less activation of both the SNS and PNS is presented, and this results in the intermediate level (rest) of the resistance to stress curve.

However, this study has been conducted only with two participants in a specific scenario (a conference presentation) which aims to determine a proof of concept regarding evolution of stress based on the GAS through complexity measures. To

this end, these entropy-based complexity measures have unveiled a physically meaningful interpretation for understanding the complex dynamics of HRV in response to an evolution of stress over time.

4.5 Future work

Future studies will investigate more closely the physically meaningful interpretation of structural complexity in relation to stress levels. This includes a collection of multichannel physiological data, such as ECG, respiratory signals, and Electroencephalogram (EEG), on public performances within a larger sample size. Standard protocols for systematic psychological and physiological stress assessment will also be conducted as a ground tooth.

Chapter 5

Stress Analysis though Entropy-based Complexity Measures for a Case Study: Music Performance

5.1 Introduction

The first attempt to introduce a taxonomy of stress dates back to Hans Selye in 1936, who defined stress as a "non-specific endocrine response" [113]. Current research explains stress through the modulation of the autonomic nervous system (ANS) resulting from physical, environmental, or other psychosocial stressors, where both the sympathetic (SNS) and parasympathetic nervous systems (PNS) are involved in the regulation of functions including heart rhythms, respiration, and blood pressure [114]. Music performance is a particularly apt domain for studying ANS reactivity to stress [115]. For professional musicians, the expectation to deliver high-quality performances—no matter where, when, and for whom—has been linked to debilitating and sometimes career-threatening mental and physical distress [115]. The majority of stress research into music performance has focused on the psychological construct of performance anxiety using questionnaires, while neglecting the objective assessment of corresponding physiological components. While research into physiological stress in musicians has usefully examined HR [116, 117, 118, 119] rather than the dynamically more informative heart rate variability (HRV). The analysis of HRV in the time, frequency, and nonlinear domains is now widely used to assess the biomarkers of stress. In particular, the high frequency (HF) power in HRV is considered to reflect PNS activity influenced by vagal control, while the low frequency (LF) power is multifaceted and was previously believed to reflect SNS activity. The

ratio of the power in the LF to HF frequency bands (so-called LF/HF ratio) was long thought to indicate the degree of sympathovagal balance; the higher the ratio, the greater the dominance of SNS, while a lower ratio was thought to suggest the dominance of PNS activity [120, 11]. However, the LF/HF ratio is not a reliable indicator of stress, as the LF band reflects both SNS and PNS activity due to the nonlinear behavior of the vagus nerve [101, 109, 110, 111, 112, 102]. Nevertheless, in many psychophysiological stress studies [121, 122, 123, 124, 125, 126], stressors have been found to be associated with an increase in the LF band and a decrease in the HF band. Although the analysis of HRV in the frequency domain can identify and capture changes in stress, nonlinear analysis in the form of structural complexity has recently been used to quantify degrees of determinism versus randomness in signals and has become prevalent [34, 13, 14, 15]. This nonlinear metric is conveniently interpreted though the "Complexity Loss Theory (CLT)" [27], which asserts that physiological responses in organisms under constraints (illness, ageing, and other inhibitions such as stress) exhibit lower structural complexity (fewer degrees of freedom) than physiological responses in healthy organisms. Among the available entropy measures, the data-driven Sample Entropy (SE) methods are particularly interesting; low levels of SE indicate a time series of high regularity, while increasing values of SE correspond to a higher degree of irregularity [13, 97]. An improved version of the SE method called Fuzzy Entropy (FE) has also been recently utilised [14, 40, 41, 42]. However, neither completely deterministic nor purely stochastic data are truly complex, as structural complexity is reflected in long-range correlations. Most studies of complexity loss in HRV have been conducted in the context of understanding cardiovascular diseases. A recent study on psychosocial stress in public performance [62] was conducted with a single expert pianist and provided evidence of a reduction in structural complexity in HRV in response to increased stress levels [62, 43, 127, 128, 59]. The aim of the present study, therefore, is to establish a systematic approach to the examination of physiological stress in music

performance contexts. The evolution of stress responses to performance was modelled over a cohort of 16 musicians whose electrocardiograms (ECGs) were recorded for 5 min prior to and 5 min during two performances [98]: i) a low-stress condition with no audience present, and ii) a high-stress condition in front of an audition panel. An audition was deemed particularly well suited for the high-stress scenario, owing to the scrutiny under which musicians are placed. Auditions also allow enhanced experimental control and maintain high ecological validity through the assignment of appropriate pieces to be played and the possibility of demarcating precise timings before and during performance. We used modern wearable sensing devices for the collection of ECG data and advanced analysis techniques to capture the signature of stress. Specifically, Multiscale Sample Entropy (MSE) [15] and Multiscale Fuzzy Entropy (MFE) [129] and our novel Multiscale Cosine Similarity Entropy (MCSE) approaches were introduced in order to examine entropy values over increasing time scales, thus producing so-called complexity profiles. In this way, not only do we account quantitatively for objective aspects of performance stress, but we are also able to identify the critical timing of stress reactivity and estimate the most appropriate period during which to intervene using stress management strategies.

5.2 Materials and Methods

5.2.1 Participants

Eleven violinists from the Royal College of Music (RCM) and five flutists from the Conservatory of Southern Switzerland (CSI) participated in the study. The cohort consisted of healthy male (n = 9) and female participants (n = 7) with a mean age of 23.12 ± 2.42 years (range 19-27), all of whom were advanced music students with at least 10 years of public performance experience. Recruitment at the RCM took place from October 2012 to March 2013, with data collection in March 2013, while recruitment at the CSI took place from March to April 2011,

followed by data collection in May 2011. Participants were assigned to perform individually the Allemande from J. S. Bach's Partita No. 2 in D minor for solo violin (BWV 1004) or the Allemande in A minor for solo flute (BWV 1013).

5.2.2 Physiological and Psychological Measures

For the violinists, ECG was recorded using the Bioharness, a physiological monitoring device from ZephyrTM which has been validated in a similar scenario by Johnstone and colleagues [130, 131]. The raw signals were acquired at a sampling rate of 250 Hz. For the flutists, ECG was collected using the PowerLab (model 26T), a similar acquisition device from ADInstruments. Electrodes were attached at the chest and intercostal spaces (between ribs VI and VII). The raw signals were acquired at a sampling rate of 1,000 Hz.

5.2.3 State Anxiety

Prior to each performance, participants completed Form Y1 of the State-Trait Anxiety Inventory (STAI) [132], a 20-item questionnaire which assesses the emotional state of a person based on subjective feelings of nervousness. Each item is rated on a 4-point scale (1 = almost never to 4 = almost always) with cumulative scores ranging from 20 (low anxiety) to 80 (high anxiety). For reference, the moderate-level score among young men is 36.47±10.02, and among young women, it is 38.76±11.95 [132].

5.3 Experimental Design

5.3.1 Induction Session

Before conducting the experiment, every participant attended a 20-minute induction session and confirmed their willingness to deliver multiple polished performances (on separate days) of either the Allemande from J. S. Bach's Partita No. 2 in D minor for solo violin (BWV 1004) or the Allemande in A

minor for solo flute (BWV 1013). The performance conditions were explained: i) the low-stress condition involved the assessment of physiological responses during a private performance without any external attendees apart from the researchers managing the measurement, ii) the high-stress condition was a performance in front of an audition panel, composed of three members of staff from the RCM (for violinists) and the CSI (for flutists). The participants were also required to provide background information on their musical experience and general health. On the day of each performance, all participants confirmed that they had not taken anxiolytic medications or other substances that may affect their perceptions and physiological responses to the performance scenarios.

5.3.2 Recording Protocol

The low- and high-stress performances were scheduled on separate days, and the order was counterbalanced across participants. The musicians were asked to arrive 30 minutes before the pre-performance period for the attachment of the ECG recording devices and also for usual performance preparation (e.g. warming-up, tuning, and rehearsing). Stage calls were given at 20 minutes and 10 minutes before performance by a member of the research team acting as the "backstage manager". At 5 minutes before performance, participants were brought to a backstage area and asked to complete Form Y1 of the STAI. The backstage manager then gave a confirmation signal and allowed the participant to enter the performance room; this period is referred to as pre-performance (PP). It is important to note that the pre-performance includes the 2-3 minutes needed to walk into the performance room and settle for the performance. The participants then performed the designated pieces, for approximately five minutes in duration (5.06 ± 0.22 minutes for the violinists and 5.19 ± 0.10 minutes for the flutists); this period is referred to as performance (P). Time labels were manually marked by the research team for every condition analyzed. In addition to the ECG recordings, all performances

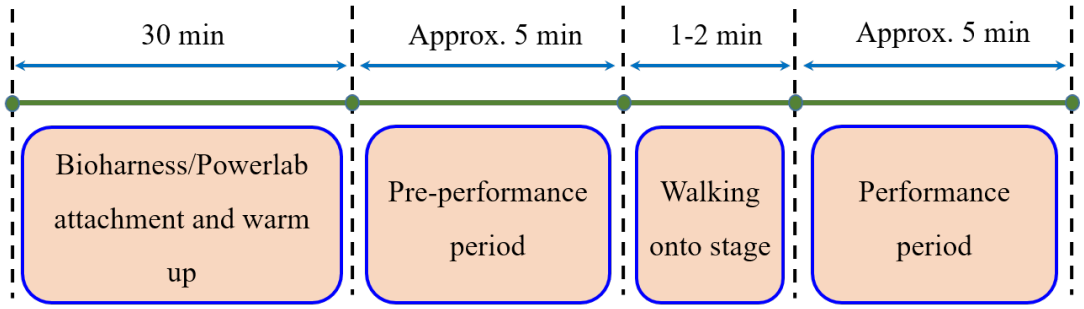

Figure 5.1: **The experimental protocol**. The timeline was designed for collecting physiological data from the participants experiencing the low- and high-stress conditions.

were recorded using a video camera. The experimental protocol is summarized in Figure 5.1.

5.4 Data Analysis

5.4.1 Pre-processing

The R-peaks in the recorded ECGs were detected using a combination of matched filtering and Hilbert transform algorithm [57], with the initial QRS complex identified based on a search for ventricular depolarization (QRS) patterns in the segmented windows of ECG data. The RR intervals were then created by subtracting the time-intervals of consecutive R-peaks. However, premature ventricular contractions, or ectopic beats, present in the original RR intervals are known to adversely affect the results from any analyzing metrics [63, 133]. To this end, a custom-made algorithm developed for detecting anomalous peaks in the RR intervals was used to address those erratic behaviors. The detected anomalous beats were then replaced by interpolated data, generated using a smoothing function; this resulted in normal sinus to normal sinus intervals (NN intervals). The HRV signals were then generated from the NN intervals using cubic spline interpolation at the sampling frequency of 8 Hz [134]. The HRV signals were segmented into the pre-performance (PP) and performance (P) periods using the time labels created during the experimental

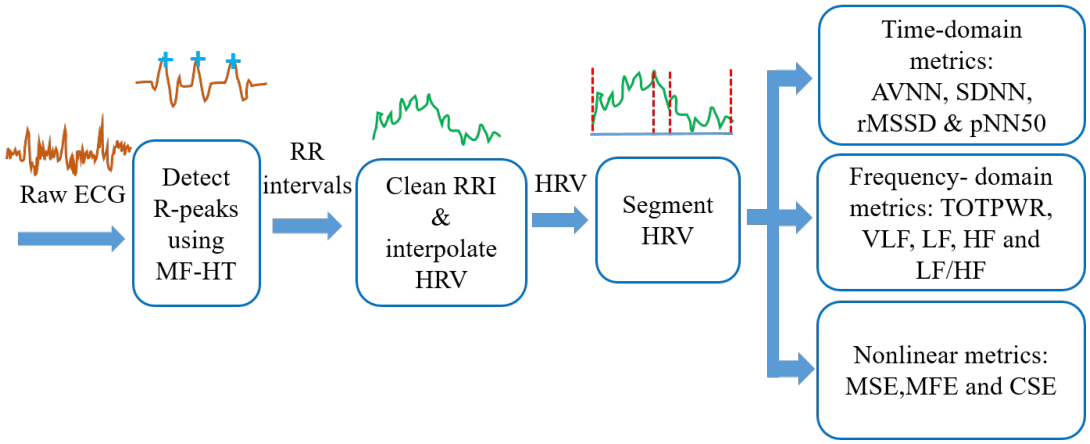

Figure 5.2: **A conceptual block diagram of the proposed framework for analysing stress in musicians**. MF-HT stands for the combination of matched filter and Hilbert transform algorithms, while PP and P respectively designate the periods pre- and during performance.

setup. The block diagram of the whole analysis framework is shown in Figure 5.2, and an example of the HRV is shown in Figure 5.3.

5.4.2 Time, Frequency and Complexity analyses

The analyses were performed in the time, frequency, and nonlinear domains. The averages of NN intervals (AVNN), the standard deviation of all NN intervals (SDNN), the square root of the mean of the squares of the differences between adjacent NN intervals (rMSSD), and the percentage of differences between adjacent NN intervals (pNN50) were used as standard time-domain metrics [135]. For the power spectral density (PSD) analysis, the aggregate PSDs in the low frequency band (LF: 0.04-0.15 Hz) and high frequency band (HF: 0.15-0.4 Hz) were computed using the Welch PSD estimator; the ratio between the power of the LF and HF bands (LF/HF) was calculated as an additional metric. For the nonlinear analysis, the MSE, MFE and MCSE were computed for quantifying degrees of structural complexity of the extracted HRVs over ten scales. The selected parameters for the MSE, and MCSE were: embedding dimension $m = 2$, tolerance level $r_{se} = 0.15$ times the standard deviation of the data, $r_{cse} = 0.07$

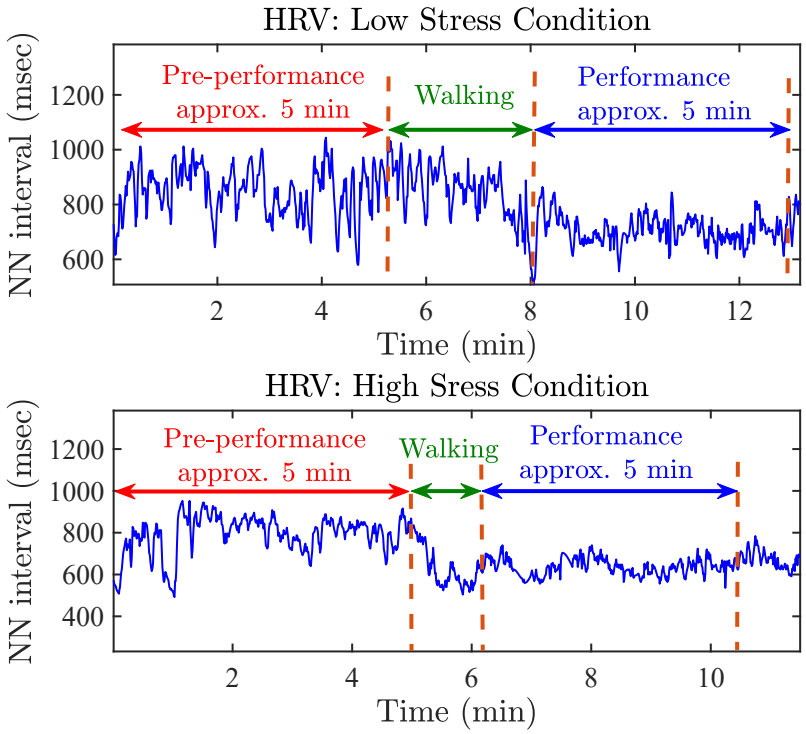

Figure 5.3: **An example of the extracted HRV of musicians**. HRV signal of a participant, interpolated from the NN intervals in the low- and high-stress conditions.

(see more details in Chapter 3) time lag, $\tau = 1$ [15], while the optimal parameters used in MFE were found empirically: embedding dimension $m = 2$, tolerance level $r_{fe} = 0.01$, time lag $\tau = 1$, and a second order Gaussian is used as a fuzzy membership function. The areas of the entropy curves over the whole ten scales (the complexity profiles) were computed and were considered as the nonlinear metric. The t-test was used to examine statistical differences in each time, frequency and nonlinear metric according to four possible comparisons: i) high-stress: pre-performance (PP) vs performance (P), ii) low-stress: pre-performance (PP) vs performance (P), iii) pre-performance (PP): low- vs high-stress, and iv) performance (P): low- vs high-stress (see Table 5.1). Scores on the state anxiety inventory (STAI-Y1), completed before the low- and high-stress performances, were compared using a paired-samples t-test.

Table 5.1: **Statistical tests of frequency and nonlinear metrics**. The unit of AVNN, SDNN, rMSSD, and pNN50 is millisecond (msec) and the unit of the TOTPWR, VLF, LF, and HF is s^2/Hz. Note. PP = pre-performance period; P = performance period; AVNN = the averages of NN intervals; SDNN = standard deviation of all NN intervals; rMSSD = square root of the mean of the squares of the differences between adjacent NN intervals; pNN50 = percentage of differences between adjacent NN intervals; TOTPWR = total NN interval spectral power; VLF = power in the very low frequency band (0.003-0.04 Hz); LF = power in the low frequency band (0.04-0.15 Hz); HF = power in the high frequency band (0.15-0.4 Hz); LF/HF = ratio between the power of the LF and HF bands; MSE = multiscale sample entropy; MFE = multiscale fuzzy entropy. Bold indicates $p \leq 0.05$ (based on Bonferroni correction with a selection of 5% significant level among 11 metrics).

Metrics	Discriptive statistics				Statistical comparisons			
	Low stress: PP mean±sd	Low stress: P mean±sd	High stress: PP mean±sd	High stress: P mean±sd	Low stress: PP vs P t_{15}, p	High stress: PP vs P t15, p	PP: low vs high stress t15, p	P: low vs high stress t15, p
Time-domain								
AVNN	624.0±78.6	637.2±108.2	557.5±91.9	555.3±115.0	-0.52, 0.61	0.07, 0.95	3.00, 0.09	**4.01, 0.001**
SDNN	51.4±20.6	42.4±17.5	48.7±21.6	38.6±18.8	1.77, 0.10	1.30, 0.21	0.49, 0.63	0.97, 0.35
rMSSD	22.5±10.9	23.8±12.4	16.2±7.7	16.4±6.4	-0.43, 0.67	-0.07, 0.95	0.27, 0.02	2.97, 0.01
pNN50	2.7±3.5	2.8±4.3	1.3±1.5	0.7±0.9	-0.06, 0.96	1.26, 0.23	1.98, 0.07	2.02, 0.06
Frequency-domain								
TOTPWR	51.79±14.37	36.50±12.35	41.42±16.78	26.41±12.16	**5.29, 0.0001**	**4.10, 0.001**	2.89, 0.01	**3.43, 0.004**
VLF	51.61±14.28	36.41±12.30	41.28±16.70	26.35±12.13	**5.27, 0.0001**	**4.09, 0.001**	2.90, 0.011	**3.43, 0.004**
LF	0.168±0.126	0.087±0.080	0.146±0.117	0.062±0.070	**3.28, 0.005**	2.22, 0.04	0.61, 0.55	1.12, 0.28
HF	0.037±0.037	0.026±0.027	0.020±0.018	0.013±0.010	1.18, 0.26	1.56, 0.14	2.26, 0.04	2.56, 0.02
LF/HF	5.51±2.82	3.78±1.93	7.31±3.69	5.92±9.71	2.24, 0.04	0.5, 0.62	-2.00, 0.06	-1.02, 0.32
Nonlinear analyses								
MSE	9.54±1.56	11.50±1.85	8.00±1.41	10.18±1.91	**-3.97, 0.001**	**-3.61, 0.003**	**4.88, 0.0002**	1.97, 0.07
MFE	11.70±1.64	13.61±1.90	10.00±1.64	12.39±1.84	**-3.71, 0.001**	**-3.71, 0.002**	**4.85, 0.0002**	1.79, 0.09
MCSE	6.37±0.45	5.94±0.55	6.65±0.33	6.31±0.62	**1.95, 0.004**	-2.37, 0.07	-2.37, 0.03	-1.99, 0.07

5.5 Results

5.5.1 Time, Frequency and Complexity Metrics Results

Table 5.1 shows that the average and the root mean square of the extracted HRV signals (AVNN and rMMSD) from the low-stress condition (performed without judges) were higher than those from the high-stress condition (performed in front of three judges); in other words, the cardiovascular reactivity of the participants was pronounced in the high-stress condition. However, none of the time-domain metrics shows significant differences in any of the four comparisons except the AVNN metric, which shows discrimination for the performance period where the low- and high-stress conditions were compared. In the frequency domain, the mean power of all frequency bands (TOTPWR, VLF, LF, and HF) showed decreases from the pre-performance to the performance periods, and from the low- to high-stress conditions. The statistical differences between three comparative scenarios (i.e. two periods of performances and the high- vs low-stress in the performance period) were significant for the TOTPWR and VLF metrics. However, the LF metric indicates statistical discrimination only between the two performance periods, while the HF and the LF/HF ratio metrics indicates no statistical discrimination for any of the comparisons. In the nonlinear domain, both MSE and MFE yielded i) an increase in mean entropies from the pre-performance to performance periods; and ii) a decrease in mean entropies from the low- to high-stress condition. Statistical comparisons revealed significant differences between most cases for both MSE and MFE, except for the comparison of the low- and high-stress conditions for the performance period. The results of both the MSE and MFE corresponded to our CLT-based assumptions for which a reduction in degrees of irregularity is due to i) perceiving stress in a stressful circumstance (high stress condition), and perceiving a period of stress (pre-performance period). Besides, the MCSE yielded i) a decrease in mean entropies from the pre-performance to the

performance periods, and ii) an increase in mean entropies from the low- to high-stress condition. Statistical comparisons revealed significant differences only for the comparison of the pre-performance and performance periods (under the low-stress condition). Even though the results of the MCSE did not give statistical separations for all comparisons, the MCSE gave another a physically meaningful perspective on self-correlation-based complexity, i.e. a decrease in degrees of uncorrelation (an increase in mean entropies estimated from the MCSE) is due to i) perceiving a stressful circumstance (high stress condition), and ii) perceiving a period of stress (pre-performance period).

The complexity profiles of the four comparisons through the MSE, MFE and MCSE were plotted as mean entropies and their standard errors (se), as shown respectively in Figure 5.4, Figure 5.5 and Figure 5.6.

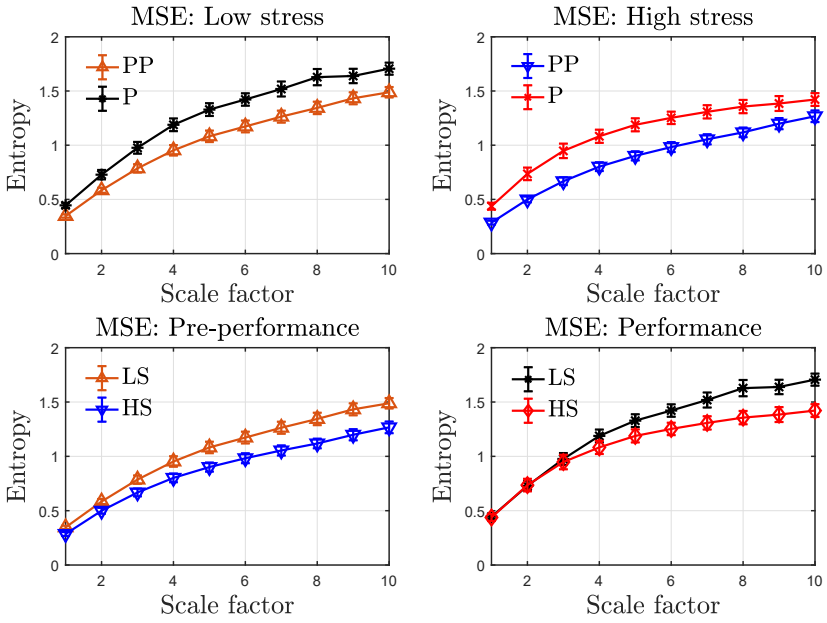

Figure 5.4: **MSE complexity profiles of the HRVs obtained the musicians.** All curves are plotted as mean entropies and their standard error against the scale factor. LS, HS, PP and P are abbreviations for the low- and high-stress conditions, the pre-performance and performance periods, respectively.

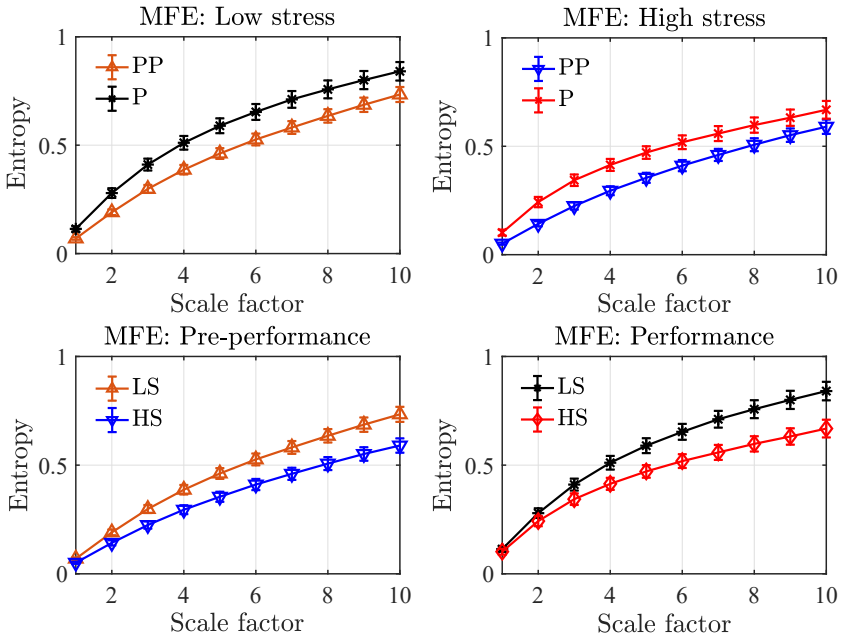

Figure 5.5: **MFE complexity profiles of the HRVs obtained from the musicians.** All curves are plotted as mean entropies and their standard error against the scale factor. LS, HS, PP and P are abbreviations for the low- and high-stress conditions, the pre-performance and performance periods, respectively.

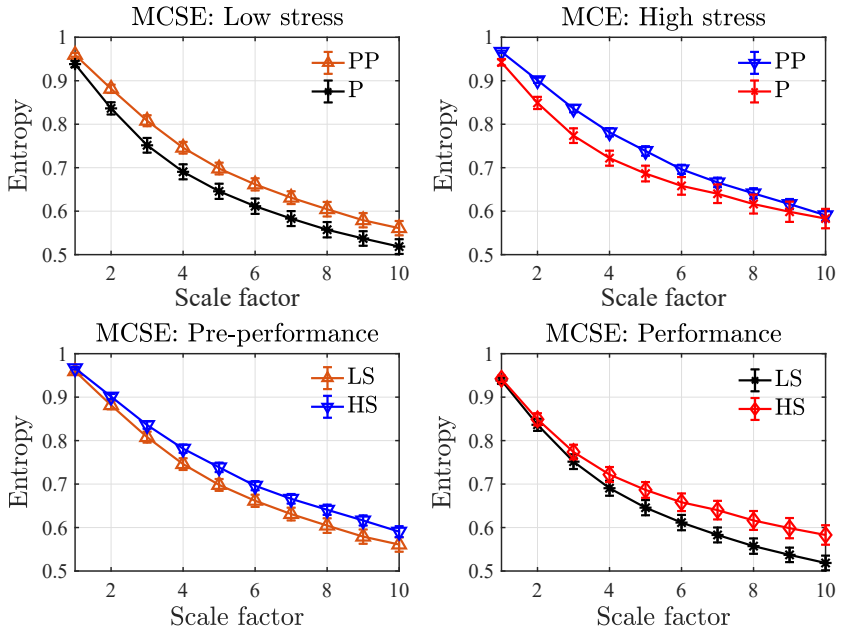

Figure 5.6: **MCSE complexity profiles of the HRVs obtained from the musicians.** All curves are plotted as mean entropies and their standard error against the scale factor. LS, HS, PP and P are abbreviations for the low- and high-stress conditions, the pre-performance and performance periods, respectively.

5.5.2 State Anxiety Result

The reported state anxiety of the musicians was significantly higher in the high-stress condition (mean = 39.12±7.04) than in the low-stress condition (mean = 34.37±7.88) t15= -2.594, p-value ≤ 0.05, confirming that the high-stress condition was indeed experienced by the participants as more anxiety provoking than the low-stress condition.

5.6 Discussion and Conclusions

We have examined the cardiovascular reactivity of musicians experiencing low- and high-stress performance conditions within the framework of CLT, quantified using the Multiscale Sample Entropy (MSE), Multiscale Fuzzy Entropy (MFE), and our novel Multiscale Cosine Similarity Entropy (MCSE) algorithms. Unlike standard questionnaire-based anxiety assessments, this has been achieved through a suite of objective stress measures based on physiological responses to stress in two scenarios, low- versus high- and before- versus during-performance. Advanced signal processing algorithms for R-peak detection and HRV extraction (Matched Filtering and Hilbert Transform; MF-HT) have been employed to deal with noisy cardiac data in real-life scenarios, while state-of-the-art data analysis techniques in the time, frequency and nonlinear complexity domains have been used to quantify the signatures in HRV related to stress in performance. The analysis has also revealed that currently used spectral analyses of HRV may be inadequate for detecting stress reactivity, as exemplified by the statistically non-significant findings reported in Table 5.1. The time-domain analysis based on the AVNN and rMMSD metrics has suggested that, in high-stress condition, the heart rates of the participants were higher than in low-stress condition. However, these higher heart rates were accompanied by a smaller difference in

heart rate variability when comparing the pre-performance and performance periods, in all time-domain metrics. The standard HRV frequency analysis showed decreases in the LF and HF powers from the pre-performance to performance period, and from the low- to high-stress condition, suggesting a shift of vagal activity from the HF to LF band [14, 15, 27, 62, 34, 13] or, in other words, a signature of both SNS and PNS in the LF band[121, 122, 123, 124, 125, 126]. This has revealed higher stress in the pre-performance period than during the performance. Our nonlinear analyses have shown that the MSE and MFE approaches have achieved robust discrimination of the underlying features related to the dynamics of the heart, regulated by the autonomic nervous system. Based on the CLT, both MSE and MFE have shown that the transition period from pre-performance to performance corresponds to a reduction in stress levels in the musicians. The same complexity pattern was presented in the discrimination from the high-stress condition to the low-stress condition. Furthermore, our novel entropy measure, the MCSE, has revealed an increase in structural complexity from the low- to high- stress condition and for a transition period from the pre-performance to the performance. This corresponds to a new definition of the CLT: *loss in uncorrelation-based complexity implies the occurrence of perceiving stress in human.* For rigour, these objective stress metrics have been benchmarked against the subjective state anxiety scores, where the low-stress and high-stress conditions corresponded respectively to lower and higher anxiety reported by the musicians.

In this study, we have used both wearable and stationary physiological recording devices and have addressed the imperfections and artefacts in such real-world data through advanced data analysis methods. Our study has focused on combining physiological and psychological measures, analyzed within the framework of the complexity loss theory, to analyze data from a number of performers and to extend a previous single-person study, to address a more

general issue of musicians' emotional and physiological adaptability to psychosocial stressors.

5.7 Future work

Subsequent work will consider joint analysis of multivariate physiological data, such as HRV, respiration rate, Electromyogram (EMG), and skin conductance. The collection, analysis and examination of multivariate data, in relation to strategies for managing stress and enhancing performance quality, promises to offer personally and professionally significant advancements in musicians' training and skill development, particularly if targeted at the sensitive period before performance, as shown in this study, and employed in a range of performance contexts.

Chapter 6

Analysis of Financial Data through Complexity Science

6.1 Introduction

Indices of major stock markets are generally accepted as indicators of the financial health and economic wellbeing [136, 137]. Given their close link with socio-economic and geo-political factors (here, we refer to those as 'events') the latent dynamics of stock indices are also a reliable indicator of the influence those events have on the health of the financial system. To put this into context, in the last 25 years the US alone have been through a number of events, including the "Dot-com Boom" in the 1990s, the 9/11 terrorist attack in 2001 and the sub-prime mortgage crisis in 2008. It is therefore natural to ask whether a general health of the economy, seen through the lens of stock indices, can be assessed in a way analogous to the way we examine health of living organisms. This motivates us to embark upon the significant body of work on human stress in order to derive indicators of 'stress' of the financial system and establish 'biomarkers' of characteristic events in stock indices. To this end, we employ the so-called "Complexity Loss Theory" which states that organisms experiencing constraints (illness, ageing, stress) exhibit lower structural complexity of their physiological responses than healthy organisms. Our analysis falls under this general umbrella, but is finance-specific and employs non-parametric analyses of the determinism (via predictability), nonlinearity, multiscale entropy, and synchrony, within an intrinsic multivariate analysis framework.

In technical terms, stock indices exhibit trends – local and global 'first order' characteristics [138] – together with economic and non-economic cyclical influences

(e.g. the four-year presidential cycle in the US) and effects of our habits, such as the Sell in May stock trading strategy and the Christmas sales effect [139]. Trends in financial indices are perhaps their most examined characteristics, with both numerical and graphical methods used for their detection. Stock market volatility, on the other hand, reflects the degree of uncertainty in stock indices. Financial analysts are therefore interested in patterns in historical data in order to predict financial crashes – an often disputed practice called "Technical Analysis" [140, 141]. A very popular numerical technical analysis method is the class of moving-average (MA) algorithms which yield indicators of general movements of stock prices such as: i) price moving average for raw data with trend, and ii) rate of change at different scales, for detrended data. The price moving averages allow investors to compare fluctuations in stocks to the trends over time, while the rates of change are relatively faithful indicators of the momentum of stocks. For example, a positive value of the rate of change suggests enough market support to continue driving prices in the direction of the current trend, while its negative value indicates lack of market support and tendency for stock values to become stagnant or to reverse.

The "Efficient Market Hypothesis" (EMH) is a cornerstone of modern financial theory and states that current security prices (the underlying value of the asset) incorporate and reflect all relevant information that could be gathered, so that stocks always trade at fair value [56]. This implies that in 'normal' situations markets cannot be consistently beaten over long time; in other words, the security prices tend to exhibit a random walk type of behaviour, characterised by poor predictability from their historical values and *high uncertainty* in the rate of change of stock prices. However, when speculative economic bubbles – 'abnormal' situations – occur, the markets are often driven by buyers who are prone to sentiment or irrational exuberance. In such scenarios, the buyers tend to overestimate stock values while anticipating the growth of markets, which in turn brings *less uncertainty* to the rate of change of future prices. This 'acceleration-stabilisation' type of behaviour is not dissimilar to the

sympatho-vagal balance in humans, whereby the sympathetic autonomous nervous system (SNS) accelerates body functions while the parasympathetic nervous system (PNS) slows them down [142].

In human sciences, stress is defined as a non-specific neuroendocrine response [1]. In the same way, we propose to define the financial stress as a non-specific deviation from its normal functioning. There is no agreement on a more specific definition, as episodes of financial stress often vastly differ, from dot-com bubble through to sub-prime mortgage crisis. A risk (stress) indicator specific to currency markets was proposed in [143], and defines financial risk through a reduction in the number of significant factors – principal components. However, the suggestions that a decrease in the degrees of freedom invariably signifies the loss of complexity during an episode of crisis is not necessarily valid; to this end, higher-order features related to long-range couplings also need to be examined [144], for example those manifested in long-term correlation, which is the basis for practical structural complexity analysis. The degree of determinism (predictability) of the signal, in addition, also plays an important role in determining the degree of complexity [145].

During a financial crisis, the term "systemic risk" refers to a series of correlated defaults among financial institutions, occurring over a short time span and triggering withdrawal of liquidity and a widespread loss of confidence in the financial system as a whole. At the heart of the concept is the notion of 'contagion', a particularly strong propagation of failures from one institution, market, or system to another. The financial stress index (FSI) proposed in [146] considers the variations in the intensity and duration of financial stress episodes through high-frequency price variables. Based on an equal-variance weighted average, financial stress is detected when the value of the FSI exceeds one standard deviation above the trend; the FSI also indicates whether an episode of financial stress is due to stress in banking, securities, or foreign exchange sectors.

The *absorption ratio* [147] is an indicator of market fragility and systemic risk, and is defined as the fraction of the total variance of a set of assets explained or absorbed by a finite set of eigenvectors. A high value for the absorption ratio corresponds to a high level of systemic risk and fragility. For example, high values of absorption ratio of the US stock market during the dot-com bubble and the global financial and sub-prime mortgage crises suggested that the market was extremely fragile (susceptibility of a financial system to large-scale financial crises caused by small, routine economic shocks [148]) and vulnerable to shocks (unexpected or unpredictable events that affect an economic positively or negatively and is measured by an impulse response function [149]). The absorption ratio can also be used as a warning for investors, as on average, stock prices decreased following one-standard-deviation spikes in the absorption ratio, and increased after one-standard-deviation drops in the absorption ratio. The '10-by-10-by-10' approach for the assessment of systemic financial risk related to stress scenarios was proposed in [150], and involves three factors: financial institutions, a number of counterparties and stress tests. The total of gains and losses of each stress test for each institution (also counterparty) is calculated and then reported periodically.

This all indicates a void in the literature when it comes to the quantification of both financial stress and systemic risk. To this end, in an analogy to human stress (sympatho-vagal imbalance) the signatures of which are derived by the sum of power spectrum at the the low-frequency (LF) band (0.04-0.15 Hz) and the sum of the power spectrum at the high-frequency (HF) band (0.15-0.4 Hz) within heart rate variability (HRV), we propose the Assessment of Latent Index of Stress (ALIS) which examines the LF and HF bands in detrended financial data. Our rationale is that low-frequency changes (LF band), which correspond to time spans of over 1 year, are driven by global factors (monetary policies), whereas the more rapid changes (HF band), over spans of 5 days to 3 months, signify abrupt events, such as the 9/11 crisis and the Internet bubble burst.

The ALIS index therefore determines 'crisis versus no-crisis' episodes of the financial stress evolution through the examination of long- and short-term changes in specific stock indices, whereas the existing FSIs in [146, 151, 152] consider several sub-components, such as stock market returns and time-varying stock market return volatility, which may be responsible for the onset and development of financial stress. While the ALIS index is not designed for specific analyses using financial market variables as potential co-founders for financial stress, it is one of the first methods which extends beyond the second order analysis in [146, 151, 152] to detect the patterns of financial crises in specific financial indices using a bio-inspired signal processing approach.

6.2 Summary of Motivation and Contribution

Inspired by the catastrophe theory [153] and the EMH theory, we propose the ALIS index as an indicator of financial stress during episodes of financial crises in different individual stock indices. Following on the complexity-loss theory, financial systems are shown to exhibit lower levels of structural complexity during financial crises (low uncertainty, i.e. the patterns of indices are easy to predict since investors are prone to do the similar activities), compared to normal periods [136]. We also introduce the moving-average multivariate sample entropy (MA-MSE) algorithm to quantify different degrees of such complexity.

It is almost self-evident that financial markets exhibit high structural complexity since activities of each investor (a small unit/element) can vary in terms of an amount of buys or sells (amplitudes) and when to make a decision (a response time), both of which depend on a reaction to simulators, such as news and regional/international regimes. This yields a series of a complex aggregation of average prices which fluctuates over time. which in turn can be quantified through entropy, for example, using the multivariate multiscale sample entropy (MMSE) algorithm [144, 53]. This approach examines long-term correlations of both the trend and the detrended data. For enhanced resolution, we introduce a

novel MA-MSE algorithm, described in Section 6.3.2. Also, prior to modelling financial indices, it is a prerequisite to establish the ground truth for the linear versus nonlinear and deterministic versus stochastic nature of the data, referred to as *signal modality analysis*.

In the analysis, we consider four major stock indices which indicate the state of economy of the US [136]: i) Dow Jones Industrial Average (DJIA), ii) NASDAQ Composite, iii) Standard & Poor's 500 (S&P 500), and iv) Russell 2000. The DJIA comprises 30 of the largest companies in the US across a range of industries except for transport and utilities; NASDAQ is an indicator of the performance of stocks in technology and of the growth in companies; S&P 500 consists of 500 large companies from a vast number of industries, each having market capitalisation of more than $5 billion; and Russell 2000 comprises a small-cap segment of the US equity market.

It is arguable whether increased local variances may signify financial crises, without assistance of sophisticated numerical methods. The studied non-parametric methods, however, are independent of signal variance which being only a 2^{nd} order moment may not effectively reveal *major* financial crises. Indeed, we show how such crises can be precisely determined through changes in the intrinsic characteristics of financial data, such as their determinism, linearity, and complexity. The purpose of this study is therefore to quantify these time-varying characteristics in order to simultaneously characterise, in a full multivariate way, the financial stress through the complexity-loss hypothesis (systems under stress exhibit greater regularity and less freedom.) [51, 154, 76] and systemic risk (the markets are contagious and behave in the same way during financial crises). This is achieved by examining in stock trends intrinsic and inter-channel dependencies together with their nonlinear and stochastic properties. The detrended stock indices (the rate of change) of the market indices over the last 25 years (between 1st January 1991 and 31st August 2015) were analysed using the following non-parametric methods: i) multivariate

multiscale sample entropy (MMSE), ii) moving-average multivariate sample entropy (MA-MSE). The analysis is verified over several case studies which support the complexity-loss hypothesis for financial markets, a robust framework to understand financial stress, and is expected to be beneficial to those interested in middle- and long-term investments.

6.3 Algorithms and Background

We shall first briefly describe the algorithms used in this study.

6.3.1 Moving-average (MA) Method for the Multivariate Data Analysis

This standard approach considers a multivariate signal $x_{org,k,i},\ k = 1, 2, \ldots, p,\ i = 1, \ldots, N$, with ρ being the number of data channels and N the total number of sample points. The moving-average filter removes the trend, $s_{k,j}$, from the original $x_{org,k,i}$, using the following functional form

$$s^{\varepsilon}_{k,j} = \frac{1}{\epsilon} \sum_{i=j}^{j+\tau-1} x_{org,k,i}, \quad 1 \leq j \leq N - \tau + 1, \tag{6.1}$$

where ϵ is a pre-defined scale factor (data window size). The detrended data, $z_{k,j}$, is then obtained as

$$z^{\epsilon}_{k,j} = x_{org,k,i} - s^{\epsilon}_{k,j}, \quad i = 1, 2, \ldots, N - 1 \tag{6.2}$$

Observe that long window sizes will remove short trends. An example of using 5-day scale for the MA is shown in Figure 6.1

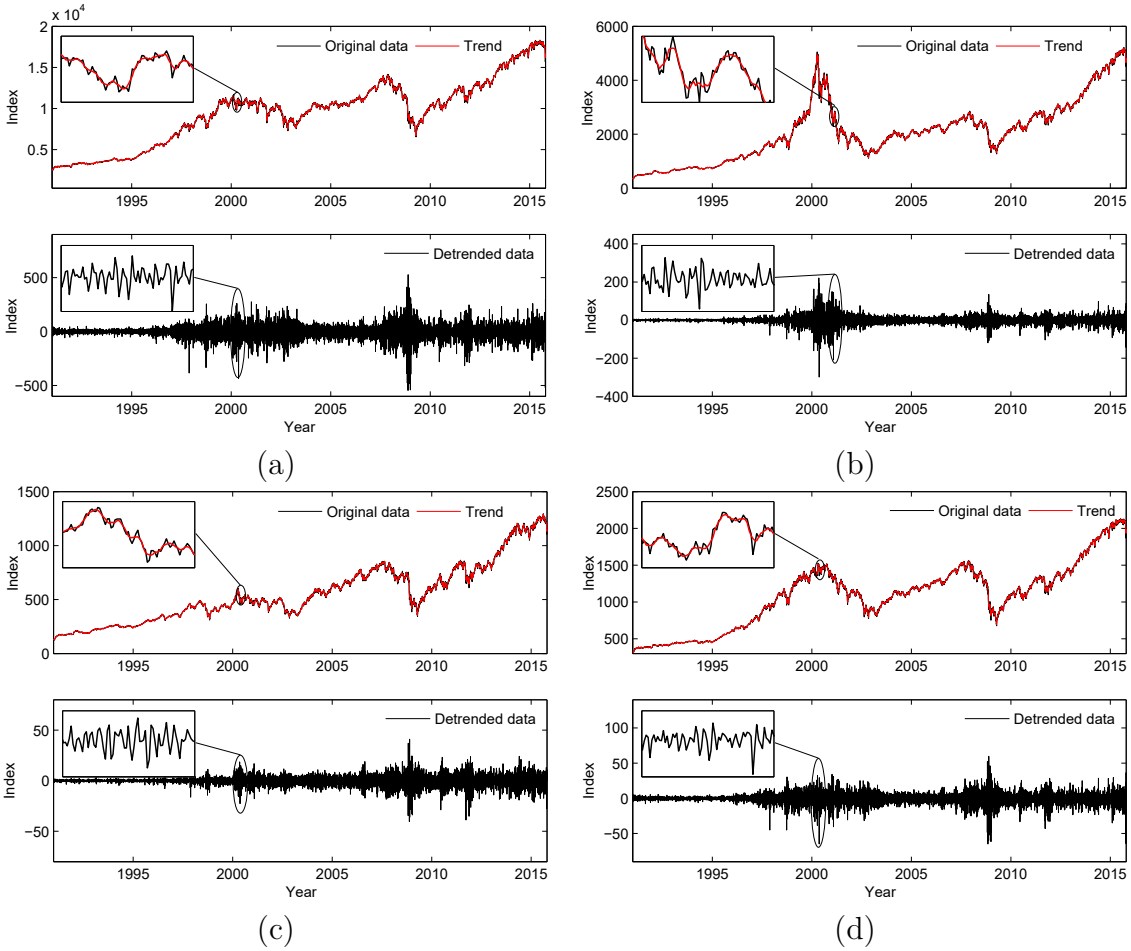

Figure 6.1: **Stock market indices (DJIA, NASDAQ, Russell 2000 and S&P 500) and their detrended versions.** *Upper panels*: Original data and their trends for a 5-day scale. *Lower panels*: Detrended data. and their trends for a 5-day scale. *Lower panels*: Detrended data. (a) The DJIA over 1991–2015. (b) The NASDAQ over 1991–2015. (c) The Russell 2000 over 1991–2015. (d) The S&P 500 over 1991–2015.

6.3.2 Multivariate Multiscale Sample Entropy (MMSE) and Moving-average Multivariate Sample Entropy (MA-MSE)

The Sample Entropy (SE) method calculates empirical estimates of entropy [13] based on the probability of similarity between the delay vectors (patterns) in data. The SE is a single-scale measure, however, the interpretation of complexity

estimated via entropy requires multiple scales. To this end, the multiscale sample entropy (MSE) algorithm [15] employs pre-determined scales, constructed using the coarse graining process (CGP). However, the CGP reduces a number of sample points of an original time series when increasing scales factor, i.e. for a given scale, ϵ, $N_\epsilon = \frac{N}{\epsilon}$, decreases linearly in the scale factor, which may results in undefined entropy at high scale factors. For better resolution, the modified multiscale entropy (Mod-MSE) [80] algorithm replaces GCP by a moving-average (MA) scale definition process. Both the MSE and the Mod-MSE are, however, univariate algorithms, not capable of accounting for cross-channel dependencies. To cater for multivariate cases, the multivariate MSE (MMSE) [144, 53], reveals both the intrinsic- and cross-complexities through a multivariate embedding process. We here introduce its variate, termed MA-MSE, to quantify multivariate complexity of *both* the trend and the detrended data, a procedure referred to as the moving-average multivariate sample entropy (MA-MSE), outlined in Algorithm 6.1. By virtue of MA-MSE, pre-defined and physically meaningful scales are generated to match periods of interest (finance-specific scales) in financial data as [141]

1. Weekly-term trading (a week or 5 days)
2. Short-term trading (a month or 20 days)
3. Medium- or quarter term trading (3 months or 60 days)
4. Long-term trading (a year or 240 days).

Within either the MMSE or the MA-MSE, first the embedding dimension m and time lag τ of each variate are calculated to construct a composite multivariate delay vector, given by

$$
\begin{aligned}
X_m(i) = [&x_{1,i}, x_{1,i+\tau_1}, \ldots, x_{1,i+(m_1-1)\tau_1}, \\
&x_{2,i}, x_{2,i+\tau_2}, \ldots, x_{2,i+(m_2-1)\tau_2}, \ldots, \\
&x_{\rho,i}, x_{\rho,i+\tau_\rho}, \ldots, x_{\rho,i+(m_\rho-1)\tau_\rho}],
\end{aligned}
\tag{6.3}
$$

where $M = [m_1, m_2, ..., m_\rho] \in \mathbb{R}^\rho$ is the embedding dimension vector, $\tau = [\tau_1, \tau_2, \ldots, \tau_\rho]$ denotes the time lag vector, p is the number of variates, and $X_m(i) \in \mathbb{R}^m$.

The CGP within the MMSE creates scale factors by averaging the adjacent sample points within non-overlapping windows of increasing length ε (scale factor). The resulting data, denoted by $y^\epsilon_{k,j}$, represent a coarse-grained scale ϵ and is obtained as

$$
y^\epsilon_{k,j} = \frac{1}{\epsilon} \sum_{i=(j-1)\epsilon+1}^{j\epsilon} x_{k,i}, \quad 1 \leq j \leq \frac{N}{\epsilon}
\tag{6.4}
$$

The proposed MA-MSE replaces the CGP by MA-based scale generation, whereby both the trend, $s^\epsilon_{k,j}$, and the detrended data, $z^\epsilon_{k,j}$, are combined as $w^\epsilon_{k,j} = [s^\epsilon_{k,j}, z^\epsilon_{k,j}]$ and are used as pre-defined scales (input) for the algorithm.

Before computing the MMSE and the MA-MSE, a tolerance parameter, r, is defined and is used to search for similar patterns (delay vectors) by comparing the scalar distance between all pairs of delay vectors in equation (6.3), but without self-comparison. If the difference in the distance of a pair of delay vectors is less than r, the event of a similar pattern has occurred. The MMSE and MA-MSE algorithms can be summarised in Algorithm 6.1

Algorithm 6.1. Multivariate multiscale sample entropy (MMSE) & Moving-average multivariate sample entropy (MA-MSE)

For each scale: $y_{k,j}^{\epsilon}$ (MMSE), or $w_{k,j}^{\epsilon}$ (MA-MSE):

1. Construct a composite delay vector based on the scale $y_{k,j}^{\epsilon}$ (MMSE) or $w_{k,j}^{\epsilon}$ (MA-MSE).
2. Search for similar patterns in every data channel of the composite delay vector. If the difference in the pair-wise distance is less than or equal to the defined tolerance $max||X_m(i) - X_m(j)|| \leq r,\ j \neq i$, the event of similarity, denoted by P_m, is counted.
3. Calculate the probability $B^m(r) = \frac{1}{N}P_m$, where N is the total number of searches in each sub-delay vector.
4. Repeat Steps 1 to 3 for the $(m+1)$-dimensional composite delay vector.
5. Calculate the MMSE or the MA-MSE using

$$MMSE(m, \tau, r),\ MA - MSE(m, \tau, r) = -ln[\frac{B^{m+1}r}{B^m r}]$$

6.3.3 Assessment of Latent Index of Stress (ALIS)

We shall now introduce the Assessment of Latent Index of Stress (ALIS) to quantify "stress level of a financial organism" by considering the detrended data, $z_{k,j}$, as the input, followed by aggregating the normalised financial time series of the low (0-0.0042 Hz, LF) and high (0.0167-0.2 Hz, HF) frequency bands. The LF band was chosen so as to correspond to long-term trends (over a year), while the HF band is related to short-term trading (5 days), short-term trends (less than a month) and medium-term trends (3 months). Given the sampling frequency, f_s, of 1 Hz (the close stock value for each day), and $f = \frac{f_s}{N_0}$, where f is the frequency and N_0 the number of data points, a simple period-frequency conversion maps the periods of one year (240 sample points), 3 months (60 sample points), and 5 days (5 sample points) to the corresponding frequencies of 0.0042 Hz ($f = \frac{f_s}{N_0} = \frac{1}{240} = 0.0042$ Hz), 0.0167 Hz ($f = \frac{f_s}{N_0} = \frac{1}{60} = 0.0167$ Hz) and 0.2 Hz ($f = \frac{f_s}{N_0} = \frac{1}{5} = 0.2$ Hz) in

detrended financial time series. These frequencies were used as cut-off frequencies for the LF and HF bands. A threshold which determines whether the market is judged 'stressed' or 'normal' is derived based on the median, as summarised in Algorithm 6.2.

Algorithm 6.2. Assessment of Latent Index of Stress (ALIS)

Input: Generate the detrended data, $z_{k,j}$, using the MA method with a pre-defined scale factor (window size) of the length 1 year.

1. Construct the two time series corresponding to the sum of the power spectrum in the LF band and the sum of the power spectrum in the HF bands as a function of time (d), $LF(d)$ and $HF(d)$, where symbol d denotes a month.
2. Normalise the LF and HF time series by subtracting the mean and dividing by standard deviation in order to alleviate the problem of scaling.
3. Remove the offset in both the $LF(d)$ and $HF(d)$.
4. The ALIS is given by $ALIS(d) = LF(d) + HF(d)$.
5. Use the median in the $ALIS(d)$ as a threshold for stress in the market.

6.4 Analysis and Results

We applied our methodology to four stock market indices which represent the US economy over the last 25 years, between 1st January 1991 and 31st August 2015. Five consecutive periods of different natures were identified, based on our interpretation of key geopolitical and socio-economic events which affected the US and world economies [136], as follows:

- **Period 1:** 1-JAN-1991 to 31-DEC-1999. Economic boom, followed the 'dot-com' boom from 1997 to December 1999.
- **Period 2:** 1-JAN-2000 to 31-DEC-2003. Uncertainty, high volatility, and Internet bubble burst; the economy crisis further deteriorated due to the 9/11 terrorist attack and its aftermaths.

- **Period 3:** 1-JAN-2004 to 31-DEC-2007. Recovery due to huge investment in undervalued stocks.
- **Period 4:** 1-JAN-2008 to 31-DEC-2011. Sub-prime mortgage crisis.
- **Period 5:** 1-JAN-2012 to 31-AUG-2015. Weak growth and recovery owing to the uncertainty in fiscal policy ("fiscal cliff"), increases in tax, and a slowdown in the housing sector.

For the MA-MSE analysis, six scale factors of 5 days (short-term trading), 10 day, 1 month (short-term trends), 2 months, 3 months (medium-term trends) and 1 year (long-term trends) were employed in the MA method, in order to obtain trends within the original daily-adjusted closing prices of the four financial indices and the detrended data. (For the ALIS index, a scale factor of 1 year was used in the MA method). The trends and the detrended data of the DJIA, NASDAQ, Russell, and S&P 500 were estimated using a scale factor of 5 days, and the results are shown in Fig. 6.1 (a)-(d).

6.4.1 Entropy Estimates of Raw Financial Data through MMSE and MA-MSE

As an economic cycle typically lasts for approximately one year, and in order to capture economic changes over a small number of economic cycles, 4-year sliding windows with 3 years and 11 months overlap (1 month increment) were optimally applied. Fig. 6.2 illustrates the multivariate complexity of the original four financial indices estimated using the MMSE. The maximum duration of coarse graining scales was set to 1 year for which the six pre-defined scale factors can be selected. However, only the entropies of five scales (5 days, 10 days, 1 month, 2 months and 3 months) could be computed, as the entropy estimated using the 1-year scale diverged. Notice the effect of aliasing caused by poor resolution of

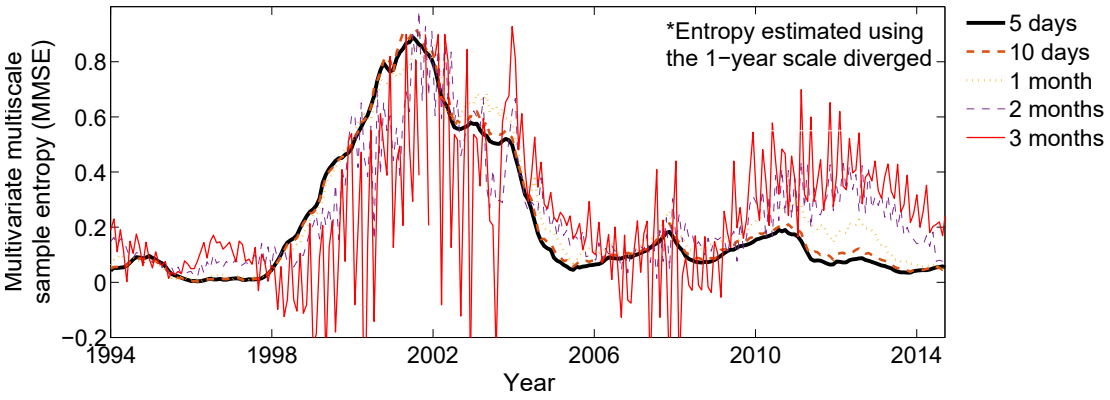

Figure 6.2: **Structural complexity of trends in compound stock indices estimated using multivariate multiscale sample entropy (MMSE).** The values were estimated using 4-year sliding windows with 3 years and 11 months overlap (1 month increment). The scale factors were 5 days, 10 days, 1 month, 2 months. For the 1-year scale, the entropy values diverged, and are excluded from the graph.

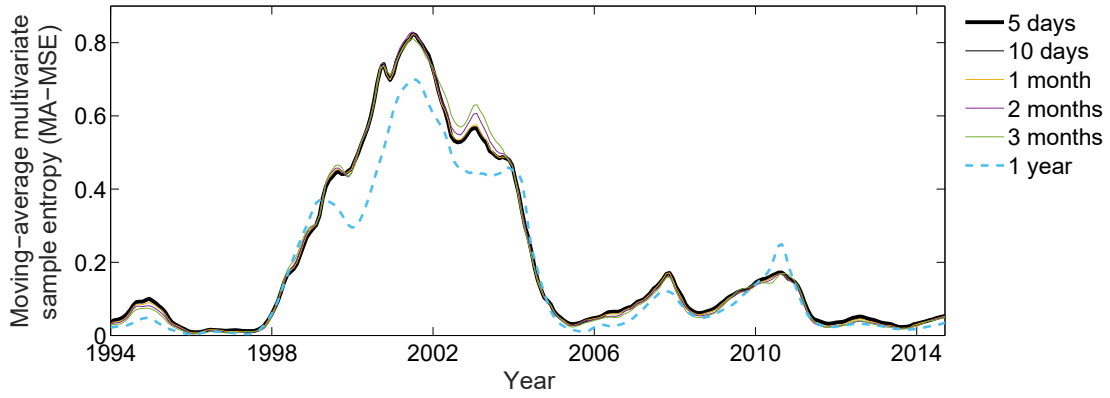

Figure 6.3: **Structural complexity of trends in compound stock indices estimated using moving-average multivariate sample entropy (MA-MSE).** The values were estimated using 4-year sliding windows with 3 years and 11 months overlap (1 month increment). The trends were generated using the MA method with six pre-defined scale factors (5 days, 10 days, 1 month, 2 months, 3 months and 1 year).

CGP in the 2- and 3-month scales, which implies that MMSE may not be suitable for large scales in financial data.

Fig. 6.3 shows the multivariate complexity of the trends (price moving average) estimated using MA-MSE with the six pre-defined scale factors. Observe that the multivariate complexities in all the scales exhibited similar sample entropy values

and no aliasing, except for the 1-year scale which showed a lower entropy, but similar variation as the other scales. The MA-MSE suggested high multivariate complexity during 2000 and 2004, the period of uncertainty and high volatility.

6.4.2 Entropy Estimates of Trend and Detrended Financial Data through MMSE and MA-MSE

Financial data were considered as an output of a low noise system. This is natural as they represent actual values of the stock indices, and therefore $m = 2$ was used. A unit time lag $\tau = 1$ was chosen as there exist short-term correlations in the sliding windows. Four-year sliding windows with 3 years and 11 months overlap (1 month increment) were used.

The long- and short-term correlations in data were found via the MA filter with different pre-defined scale factors, ϵ. We considered six pre-defined scale factors which match the periods of interest in financial data (short-term trading, short-, medium-, and long-term trends), for which the scale factors were respectively 5 days (5 sample points), 10 days (10 sample points), 1 month (20 sample points), 2 months (40 sample points), 3 months (60 sample points), and 1 year (240 sample points).

Fig. 6.4 shows the multivariate complexity of the trends (price moving average) estimated using the MA-MSE with the six pre-defined scale factors. Observe that in each economic period the multivariate complexities in all the scales exhibited similar sample entropy values. The MA-MSE suggested substantially higher multivariate complexity during the dot-com bubble and the Internet bubble burst, the periods of uncertainty and high volatility. During the sub-prime mortgage crisis, the MA-MSE revealed higher entropy values than the 'normal' periods – the economic-boom, economic-recovery, and weak-growth periods. Note that high multivariate complexities of the trends estimated using

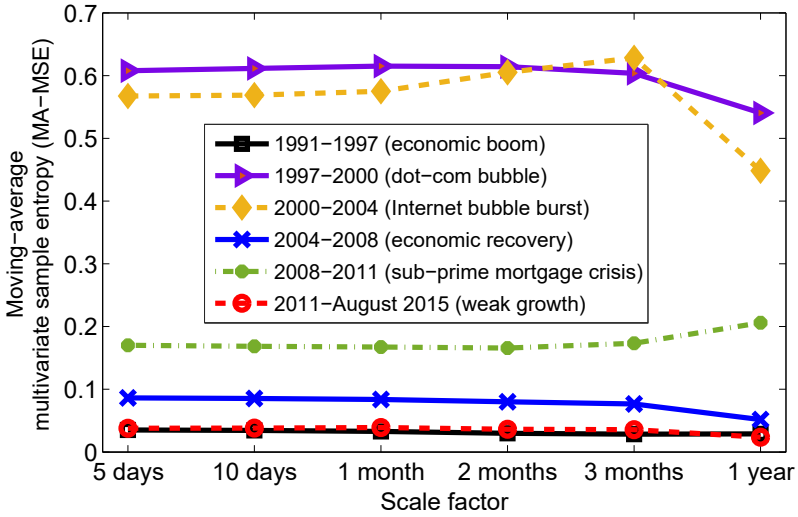

Figure 6.4: **Structural complexity of trends in compound stock indices.** The moving-average multivariate sample entropy (MA-MSE) values which represent the structural complexity for the trends of the four financial indices in different economic periods. The trends were generated using the MA method with six pre-defined scale factors (5 days, 10 days, 1 month, 2 months, 3 months and 1 year).

the MA-MSE revealed the presence of the crises, as financial trends show the tendencies of the markets to change in a particular way over time [138].

The multivariate complexities of the original data of the four financial indices and the trends were estimated respectively using the MMSE and the MA-MSE, and are shown in Fig. 6.2 and Fig. 6.3. Observe that the multivariate complexity quantified using the MA-MSE had no aliasing at large scales, a major improvement of the MA-MSE in scale generation.

Fig. 6.5 validates our complexity-loss hypothesis by examining the multivariate complexity of the detrended data (rate of change) estimated using the MA-MSE with six pre-defined scales. It suggests high complexity between 2000 and 2004, the period of uncertainty and high volatility. Observe in both the figures a high variation in complexity among different scales from 2004 to 2008 (the economic recovery period) – highly pronounced in the 5-day pre-defined scale, which indicates enhanced short-term dependencies in data. Also, during the 'dot-com bubble' between 1997 and 2000, long-term correlations – more regularity – were

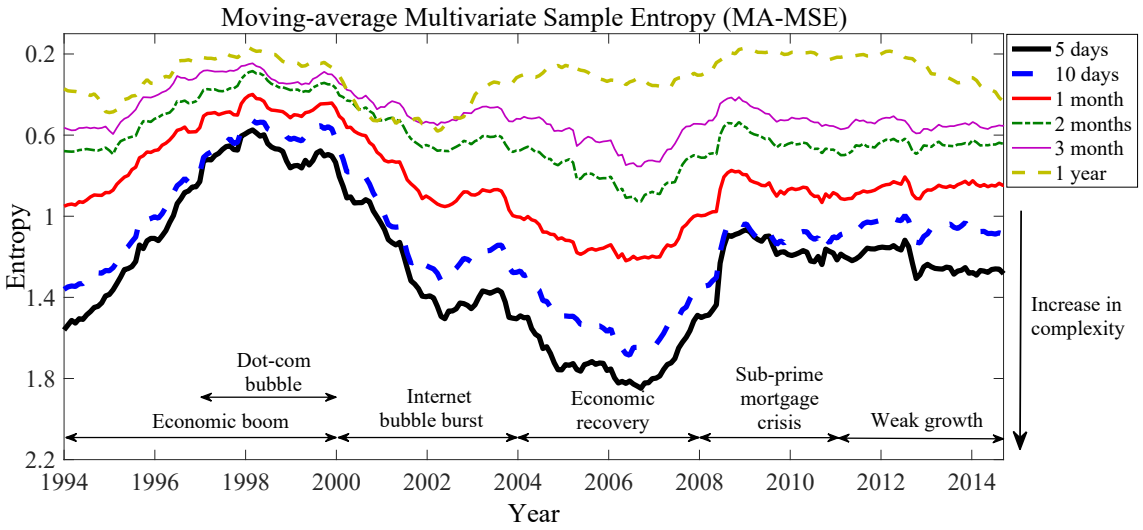

Figure 6.5: **Structural complexity of detrended compound stock indices.** The moving-average multivariate sample entropy (MA-MSE) values which represent the structural complexity for the detrended data of the four financial indices. These values were estimated using 4-year sliding windows with 3 years and 11 months overlap (1 month increment). The trends were generated using the MA method with six pre-defined scale factors (5 days, 10 days, 1 month, 2 months, 3 months and 1 year).

observed. Note that while the occurrences of the crises were detected using the MA-MSE applied to the financial trends, stress in the financial markets was observed using the MA-MSE applied to the detrended data.

6.4.3 Financial Stress through ALIS

The wellbeing of the "economic organism" was next examined through the complexity-loss hypothesis, whereby the low complexity (high 'stress' level) is indicated by high values of the proposed ALIS index applied to the detrended data. Four-year sliding windows with 3 years and 11 months overlap (1 month increment) were used. Fig. 6.6 (a)-(d) show the stress levels for the DJIA, NASDAQ, Russell 200 and S&P 500. Observe that the stress levels of the DJIA and the S&P 500 (markets for big companies) were above the thresholds during the two crises: the Internet bubble burst and the sub-prime mortgage crisis,

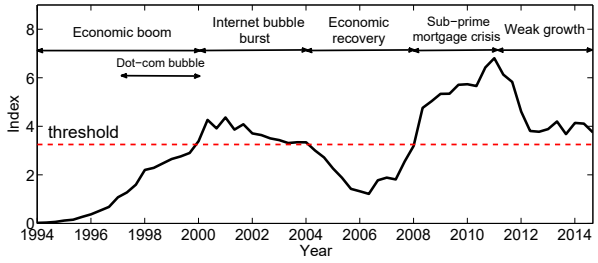

(a) Evolution of ALIS for DJIA.

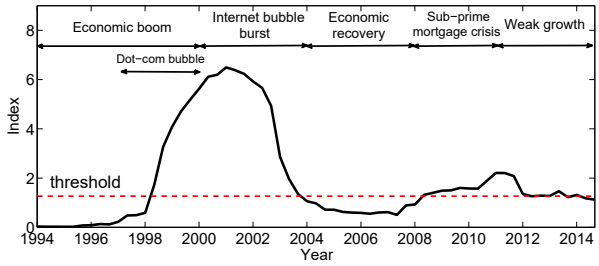

(b) Evolution of ALIS for NASDAQ.

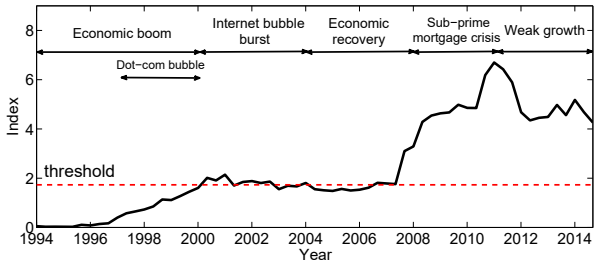

(c) Evolution of ALIS for Russell 2000.

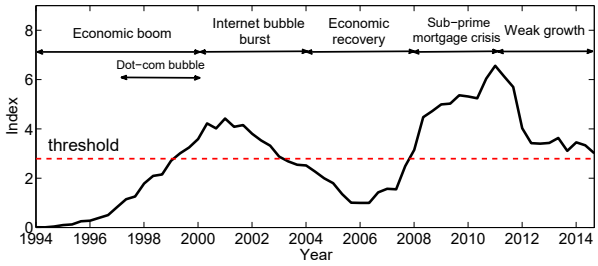

(d) Evolution of ALIS for S&P 500.

Figure 6.6: **Financial stress evolution through the proposed ALIS index.** Observe the perfect match in ALIS for the DJIA, Russell 2000 and S&P 500 for both the Internet burst and sub-prime mortgage abnormalities. The NASDAQ comprises only IT companies and thus reacted more strongly to the Internet bubble burst and less strongly for the housing crisis.

where the NASDAQ (market for IT companies) exhibited substantially higher level of stress during the dot-com bubble and the Internet bubble burst. Although the sub-prime mortgage crisis primarily affected the housing sector and

non-IT companies, it also impacted on IT companies, as indicated by an excess stress level of the NASDAQ in 2011. The Russell 2000 also exhibited high stress level during the sub-prime mortgage crisis and the recent weak growth period. However, as it comprises a small-cap segment of the US equity market, it was less affected by the Internet bubble burst.

6.5 Conclusions

We have examined the financial market from the point of view of complexity science and have analysed the constraints it exhibits in its responses to major socio-economic and geo-political events. This has been achieved for four major stock markets over a period of 25 years. The multiscale sample entropy based multivariate MA-MSE algorithm has been shown to provide both a composite estimate of complexity for financial indices and an estimate of systemic risk. Finally, we have introduced a new metric, referred to as the Assessment of Latent Index of Stress (ALIS), which measures the degree of financial stress based on the physically meaningful scales which reflect common trading principles. The ALIS has strongly indicated financial stress during the Internet and mortgage bubble crises. This work has conclusively demonstrated the utility of posterior complexity science approaches in the assessment of financial stress.

6.6 Future work

Future studies will focus on a variety of financial indices including currency exchange rates, and we will employ robust multivariate complexity measures approaches within machine learning algorithms in predictive scenarios.

Chapter 7

Conclusions and Future Work

This thesis has introduced the concept of complexity science and has brought it to real-world within the context of system stress analysis. This makes it possible for two real-world dynamical systems: i) autonomic nervous (ANS, in human), and ii) economic (in financial markets), which have been studied. We have analysed structural complexity of the two systems through standard entropy-based measures, Sample Entropy (SE), Fuzzy Entropy (FE) and their multiscale versions (MSE and MFE). This includes our proposed data-driven approaches called the "Cosine Similarity Entropy (CSE), "Multiscale Cosine Similarity Entropy (MCSE)", "Moving-average Multivariate Sample Entropy (MA-MSE)" and the "Assessment of Latent Index of Stress" (ALIS) methods. These complexity measures have unveiled that both the systems exhibit analogous underlying dynamical behaviors when perceiving stressors. This compiles with the "Complexity Loss Theory", which asserts that physiological responses in organisms under constraints (illness, aging, and other inhibitions such as stress) exhibit lower structural complexity than physiological responses in healthy organisms and the "Efficient Market Hypothesis" which states that there exist differences in structural complexity in security prices between regular and abnormal situations. It has been found that the standard uncertainty-based complexity measures (MSE, MFE, MA-MSE) yield a decrease in entropy values (low uncertainty-based complexity) during occurrences of a stressful period, while our novel MCSE yields an increase in entropy values (high self-correlation-based complexity) during the same period of stress. The results from the MCSE (with synthetic and real-world signals) have suggested a new interpretation for structural complexity of systems in the context of self-correlation which has been proven that the entropy curves of the synthetic

and real-world signals change monotonically from small to large (coarse grained) scales, while the MSE and MFE yielded mixed orders of entropy curves of such signals; the interpretation of structural complexity from both the MSE and MFE should therefore be made with caution.

In our human performance studies, based on the "General Adaptation Syndrome" it has been is found that: i) the high stress period occurs during the "pre-performance" period or coincides with the "high stress condition"; this corresponds to the "alarm stage" whereby the sympathetic nervous system activates to prepare the body to the fight or flight mode, resulting in the low level of the resistance to stress curve, ii) the low stress period occurs during the 'performance' period or coincides with the "low stress condition"; this corresponds to the "resistance stage" whereby the parasympathetic nervous system activates to calm the body (coping with stress), resulting in the high level of the resistance to stress curve, and iii) the rest (recovery) period occurs during the post-performance period and corresponds to the homeostasis stage whereby the both the SNS and PNS less or equally activated; this results in the normal (rest) level of the resistance to stress curve. However, the interpretation of stress scenarios is different when using the self-correlation-based MCSE whereby the high stress scenario corresponds to high complexity or high entropy values and the low stress scenario corresponds to low complexity or low entropy values.

In our economic stress study, we have shown that the results from the MA-MSE and the ALIS are able to capture an analogy between transitions from 'normal' (relaxed) to 'abnormal' (stressed) financial periods in four major stock indices of the US economy over the past 25 years: i) Dow Jones Industrial Average, ii) NASDAQ Composite, iii) Standard & Poor's 500, and iv) Russell 2000, together with FTSE 100, CAC 40 whereby the high stress events (economic crises) occur during low complexity (low entropy values estimated from the MA-MSE but high values of ALIS) and the low stress events (normal economic) occur during high complexity (high entropy values estimated from the MA-MSE but low values of

ALIS). Our findings support the EMH theory and reveal high stress for both the periods of Internet bubble burst and sub-prime mortgage crisis.

Future work on the CSE and the MCSE will be related to baseline wander of a time series which requires advanced signal processing techniques to model nonstationary components buried in such baseline. Multivariate versions of the CSE will also be needed since modern real-world data are usually obtained from multiple channels or multiple sensors for which such multivariate versions could yield more meaningful structural complexity quantified from inter and across multiple channels. Other directions of future work could be related to measuring structural complexity of a variety of real-world recordings, such as multichannel/ multimodal biomedical data obtained from real-life/experimental performances, currency exchange rates, high frequency trading stock indices, ect.

Bibliography

[1] H. Selye, "Stress and the general adaptation syndrome," *British Medical Journal*, vol. 1, no. 4667, pp. 1383–1392, 1950.

[2] S. Szabo, M. Yoshida, J. Filakovszky, and G. Juhasz, "Stress is 80 years old: From Hans Selye original paper in 1936 to recent advances in GI ulceration," *Current pharmaceutical design*, vol. 23, no. 27, pp. 4029–4041, 2017.

[3] R. Berto, "The role of nature in coping with psycho-physiological stress: A literature review on restorativeness," *Behavioral Sciences*, vol. 4, no. 4, pp. 394–409, 2014.

[4] M. Antoun, K. M. Edwards, J. Sweeting, and D. Ding, "The acute physiological stress response to driving: A systematic review," *PLOS ONE*, vol. 12, no. 10, pp. 1–13, 2017.

[5] S. K. Ciccarelli and J. N. White, *Psychology: An Exploration*. Pearson Prentice Hall, 2013.

[6] D. Shier, J. Butler, and R. Lewis, *Hole's Essentials of Human Anatomy & Physiology*. McGraw-Hill Companies,Incorporated, 2008.

[7] W. B. Cannon, "Organization for physiological homeostasis," *Physiological Reviews*, vol. 9, no. 3, pp. 399–431, 1929.

[8] W. B. Cannon, *Bodily Changes in Pain, Hunger, Fear, and Rage: An Account of Recent Researches Into the Function of Emotional Excitement*. D. Appleton, 1915.

[9] E. Cox, *Psychology for A-Level*. Psychology for Aqa Specification a Series, Oxford University Press, 2001.

[10] P. Laguna, G. B. Moody, and R. G. Mark, "Power spectral density of unevenly sampled data by least-square analysis: Performance and

application to heart rate signals," *IEEE Transactions on Biomedical Engineering*, vol. 45, no. 6, pp. 698–715, 1998.

[11] M. Malik, Task Force of the European Society of Cardiology and the North American Society of Pacing and Electrophysiology, M. Malik, and Task Force of the European Society of Cardiology and the North American Society of Pacing and Electrophysiology, "Heart rate variability: Standards of measurement, physiological interpretation, and clinical use," *European Heart Journal*, vol. 17, no. 5, pp. 354–381, 1996.

[12] S. M. Pincus, "Approximate entropy as a measure of system complexity," *Proceedings of the National Academy of Sciences*, vol. 88, no. 6, pp. 2297–2301, 1991.

[13] J. S. Richman and J. R. Moorman, "Physiological time-series analysis using approximate entropy and sample entropy," *American Journal of Physiology - Heart and Circulatory Physiology*, vol. 278, no. 6, pp. H2039–H2049, 2000.

[14] W. Chen, Z. Wang, H. Xie, and W. Yu, "Characterization of surface EMG signal based on fuzzy entropy.," *IEEE transactions on neural systems and rehabilitation engineering : a publication of the IEEE Engineering in Medicine and Biology Society*, vol. 15, pp. 266–272, jun 2007.

[15] M. Costa, A. L. Goldberger, and C. Peng, "Multiscale entropy analysis of complex physiologic time series," *Physical Review Letters*, vol. 89, no. 6, pp. 6–9, 2002.

[16] P. Grassberger, "Toward a quantitative theory of self-generated complexity," *International Journal of Theoretical Physics*, vol. 25, no. 9, pp. 907–938, 1986.

[17] M. Gell-Mann, "Let's call it plectics," *Complexity*, vol. 1, no. 5, 1995.

[18] N. Goldenfeld and L. P. Kadanoff, "Simple lessons from complexity," *Science*, vol. 284, no. 5411, pp. 87–89, 1999.

[19] J. Ladyman, J. Lambert, and K. Wiesner, "What is a complex system?," *European Journal for Philosophy of Science*, pp. 1–35, 2012.

[20] S. M. Manson, "Simplifying complexity: A review of complexity theory," *Geoforum*, vol. 32, no. 3, pp. 405–414, 2001.

[21] Editorial, "No man is an island," *Nature Physics*, vol. 5, no. 1, p. 1, 2009.

[22] A. N. Proto, *Nonlinear Phenomena in Complex Systems*. North-Holland Delta Series, Elsevier Science, 2012.

[23] U. Lu, S. M. Roach, D. Song, and T. W. Berger, "Nonlinear dynamic modeling of neuron action potential threshold during synaptically driven broadband intracellular activity," *IEEE Transactions on Bio-Medical Engineering*, vol. 59, pp. 706–716, mar 2012.

[24] E. F. Fama, "Random walks in stock-market prices," *Financial Analysts Journal*, vol. 21, pp. 55–59, 1965.

[25] E. Ghysels and D. R. Osborn, *The Econometric Analysis of Seasonal Time Series*. The Econometric Analysis of Seasonal Time Series, Cambridge University Press, 2001.

[26] C. Wu, C. Kao, and C. F. Lee, "Time-series properties of financial series and implications for modeling," *Journal of Accounting, Auditing & Finance*, vol. 11, no. 2, pp. 277–303, 1996.

[27] L. Lipsitz and A. Goldberger, "Loss of 'complexity' and aging. Potential applications of fractals and chaos theory to senescence.," *JAMA*, vol. 267, pp. 1806–1809, apr 1992.

[28] M. D. Costa, C.-K. Peng, and A. L. Goldberger, "Multiscale analysis of heart rate dynamics: Entropy and time irreversibility measures," *Cardiovascular engineering (Dordrecht, Netherlands)*, vol. 8, pp. 88–93, jun 2008.

[29] F. Takens, "Detecting Strange Attractors in Turbulence," in *Dynamical Systems and Turbulence* (D. Rand and L.-S. Young, eds.), pp. 366–381, Berlin, Heidelberg: Springer Berlin Heidelberg, 1981.

[30] S. M. Pincus and D. L. Keefe, "Quantification of hormone pulsatility via an approximate entropy algorithm," *American Journal of Physiology-Endocrinology And Metabolism*, vol. 262, no. 5, pp. E741–E754, 1992.

[31] S. M. Pincus and R. R. Viscarello, "Approximate entropy: A regularity measure for fetal heart rate analysis," *Obstetrics & Gynecology*, vol. 79, no. 2, pp. 249–255, 1992.

[32] S. M. Pincus and A. L. Goldberger, "Physiological time-series analysis: What does regularity quantify?," *American Journal of Physiology - Heart and Circulatory Physiology*, vol. 266, no. 4, pp. H1643–H1656, 1994.

[33] S. Pincus, "Approximate entropy (ApEn) as a complexity measure," *Chaos: An Interdisciplinary Journal of Nonlinear Science*, vol. 5, no. 1, pp. 110–117, 1995.

[34] S. M. Pincus, "Assessing serial irregularity and its implications for health," *Annals of the New York Academy of Sciences*, vol. 954, no. 1, pp. 245–267, 2001.

[35] R. K. Udhayakumar, C. Karmakar, and M. Palaniswami, "Approximate entropy profile: A novel approach to comprehend irregularity of short-term HRV signal," *Nonlinear Dynamics*, vol. 88, pp. 823–837, apr 2017.

[36] C. Gómez and R. Hornero, "Entropy and complexity analyses in Alzheimer's disease: An MEG study," *The Open Biomedical Engineering Journal*, vol. 4, pp. 223–235, 2010.

[37] N. H. Packard, J. P. Crutchfield, J. D. Farmer, and R. S. Shaw, "Geometry from a time series," *Physical Review Letters*, vol. 45, no. 9, pp. 52–56, 1980.

[38] E. R. Deyle and G. Sugihara, "Generalized theorems for nonlinear state space reconstruction," *PLOS ONE*, vol. 6, no. 3, pp. 1–8, 2011.

[39] M. Toda, T. Komatsuzaki, T. Konishi, S. A. Rice, and R. S. Berry, *Geometric Structures of Phase Space in Multi-Dimensional Chaos: Applications to Chemical Reaction Dynamics in Complex Systems*. No. pt. 2 in Advances in Chemical Physics, Wiley, 2005.

[40] H.-B. Xie, W.-X. He, and H. Liu, "Measuring time series regularity using nonlinear similarity-based sample entropy," *Physics Letters A*, vol. 372, no. 48, pp. 7140–7146, 2008.

[41] W. Chen, J. Zhuang, W. Yu, and Z. Wang, "Measuring complexity using FuzzyEn, ApEn, and SampEn.," *Medical Engineering and Physics*, vol. 31, pp. 61–68, jan 2009.

[42] H.-B. Xie, J.-Y. Guo, and Y.-P. Zheng, "Using the modified sample entropy to detect determinism," *Phys. Lett. A*, vol. 374, no. 38, pp. 3926–3931, 2010.

[43] M. Costa, A. L. Goldberger, and C.-K. Peng, "Multiscale entropy analysis of biological signals," *Physical review. E, Statistical, nonlinear, and soft matter physics*, vol. 71, p. 21906, feb 2005.

[44] M. U. Ahmed, N. Rehman, D. Looney, T. M. Rutkowski, and D. P. Mandic, "Dynamical complexity of human responses: a multivariate data-adaptive framework," *Bulletin of the Polish Academy of Sciences: Technical Sciences*, vol. 60, no. 3, pp. 433–445, 2012.

[45] R. L. Flood, "Complexity: A definition by construction of a conceptual framework," *Systems Research*, vol. 4, no. 3, pp. 177–185, 1987.

[46] B. Edmonds, "What is Complexity? - The philosophy of complexity per se with application to some examples in evolution," 1995.

[47] R. Standish, "On complexity and emergence," *Complexity International*, vol. 9, pp. 1–6, jan 2001.

[48] R. Standish, "Concept and definition of complexity," *Intelligent Complex Adaptive Systems*, vol. doi:10.401, pp. pp105–124, may 2008.

[49] C. Gan and G. Learmonth, "Comparing entropy with tests for randomness as a measure of complexity in time series," *ArXiv e-prints*, vol. arXiv:1512, pp. 1–21, dec 2015.

[50] M. Trifonov, "The structure function as new integral measure of spatial and temporal properties of multichannel EEG," *Brain Informatics*, vol. 3, pp. 211–220, dec 2016.

[51] R. Hornero, D. Abasolo, J. Escudero, and C. Gomez, "Nonlinear analysis of electroencephalogram and magnetoencephalogram recordings in patients with Alzheimer's disease," *Philosophical Transactions of the Royal Society A: Mathematical, Physical and Engineering Sciences*, vol. 367, pp. 317–336, jan 2009.

[52] M. Costa, C. K. Peng, A. L. Goldberger, and J. M. Hausdorff, "Multiscale entropy analysis of human gait dynamics," *Physica A: Statistical Mechanics and its Applications*, vol. 330, no. 1-2, pp. 53–60, 2003.

[53] M. U. Ahmed and D. P. Mandic, "Multivariate multiscale entropy analysis," *IEEE Signal Processing Letters*, vol. 19, pp. 91–94, feb 2012.

[54] R. L. Flood and E. Carson, *Dealing with Complexity an Introduction to the Theory and Application of Systems Science*. Springer US, 2 ed., 1993.

[55] D. E. Allen, M. McAleer, R. Powell, and A. K. Singh, "A non-parametric and entropy based analysis of the relationship between the VIX and S&P 500," *Journal of Risk and Financial Management*, vol. 6, no. 1, pp. 6–30, 2013.

[56] E. F. Fama, "Efficient capital markets: A review of theory and empirical work," *The Journal of Finance*, vol. 25, no. 2, pp. 383–417, 1970.

[57] T. Chanwimalueang, W. Von Rosenberg, and D. P. Mandic, "Enabling R-peak detection in wearable ECG: Combining matched filtering and Hilbert transform," *In Proceedings of the International Conference on Digital Signal Processing (DSP)*, vol. 2015-Septe, pp. 134–138, 2015.

[58] T. Chanwimalueang and D. Mandic, "Cosine Similarity Entropy: Self-Correlation-Based Complexity Analysis of Dynamical Systems," *Entropy*, vol. 19, pp. 1–23, nov 2017.

[59] T. Chanwimalueang, L. Aufegger, W. von Rosenberg, and D. P. Mandic, "Modelling stress in public speaking: Evolution of stress levels during conference presentations," in *In Proceedings of the IEEE International Conference on Acoustics, Speech and Signal Processing (ICASSP)*, vol. 2016-May, pp. 814–818, 2016.

[60] T. Chanwimalueang, L. Aufegger, T. Adjei, D. Wasley, C. Cruder, D. P. Mandic, and A. Williamon, "Stage call: cardiovascular reactivity to audition stress in musicians," *PLOS ONE*, vol. 12, no. 4, pp. 1–14, 2017.

[61] A. Hemakom, T. Chanwimalueang, A. Carrión, L. Aufegger, A. G. Constantinides, and D. P. Mandic, "Financial stress through complexity science," *IEEE Journal of Selected Topics in Signal Processing*, vol. 10, pp. 1112–1126, sep 2016.

[62] A. Williamon, L. Aufegger, D. Wasley, D. Looney, and D. P. Mandic, "Complexity of physiological responses decreases in high-stress musical performance," *Journal of The Royal Society Interface*, vol. 10, no. 89, p. 20130719, 2013.

[63] M. A. Peltola, "Role of editing of RR intervals in the analysis of heart rate variability," *Frontiers in Physiology*, vol. 3, 2012.

[64] P. Laguna, R. G. Mark, A. Goldberg, and G. B. Moody, "A database for evaluation of algorithms for measurement of QT and other waveform intervals in the ECG," pp. 673–676, IEEE, 1997.

[65] D. Ebenezer and V. Krishnamurthy, "Wave digital matched filter for electrocardiogram preprocessing," *Journal of biomedical engineering*, vol. 15, no. 2, pp. 132–134, 1993.

[66] Q. Xue, Y. H. Y. H. Hu, and W. J. Tompkins, "Neural-network-based adaptive matched filtering for QRS detection," *IEEE Transactions on Biomedical Engineering*, vol. 39, no. 4, pp. 317–329, 1992.

[67] A. Ruha, S. Sallinen, and S. Nissila, "A real-time microprocessor QRS detector system with a 1-ms timing accuracy for the measurement of ambulatory HRV," *IEEE Transactions on Biomedical Engineering*, vol. 44, no. 3, 1997.

[68] S. Dobbs, N. Schmitt, H. Ozemek, S. Dobbs, N. Schmitt, and H. Ozemek, "QRS detection by template matching using real-time correlation on a microcomputer," *Journal of Clinical Engineering*, vol. 9, no. 3, pp. 197–212, 1984.

[69] M. E. Nygårds, L. Sörnmo, M. E. Nygards, and L. Sornmo, "Delineation of the QRS complex using the envelope of the e.c.g.," *Medical & Biological Engineering & Computing*, vol. 21, pp. 538–547, sep 1983.

[70] Z. Song-Kai, W. Jian-Tao, X. Jun-Rong, Zhou Song-Kai, Wang Jian-Tao, and Xu Jun-Rong, "The real-time detection of QRS-complex using the envelope of ECG," in *In Proceedings of the IEEE International Conference on Engineering in Medicine and Biology Society (EMBS)*, vol. 1, p. 38, nov 1988.

[71] A. Science, U. Kingdom, M. H. Centre, and M. R. Infirmary, "A new QRS detection tlgorithm Based on the Hilbert Transform," pp. 379–382, 2000.

[72] D. Benitez, P. A. Gaydecki, A. Zaidi, and A. P. Fitzpatrick, "The use of the Hilbert transform in ECG signal analysis," *Computers in Biology and Medicine*, vol. 31, no. 5, pp. 399–406, 2001.

[73] J. Pan and W. Tompkins, "A real-time QRS detection algorithm," {*IEEE*} *Transactions on Biomedical Engineering*, vol. 3, pp. 230–236, 1985.

[74] R. A. Álvarez, A. J. M. Penín, and X. A. V. Sobrino, "A comparison of three QRS detection algorithms over a public database," *Procedia Technology*, vol. 9, pp. 1159–1165, 2013.

[75] B.-U. Köhler, C. Hennig, R. Orglmeister, B.-U. Kohler, C. Hennig, and R. Orglmeister, "The principles of software QRS detection," *IEEE Engineering in Medicine and Biology Magazine*, vol. 21, no. 1, 2002.

[76] A. L. Goldberger, L. A. Amaral, L. Glass, J. M. Hausdorff, P. C. Ivanov, R. G. Mark, J. E. Mietus, G. B. Moody, C. K. Peng, and H. E. Stanley, "PhysioBank, PhysioToolkit, and PhysioNet: Components of a new research resource for complex physiologic signals," *Circulation*, vol. 101, pp. E215–20, jun 2000.

[77] W. von Rosenberg, T. Chanwimalueang, D. Looney, and D. P. Mandic, "Vital signs from inside a helmet: A multichannel face-lead study," in *In Proceeding of the IEEE International Conference on Acoustics, Speech and Signal Processing - Proceedings (ICASSP)*, vol. TBC, pp. 982–986, 2015.

[78] T. Gautama, D. P. Mandic, and M. M. Van Hulle, "The delay vector variance method for detecting determinism and nonlinearity in time series," *Physica D*, vol. 190, no. 3-4, pp. 167–176, 2004.

[79] R. Alcaraz, D. Abásolo, R. Hornero, and J. Rieta, "Study of sample entropy ideal computational parameters in the estimation of atrial fibrillation organization from the ECG," *Computers in Cardiology*, vol. 37, pp. 1027–1030, sep 2010.

[80] S.-D. Wu, C.-W. Wu, K.-Y. Lee, and S.-G. Lin, "Modified multiscale entropy for short-term time series analysis," *Physica A: Statistical Mechanics and its Applications*, vol. 392, no. 23, pp. 5865–5873, 2013.

[81] A. Molina-Picó, D. Cuesta-Frau, M. Aboy, C. Crespo, P. Miró-Martínez, and S. Oltra-Crespo, "Comparative study of approximate entropy and sample entropy robustness to spikes," *Artificial Intelligence in Medicine*, vol. 53, no. 2, pp. 97–106, 2011.

[82] D. E. Lake, J. S. Richman, M. P. Griffin, and J. R. Moorman, "Sample entropy analysis of neonatal heart rate variability," *American Journal of Physiology*, vol. 283, no. 3, pp. R789–R797, 2002.

[83] T. Carter, "An introduction to information theory and entropy," *Complex Systems Summer School, Santa Fe*, p. 139, 2007.

[84] D. J. H. Garling, "Review: The Cauchy-Schwarz Master Class: An Introduction to the Art of Mathematical Inequalities by J. Michael Steele," *The American Mathematical Monthly*, vol. 112, no. 6, pp. 575–579, 2005.

[85] E. Deza and M. M. Deza, *Encyclopedia of Distances*. Berlin, Heidelberg: Springer Berlin Heidelberg, 2009.

[86] M. U. Ahmed, T. Chanwimalueang, S. Thayyil, and D. P. Mandic, "A multivariate multiscale fuzzy entropy algorithm with application to uterine EMG complexity analysis," *Entropy*, vol. 19, no. 1(2), pp. 1–18, 2017.

[87] M. Kryszkiewicz, *The Triangle Inequality Versus Projection onto a Dimension in Determining Cosine Similarity Neighborhoods of Non-negative Vectors*, pp. 229–236. Berlin, Heidelberg: Springer Berlin Heidelberg, 2012.

[88] M. Kryszkiewicz, "The cosine similarity in terms of the Euclidean distance," *Encyclopedia of Business Analytics and Optimization*, pp. 2498–2508, 2014.

[89] A. Abbad, K. Abbad, and H. Tairi, "Face Recognition Based on City-block and Mahalanobis Cosine Distance," in *In Proceedings of the International Conference on Computer Graphics, Imaging and Visualization (CGiV)*, pp. 112–114, mar 2016.

[90] M. Senoussaoui, P. Kenny, T. Stafylakis, and P. Dumouchel, "A Study of the cosine distance-based mean shift for telephone speech diarization," *IEEE/ACM Transactions on Audio, Speech, and Language Processing*, vol. 22, pp. 217–227, jan 2014.

[91] L. Sahu and B. R. Mohan, "An Improved K-means Algorithm Using Modified Cosine Distance Measure for Document Clustering Using Mahout with Hadoop," in *In Proceedings of the International Conference on Industrial and Information Systems (ICIIS)*, pp. 1–5, dec 2014.

[92] J. Ji, J. Li, Q. Tian, S. Yan, and B. Zhang, "Angular-similarity-preserving binary signatures for linear subspaces," *IEEE Transactions on Image Processing*, vol. 24, pp. 4372–4380, nov 2015.

[93] K. Pearson, "Note on regression and inheritance in the case of two parents," *Proceedings of the Royal Society of London*, vol. 58, pp. 240–242, 1985.

[94] S. M. Stigler, "Francis Galton's account of the invention of correlation," *Statistical Science*, vol. 4, no. 2, pp. 73–79, 1989.

[95] A. G. Josh Patterson, *Deep Learning a Practitioner's Approach*. O'Reilly Media, 1 ed., 2015.

[96] F. Kaffashi, R. Foglyano, C. G. Wilson, and A. L. Kenneth, "The effect of time delay on Approximate & Sample Entropy calculations," *Physica D*, vol. 237, pp. 3069–3074, 2008.

[97] J. S. Richman, D. E. Lake, and J. Moorman, "Sample entropy," *Methods in Enzymology*, vol. 384, no. 1991, pp. 172–184, 2004.

[98] G. D. Clifford, F. Azuaje, and P. E. McSharry, *Advanced Methods and Tools for ECG Data Analysis*. Artech House, 1st ed., sep 2006.

[99] V. Vuksanović and V. Gal, "Heart rate variability in mental stress aloud," *Medical Engineering and Physics*, vol. 29, no. 3, pp. 344–349, 2007.

[100] I. Van Diest, M. M. Bradley, P. Guerra, O. Van den Bergh, and P. J. Lang, "Fear-conditioned respiration and its association to cardiac reactivity," *Biological Psychology*, vol. 80, no. 2, pp. 212–217, 2009.

[101] G. E. Billman, "The LF/HF ratio does not accurately measure cardiac sympatho-vagal balance," *Frontiers in Physiology*, vol. 4, p. 26, feb 2013.

[102] G. Miličević and G. Milicevic, "Low to high frequency ratio of heart rate variability spectra fails to describe sympatho-vagal balance in cardiac patients," *Collegium antropologicum*, vol. 29, pp. 295–300, jun 2005.

[103] G. D. Clifford and L. Tarassenko, "Quantifying errors in spectral estimates of HRV due to beat replacement and resampling," *IEEE Transactions on Biomedical Engineering*, vol. 52, no. 4, pp. 630–638, 2005.

[104] N. R. Lomb, "Least-squares frequency analysis of unequally spaced data," *Astrophysics and Space Science*, vol. 39, no. 2, pp. 447–462, 1976.

[105] J. D. Scargle, "Studies in astronomical time series analysis. II - Statistical aspects of spectral analysis of unevenly spaced data," *The Astrophysical Journal*, vol. 263, pp. 835–853, 1982.

[106] G. B. Moody, "Spectral analysis of heart rate without resampling," in *In Proceedings of the IEEE Computers in Cardiology Conference*, pp. 715–718, 1993.

[107] G. G. Berntson, J. T. Bigger jr., D. L. Eckberg, P. Grossman, P. G. Kaufmann, M. Malik, H. N. Nagaraja, S. W. Porges, J. P. Saul, P. H. Stone,

and M. W. van der Molen, "Heart rate variability: Origins, methods, and interpretive caveats," *Psychophysiology*, vol. 34, pp. 623–648, 1997.

[108] N. E. Huang, Z. Shen, S. R. Long, M. C. Wu, H. H. Shih, Q. Zheng, N.-C. N.-C. Yen, C. C. Tung, and H. H. Liu, "The empirical mode decomposition and the Hilbert spectrum for nonlinear and non-stationary time series analysis," *Proceedings of the Royal Society of London A: Mathematical, Physical and Engineering Sciences*, vol. 454, no. 1971, pp. 903–995, 1998.

[109] A. K. Ahmed, J. B. Harness, and A. J. Mearns, "Respiratory control of heart rate," *European Journal of Applied Physiology and Occupational Physiology*, vol. 50, no. 1, pp. 95–104, 1982.

[110] T. E. Brown, L. A. Beightol, J. Koh, and D. L. Eckberg, "Important influence of respiration on human R-R interval power spectra is largely ignored," *Journal of Apply Physiology*, vol. 75, pp. 2310–2317, nov 1993.

[111] W. Tiller, R. McCraty, and M. Atkinson, "Cardiac coherence: a new, noninvasive measure of autonomic nervous system order," *Altern Ther Health Med*, vol. 2, no. 1, pp. 52–65, 1996.

[112] P. M. Lehrer, E. Vaschillo, B. Vaschillo, S. Lu, D. L. Eckberg, R. Edelberg, W. J. Shih, Y. Lin, T. Kuusela, K. U. O. Tahvanainen, and R. M. Hamer, "Heart rate variability biofeedback increases baroreflex gain and peak expiratory flow," *Psychosomatic Medicine*, vol. 65, no. 5, pp. 796–805, 2003.

[113] H. Selye, "A Syndrome produced by diverse nocuous agents," *The Journal of Neuropsychiatry and Clinical Neurosciences*, vol. 10, no. 2, pp. 230a–231, 1998.

[114] G. Billman, "Heart rate variability - a historical perspective," *Frontiers in Physiology*, vol. 2, p. 86, 2011.

[115] A. Williamon, *Musical Excellence: Strategies and Techniques to Enhance Performance*. Oxford University Press, 2004.

[116] M. G. Craske and K. D. Craig, "Musical performance anxiety: The three-systems model and self-efficacy theory," *Behaviour Research and Therapy*, vol. 22, no. 3, pp. 267–280, 1984.

[117] J. Abel and K. Larkin, "Anticipation of performance among musicians: Physiological arousal, confidence, and state-anxiety Inventory," *Psychology of Music*, vol. 18, pp. 171–182, 1990.

[118] M. Brotons, "Effects of performing conditions on music performance anxiety and performance quality," *Journal of Music Therapy*, vol. 31, pp. 63–81, 1994.

[119] M. Yoshie, K. Kudo, T. Murakoshi, and T. Ohtsuki, "Music performance anxiety in skilled pianists: effects of social-evaluative performance situation on subjective, autonomic, and electromyographic reactions," *Experimental Brain Research*, vol. 199, no. 2, p. 117, 2009.

[120] M. Pagani, F. Lombardi, S. Guzzetti, O. Rimoldi, R. Furlan, P. Pizzinelli, G. Sandrone, G. Malfatto, S. Dell'Orto, and E. Piccaluga, "Power spectral analysis of heart rate and arterial pressure variabilities as a marker of sympatho-vagal interaction in man and conscious dog," *Circulation Research*, vol. 59, no. 2, pp. 178–193, 1986.

[121] G. G. Berntson and J. T. Cacioppo, "Heart rate variability: Stress and psychiatric conditions," *Dynamic electrocardiography*, pp. 57–64, 2004.

[122] G. G. Berntson, J. T. Cacioppo, P. F. Binkley, B. N. Uchino, K. S. Quigley, and A. Fieldstone, "Autonomic cardiac control. III. Psychological stress and cardiac response in autonomic space as revealed by pharmacological blockades," *Psychophysiology*, vol. 31, pp. 599–608, nov 1994.

[123] B. H. Friedman, J. F. Thayer, and R. A. Tyrrell, "Spectral characteristics of heart period variability during cold face stress and shock avoidance in normal subjects," *Clinical autonomic research : official journal of the Clinical Autonomic Research Society*, vol. 6, pp. 147–152, jun 1996.

[124] J. P. Delaney and D. A. Brodie, "Effects of short-term psychological stress on the time and frequency domains of heart-rate variability," *Perceptual and motor skills*, vol. 91, pp. 515–524, oct 2000.

[125] D. Lucini, G. Norbiato, M. Clerici, and M. Pagani, "Hemodynamic and autonomic adjustments to real life stress conditions in humans," *Hypertension*, vol. 39, no. 1, pp. 184–188, 2002.

[126] R. P. Sloan, P. A. Shapiro, E. Bagiella, S. M. Boni, M. Paik, J. T. J. Bigger, R. C. Steinman, and J. M. Gorman, "Effect of mental stress throughout the day on cardiac autonomic control.," *Biological psychology*, vol. 37, pp. 89–99, mar 1994.

[127] Z. Visnovcova, M. Mestanik, M. Javorka, D. Mokra, M. Gala, A. Jurko, A. Calkovska, and I. Tonhajzerova, "Complexity and time asymmetry of heart rate variability are altered in acute mental stress," *Physiological measurement*, vol. 35, pp. 1319–1334, jul 2014.

[128] V. Tuzcu, S. Nas, T. Borklu, and A. Ugur, "Decrease in the heart rate complexity prior to the onset of atrial fibrillation," *Europace : European pacing, arrhythmias, and cardiac electrophysiology : journal of the working groups on cardiac pacing, arrhythmias, and cardiac cellular electrophysiology of the European Society of Cardiology*, vol. 8, pp. 398–402, jun 2006.

[129] G.-L. Xiong, L. Zhang, H.-S. Liu, H.-J. Zou, and W.-Z. Guo, "A comparative study on ApEn, SampEn and their fuzzy counterparts in a multiscale framework for feature extraction," *Journal of Zhejiang University SCIENCE A*, vol. 11, no. 4, pp. 270–279, 2010.

[130] J. A. Johnstone, P. A. Ford, G. Hughes, T. Watson, and A. T. Garrett, "Bioharness(texttrademark) Multivariable Monitoring Device: Part. I: Validity," sep 2012.

[131] J. A. Johnstone, P. A. Ford, G. Hughes, T. Watson, and A. T. Garrett, "Bioharness multivariable monitoring device: part. II: reliability.," *Journal of sports science & medicine*, vol. 11, no. 3, pp. 409–417, 2012.

[132] J. G. A. Spielberger C.D, Gorsuch R.L, Lushene R, Vagg P.R, *Manual for the State-Trait Anxiety Inventory*. Palo Alto, CA: Consulting Psychologists Press, 1983.

[133] P. Domitrovich and P. Stein, "A new method to detect erratic sinus rhythm in RR-interval files generated from Holter recordings," *Computers in Cardiology*, pp. 665–668, 2002.

[134] D. Singh, K. Vinod, and S. C. Saxena, "Sampling frequency of the RR interval time series for spectral analysis of heart rate variability.," *Journal of medical engineering & technology*, vol. 28, no. 6, pp. 263–272, 2004.

[135] J. E. Mietus, C.-K. Peng, I. Henry, R. L. Goldsmith, and A. L. Goldberger, "The pNNx files: re-examining a widely used heart rate variability measure," oct 2002.

[136] W. Er and D. P. Mandic, "Dynamical complexity analysis of multivariate financial data," in *Proceeding of IEEE International Conference on Acoustics, Speech and Signal Processing - Proceedings (ICASSP)*, pp. 8732–8736, IEEE, 2013.

[137] N. Amenc, F. Goltz, and V. Le Sourd, "Assessing the quality of stock market indices: Requirements for asset allocation and performance measurement," *EDHEC-Risk Institute*, 2006.

[138] G. A. Fontanills and T. Gentile, *The Stock Market Course*, vol. 117. John Wiley & Sons, 2002.

[139] H. S. Dent, *The Next Great Bubble Boom: How to Profit from the Greatest Boom in History, 2006-2010*. Free Press, 2006.

[140] R. Stutely, *Numbers guide*. Bloomberg Press,, 2003.

[141] R. D. Edwards, W. H. C. Bassetti, and J. Magee, *Technical Analysis of Stock Trends*. CRC press, 2007.

[142] A. J. Camm, M. Malik, J. T. Bigger, G. Breithardt, S. Cerutti, R. J. Cohen, P. Coumel, E. L. Fallen, H. L. Kennedy, R. E. Kleiger, and Others, "Heart rate variability: standards of measurement, physiological interpretation and clinical use. Task Force of the European Society of Cardiology and the North American Society of Pacing and Electrophysiology," *Circulation*, vol. 93, no. 5, pp. 1043–1065, 1996.

[143] P. Lequeux and M. Menon, "An eigenvalue approach to risk regimes in currency markets," *Journal of Derivatives & Hedge Funds*, vol. 16, no. 2, pp. 123–135, 2010.

[144] M. Ahmed and D. Mandic, "Multivariate multiscale entropy: a tool for complexity analysis of multichannel data.," *Physical review. E, Statistical, nonlinear, and soft matter physics*, vol. 84, p. 61918, dec 2011.

[145] P. M. Addo, M. Billio, and D. Guegan, "Understanding exchange rates dynamics," 2013.

[146] R. Cardarelli, S. Elekdag, and S. Lall, "Financial stress and economic contractions," *Journal of Financial Stability*, vol. 7, no. 2, pp. 78–97, 2011.

[147] M. Kritzman, Y. Li, S. Page, and R. Rigobon, "Principal components as a measure of systemic risk," *The Journal of Portfolio Management*, vol. 37, no. 4, pp. 112–126, 2011.

[148] R. D. Lagunoff, Stacey, L. Schreft, P. Kehoe, N. Kocherlakota, J. Lacker, and A. Villamil, "A model of financial fragility," *Journal of Economic Theory*, pp. 220–264, 2001.

[149] H. Lütkepohl, "Impulse Response Function," in *The New Palgrave Dictionary of Economics*, pp. 1–5, London: Palgrave Macmillan UK, 2016.

[150] D. Duffie, "Systemic Risk Exposures: a 10-by-10-by-10 Approach," in *Risk Topography: Systemic Risk and Macro Modeling*, pp. 47–56, University of Chicago Press, 2013.

[151] R. Balakrishnan, S. Danninger, S. Elekdag, and I. Tytell, "The transmission of financial stress from advanced to emerging economies," *Emerging Markets Finance and Trade*, vol. 47, no. sup2, pp. 40–68, 2011.

[152] C. S. Hakkio and W. R. Keeton, "Financial stress: what is it, how can it be measured, and why does it matter?," *Economic Review-Federal Reserve Bank of Kansas City*, vol. 94, no. 2, p. 5, 2009.

[153] E. C. Zeeman, "Catastrophe theory," *Scientific American*, vol. 234, no. 4, pp. 65–83, 1976.

[154] T. Takahashi, R. Y. Cho, T. Murata, T. Mizuno, M. Kikuchi, K. Mizukami, H. Kosaka, K. Takahashi, and Y. Wada, "Age-related variation in EEG complexity to photic stimulation: A multiscale entropy analysis," *Clinical Neurophysiology*, vol. 120, pp. 476–483, mar 2009.

[155] G. B. Moody and R. G. Mark, "A new method for detecting atrial fibrillation using RR intervals," in *In Proceedings of the Computers in Cardiology*, (Aachen, Germany), pp. 227–230, 1983.

Appendix A. Autoregressive Models

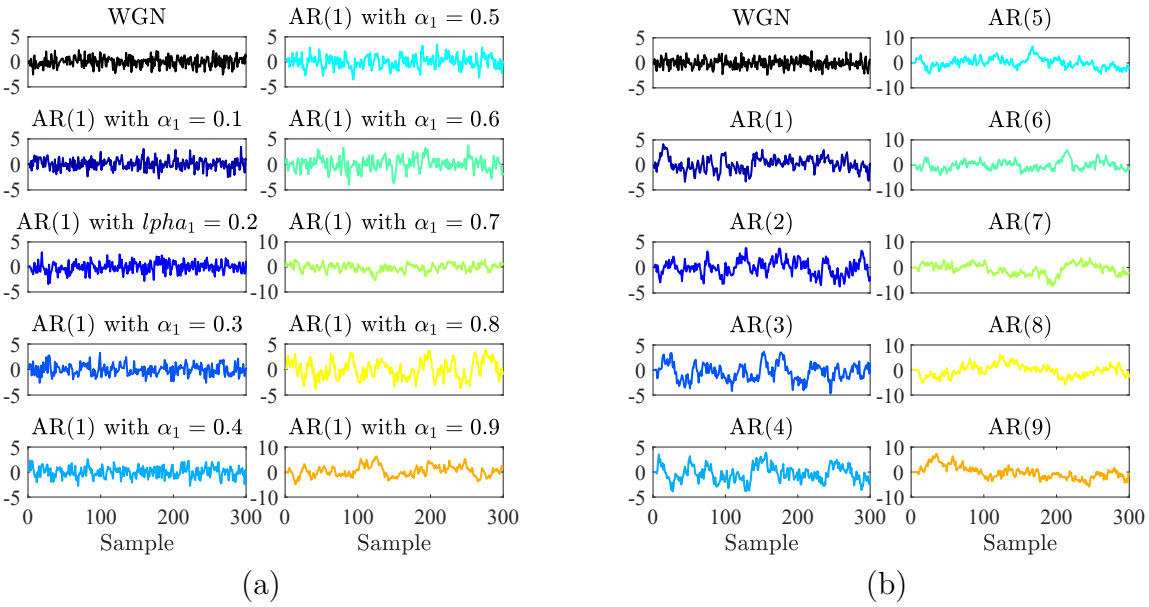

Figure A.1: **Two groups of synthetic AR processes used for evaluating the performances of the SE, FE and CSE approaches**. (a) The first 300 samples from AR(1) processes with nine varying coefficients of correlation (α_1) and the driving WGN input. (b) The first 300 samples of the AR(1) - AR(9) processes with the pre-defined correlation coefficients and the driving input WGN, giving signals with the degrees of freedom of the underlying generation system ranging from 1 to 9.

To evaluate the performances of the SE, FE and CSE approaches, we generated two groups of AR models: i) AR(1) with nine varying correlation coefficients and ii) nine orders of AR processes with the pre-defined correlation coefficients. For the first group, AR(1) models driven by random noise were synthesized using 20 independent realizations of 10,000 samples. Each realization consists of nine varying coefficients of the AR(1) processes generated as

$$x(t) = \alpha_1 x(t-1) + \varepsilon(t) \tag{A.1}$$

where $\varepsilon(t) \sim \mathcal{N}(0,1)$ and $\alpha_1 \in [0.1, 0.2, 0.3, 0.4, 0.5, 0.6, 0.7, 0.8, 0.9]$.

For the second group, $p^{th}-$order AR processes driven by random noise were

Table A.1: The pre-defined correlation coefficients used for the nine orders of the AR(p) processes

Correlation coefficient	α_1	α_2	α_3	α_4	α_5	α_6	α_7	α_8	α_9
AR(1)	0.5	-	-	-	-	-	-	-	-
AR(2)	0.5	0.25	-	-	-	-	-	-	-
AR(3)	0.5	0.25	0.125	-	-	-	-	-	-
AR(4)	0.5	0.25	0.125	0.0625	-	-	-	-	-
AR(5)	0.5	0.25	0.125	0.0625	0.0313	-	-	-	-
AR(6)	0.5	0.25	0.125	0.0625	0.0313	0.0156	-	-	-
AR(7)	0.5	0.25	0.125	0.0625	0.0313	0.0156	0.0078	-	-
AR(8)	0.5	0.25	0.125	0.0625	0.0313	0.0156	0.0078	0.0039	-
AR(9)	0.5	0.25	0.125	0.0625	0.0313	0.0156	0.0078	0.0039	0.0019

synthesized using 20 independent realizations of 10,000 samples, given by

$$x(t) = \sum_{i=1}^{p} \alpha_i x(t-i) + \varepsilon(t) \tag{A.2}$$

where $\varepsilon(t) \sim \mathcal{N}(0,1)$, p is the AR order increasing from 1 to 9 and α_i represents the pre-defined correlation coefficients of the i^{th}order as shown in Table (A.1).

Note that with the selected correlation coefficients, both groups of the generated AR models were stable and stationary, which can be seen in Figure A.1.

Appendix B. Heart Rate Variability Database

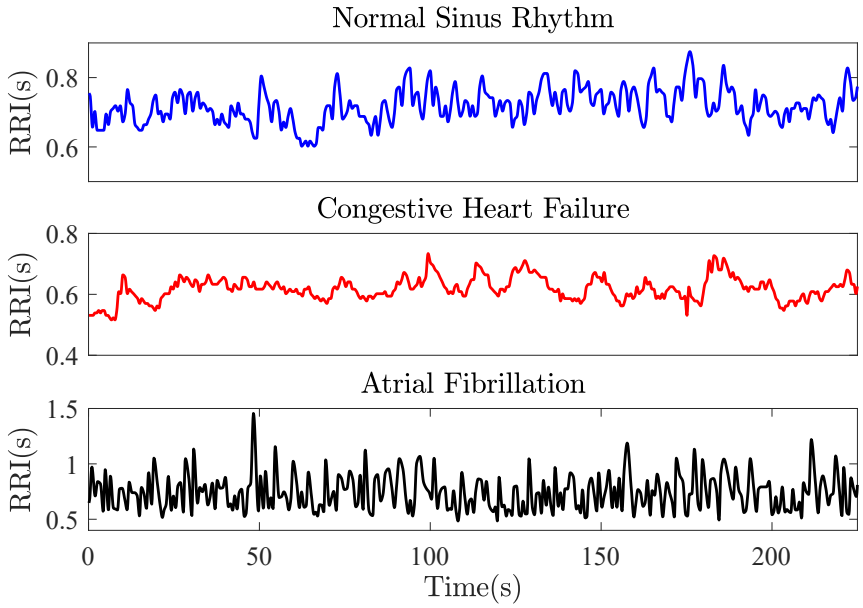

Figure B.1: **Example of the RR intervals (RRI) of the three cardiac conditions over 225 second duration**. Top: RRI of the normal sinus rhythm database (in blue); Middle: RRI of the congestive heart failure database (in red); Bottom: graph represents the atrial fibrillation (in black).

One-hour RR intervals of the three cardiac pathologies; Normal Sinus Rhythm (NSR), Congestive Heart Failure (CHF) and Atrial Fibrillation (AF), were extracted from the Physiobank database available at https://physionet.org/ [76]. The beat annotations (RR intervals) of the NSR and CHF database were obtained by the automated detector with manual review and correction, while the beat annotations of the AF database were only obtained by automated detector. For the NSR database, we obtained 18 RR intervals of subjects who had no significant arrhythmia. The subjects included 5 men, aged 26 to 45, and 13 women, aged 20 to 50. For the CHF database, we selected the first 20 RR intervals from the total of 29 subjects with congestive heart failure (NYHA classes I, II, and III), who aged from 34 to 79. The subjects included 8 men and

2 women; the gender is not known for the remaining 21 subjects. For the AF database, we obtained 20 RR intervals from the total of 25 subjects, with no information about the age and gender [155]. An example of the RR intervals of the three cardiac conditions within 225 seconds is shown in Figure B.1.